UNIVERSITY OF ICELAND

GRÓ · GTP Geothermal Training Programme

unesco Centre Under the auspices of UNESCO

**M.S. thesis in**
**Geophysics**

# 3D-density model using gravity data and a Play Fairway Analysis to evaluate the most favorable drilling targets in Berlín Geothermal Field, El Salvador

**Mayra Raquel Hernández Cabrera**

June 2024

**FACULTY OF EARTH SCIENCES**

# 3D-density model using gravity data and a Play Fairway Analysis to evaluate the most favorable drilling targets in Berlín Geothermal Field, El Salvador

Mayra Raquel Hernández Cabrera

Thesis submitted in partial fulfillment of a
*Magister Scientiarum* degree in Geophysics

MS Committee
Gylfi Páll Hersir
Thorbjörg Ágústsdóttir
Halldór Geirsson

Examiner
Thorsteinn Egilson

Faculty of Earth Sciences
School of Engineering and Natural Sciences
University of Iceland
Reykjavik, June 2024

3D-density model using gravity data and a Play Fairway Analysis to evaluate the most favorable drilling targets in Berlín Geothermal Field, El Salvador

60 ECTS
Thesis submitted in partial fulfillment of a *M.S.* degree in Geophysics



Faculty of Earth Sciences
School of Engineering and Natural Sciences
University of Iceland
VRII, Hjardarhagi 2-6
102 Reykjavik
Iceland

Telephone: 525-4000

Bibliographic information:
Mayra Raquel Hernández Cabrera, 2024, *3D-density model using gravity data and a Play Fairway Analysis to evaluate the most favorable drilling targets in Berlín Geothermal Field, El Salvador*, M.S.Thesis, Faculty of Earth Sciences, University of Iceland, 75 pp.

Printing: Háskólaprent, Fálkagata 2, 107 Reykjavík
Reykjavik, Iceland, June 2024

# Abstract

The Berlín Geothermal Field is a high-temperature geothermal system located in the southern flank of the Central Graben and the northwest sector of the Berlín-Tecapa volcanic complex in Usulután, El Salvador. The geothermal system is one of the main geothermal resources in El Salvador, with an installed capacity of 109.2 MWe, composed of three condensing units: two units of 28.1 MWe since 2000, one of 44 MWe operating since 2007, and one binary unit of 9 MWe since 2009. In the area, there are 45 wells, of which 15 are producers, 24 are injection wells, and one well is used for monitoring the reservoir pressure. The rest of the wells are either on standby or abandoned. By 2023, the geothermal power plant delivered approximately 11.08% of the total energy generation in the country. Due to its great importance as a renewable resource, it is deemed of big value to understand the geothermal system better since physical properties (density, electrical resistivity, temperature) permit validating geophysical models for further utilization of the resource. This work aims to evaluate the Berlín Geothermal resource through a 3D model "a conceptual model", which includes different geoscientific data, and another model called the "Weighted Model", using the Play Fairway Analysis method to identify the most favorable areas to drill new production and reinjection. We used the Geosoft Oasis Montaj and Leapfrog Geothermal programs to build the 3D-density and 3D-weighted models, respectively. This study builds on previous works. The 3D density model, the seismic velocity tomography made in 2022, and the static temperature profile are used to update the conceptual model from 2019 (LAGEO, 2019) as well as, the weighted model made in 2021 (Hernández et al., 2023). The updated conceptual model shows the flow path of deep hot fluids towards platforms TR-4, TR-18, and TR-17, which confirms the upflow zones in BGF. Besides, the steam cap of the area which has been identified in boreholes TR-18A and TR-18B and extends towards borehole TR-17A. To summarize, the caprock is confirmed between 1.7 to 2.0 $g/cm^3$, the reservoir between 2.3 and 2.6 $g/cm^3$ and the basement between 2.65 and 3.0 $g/cm^3$. The updated Favorability Index Model (FIM) suggests five potential geothermal areas where the best parameters are converging from all models, indicating a favorability equal to or higher than 75%.

# Ágrip

Berlin jarðhitasvæðið er háhitakerfi í suðurhlíðum meginsigdældarinnar og í norðvestur hluta Berlin-Tecapa eldfjallakerfisins í Usultan, El Salvador. Jarðhitakerfið er ein stærsta jarðhitaauðlindin í El Salvador. Uppsett afl er 109,2 MWe. Þar af eru þrír jarðgufuhverflar, tveir þeirra 28,1 MWe, starfræktir frá árinu 2000 og sá þriðji er 44 MWe, starfræktur frá 2007. Auk þess var sett upp 9 MWe tvívökvavirkjun árið 2009. Alls hafa verið boraðar 45 holur. Þar af eru 15 nýttar til rafmagnsframleiðslu, 24 til niðurdælingar og ein til þess að fylgjast með þrýstingi í jarðhitakerfinu. Hinar fimm holurnar eru ýmist í biðstöðu eða hafa verið gefnar upp á bátinn. Árið 2023 stóð jarðhitakerfið undir um 11,08% af heildarorkuframleiðslu landsins. Vegna hins mikla mikilvægis svæðisins sem endurnýtanleg auðlind er talið mikilvægt að átta sig enn betur á jarðhitakerfinu þar sem þekktir eðliseiginleikar á borð við eðlisþyngd, viðnám og hitastig renna frekari stoðum undir jarðeðlisfræðileg líkön af svæðinu og þar með aukinni nýtingu. Hér er markmiðið að leggja mat á Berlin jarðhitageyminn með þrívíðu "hugmyndalíkani" sem grundvallast á jarðvísindalegum gögnum en einnig með svokölluðu "viktuðu líkani" þar sem notaðar eru tölfræðilegar aðferðir (Play Fairway Analysis, PFA) til þess skilgreina álitlegustu svæðin til borunar nýrra vinnsluhola annars vegar og niðurdælingarhola hins vegar. Við notuðum Geosoft Oasis Montaj og Leapfrog Geothermal forritin til þess að búa til þrívítt eðlisþyngdar líkan annars vegar og þrívítt viktað líkan hins vegar. Þessi vinna grundvallast á eldri vinnu. Þrívíða eðlisþyngdarlíkanið, þrívíð hraðalíkön jarðskjálftabylgna frá 2022 og hitamælingar í borholum voru notuð til þess að uppfæra hugmyndalíkanið frá 2019 (LAGEO, 2019) sem og viktaða líkanið frá 2021 (Hernández o.fl., 2023). Uppfært hugmyndalíkan sýnir rennslisleiðir heits vökva sem kemur djúpt að og rennur í áttina að borstæðum hola TR-4, TR-18 og TR-17 Líkanið staðfestir uppstreymið við Berlín jarðhitasvæðið. Sömuleiðis gufupúðann sem kemur fram víð holur TR-18A og TR-18B og teygir sig að holu TR-17A. Samandregið má segja að að eðlisþyngd þakbergsins sé milli 1,7 og 2,0 $g/cm^3$, jarðhitageymisinn milli 2,3 og 2,6 $g/cm^3$ og eðlisþyngd berggrunnsins sé milli 2,65 og 3,0 $g/cm^3$. Uppfært tölfræðilíkan af álitlegustu svæðunum gefur vísbendingu um fimm vænleg jarðhitasvæði þar sem megin breytur allra líkananna falla saman og tölfræðín bendir til líkinda sem eru jafnt og eða hærri en 75%.

*Dedication*

*To my parents, for their encouragement and dedication. To my daughter and son, Fiorella and Nicolás who have been my inspiration, support and motivation. To my boyfriend for his support, patience and dedication. To my friends for their patience and lovely words during my experience far away to home.*

# Table of Contents

# List of Figures

# List of Tables

# Abbreviations

| | |
|---|---|
| **1D** | One Dimensional |
| **2D** | Two Dimensional |
| **3D** | Three Dimensional |
| **BA** | Bouguer Anomaly |
| **BGF** | Berlin Geothermal Field |
| **FIM** | Favorability Index Model |
| **GDB** | Geodatabase |
| **IM** | Index Model |
| **ISOR** | Iceland GeoSurvey |
| **m a.s.l.** | Meters above sea level |
| **m b.s.l.** | Meters below sea level |
| **MT** | Magnetotelluric |
| **MWe** | Electrical Megawatt |
| **NW** | North-West |
| **PT** | Pressure and Temperature |
| **SE** | South-East |
| **TDEM** | Time Domain Electromagnetic |

# Acknowledgements

My sincere gratitude to the GRÓ Geothermal Training Program under the auspices of UNESCO, and the Government of Iceland for awarding me a scholarship to study at the University of Iceland and LAGEO for granting me the time to pursue my studies.

I appreciate and thank the GTP staff, Guðni Axelsson, Málfrídur Ömarsdóttir, and Ingimar Haraldsson, for their help and support during my time in Iceland.

I want to thank my supervisors, Gylfi Páll Hersir and Thorbjörg Ágústsdóttir, for all their time, continuous guidance, assistance, and support.

Thanks to my coworkers at LAGEO for making the necessary documentation available for me and all the Geophysics department staff in LAGEO for their support. Last but not least to my family for their moral support.

UNIVERSITY OF ICELAND

GRÓ · GTP Geothermal Training Programme

unesco Centre Under the auspices of UNESCO

**M.S. thesis in**
**Geophysics**

# 3D-density model using gravity data and a Play Fairway Analysis to evaluate the most favorable drilling targets in Berlín Geothermal Field, El Salvador

**Mayra Raquel Hernández Cabrera**

June 2024

**FACULTY OF EARTH SCIENCES**

# 2 Berlin Geothermal Field

This chapter presents a conceptual model of Berlín Geothermal Field (BGF), updated in 2019 through geoscientific information compiled until 2018 (LAGEO, 2019). The new information includes a) Geological information from wells drilled between 2012-2018 (TR-18B, TR-5D, TR-17C, TR-14B, and TR-4R) (see Figure 2.2); b) Diffuse gas measured during 2000, 2010, 2015, and 2018, and measurements from surface and subsurface; c) The 3D resistivity model made in 2018 based on MT measurements; and integration of geoscientific data using Leapfrog Geothermal software.

BGF is an excellent example of geothermal activity due to the subduction zone in Central America. The subduction of the Cocos Plate underneath the Caribbean Plate occurs at the Middle America Trench (see Figure 2.1), pushing the rocks to great depths, while magma and heat are transferred towards the surface (DeMets, 2001). Central America is seismically very active due to rapid plate convergence, creating different volcanoes and, in many cases, high-temperature geothermal areas with high potential energy as shown in Figure 2.1 (Snyder et al., 2004). Some of the main geothermal power plants in the region are Berlín (109.4 MWe) and Ahuachapán (95 MWe), both located in El Salvador, Momotombo (77.5 MWe) located in Nicaragua, and Miravalles with a total installed capacity of 149.5 MWe in Costa Rica (SICA, 2021).

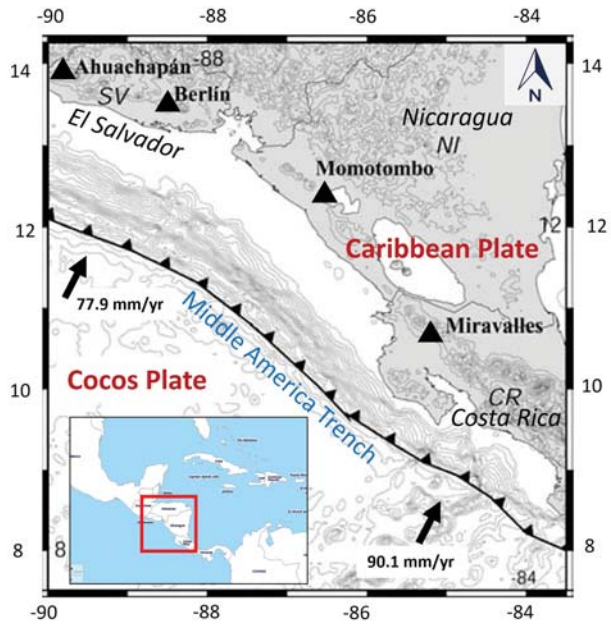


*Figure 2.1. Regional tectonic map of Central America. Location of the most important geothermal fields related to the subduction zone in the Middle America Trench, due to the motion of The Cocos and Caribbean Plate (image modified from Snyder et al., 2004). The inset figure shows the location of the map.*

The geothermal resources potential in Central American countries varies and is reflected in the electricity generation for each operating geothermal power plant, which is mainly located near volcanic areas. The installed electrical capacity in the geothermal power plants in Central America currently reaches 708 MWe. The region has 14 geothermal power plants and approximately 24 areas of geothermal interest for exploration studies (SICA, 2021).

Over the past 32 years (1992-2024), BGF has been in commercial operation through several stages of development. Currently, the installed capacity is 109.2 MWe with a mass flow rate extraction of 798 kg/s, according to the data registered in February 2023 (LAGEO, 2023). The separated water is injected in three different ways: 1. A fraction of the separated water is reinjected at high temperatures (172-180°C) and transported directly from the separators to the reinjection wells; 2. Water is injected at 140°C after transferring heat to the working fluid (Isopentane) of the binary unit, and 3. Water is injected at 60°C by gravity or pumps (LAGEO, 2020).

Since exploitation started in BGF, 45 geothermal wells have been drilled (see Figure 2.2). The production and reinjection wells range from 1,085 m (TR-18A) to 2,690 m (TR-17A) depth and 503.8 m (TR-11A) to 3,455 m (TR-19C) depth, respectively. No new production wells have been drilled in the area during the past six years, which means it is essential to continue the development of the field.

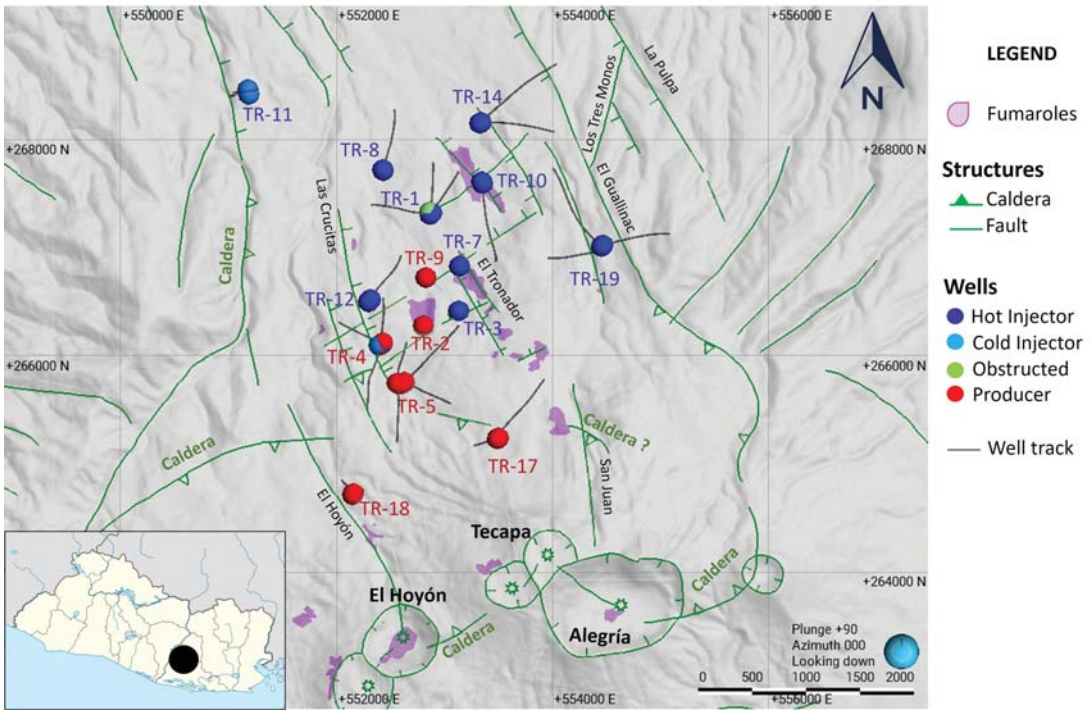


*Figure 2.2. Location map of the geothermal wells in BGF. The inset map shows the location of the geothermal area in the Usulután municipality, El Salvador.*

According to the historical production of the Berlín Geothermal Field, enough geothermal resources are available to drill new production wells in the area (LAGEO, 2023). During 2017-2023, an increase in electrical generation has been identified in Unit I, III, and Binary Unit, except for Unit II (installed capacity of 28.1 MWe), which presents a

decrease of 0.18 MWe per year. However, an increase in enthalpy and flow has been detected in boreholes TR-18A, TR18-B, and TR-5, which the evaporation process and high permeability in the area could explain (LAGEO, 2023).

A section for each geoscientific area is presented in this chapter; the most important findings are highlighted to be subsequently integrated as the most significant contributions to the last conceptual model in 2019.

## 2.1 Geological Overview

In integrating geoscientific data, geological information plays a vital role in characterizing the geothermal system. The geology or geological data help to indicate active/inactive volcanism, stratigraphy, lithology, nature of the hydrothermal alteration, possible age, and structural system of the area. Accordingly, this section briefly summarizes the regional setting, stratigraphic formation, and geothermal manifestations in BGF.

### 2.1.1 Regional setting

BGF is located between 258,000 - 274,000 m latitude and 547,000 - 559,000 m longitude in El Salvador, specifically in the Eastern part of the seismically active subducting margin of Central America (see Figure 2.1). The subduction direction of the Cocos plate is to the NE, but due to the re-distribution of the stress in the on-shore back-arc setting, the maximum horizontal stress ($\sigma_{Hmax}$) in the vicinity of BGF is NW-SE oriented (GESAL, 2003). The evidence for this is from earthquake focal mechanisms shown on the present-day stress map given in Figure 2.3. The main structures in the area have been interpreted as a caldera crossed by a Graben in the NW-SE direction (LAGEO, 2019).

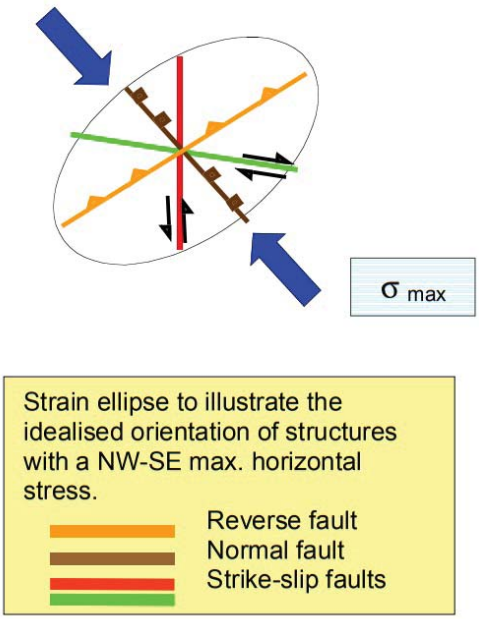


*Figure 2.3. Theoretical Strain ellipse applied to faults in the BGF (GESAL, 2003).*

Intersections of several fault systems are considered by many authors as potential drilling targets (LAGEO, 2019). Nevertheless, it should be noted that faults, in this case, are not clearly visible on the ground, but are often indirectly singled out as photogeological lineaments or discontinuities resulting from particular geophysical modeling (electric, gravimetric) (GESAL, 2003).

Due to these cortical dynamic conditions, the crust's fragile response in this part of the Caribbean plate is observed in four groups of faults: NW-SE, N-S, E-W, and NE-SW. Of these, the most developed are the following (LAGEO, 2019):

**NW-SE:** Identified due to the seismic activity in the area, especially to the west of BGF, near TR-6 and fumaroles are aligned to this normal fault system.

**E-W:** Called dextral transcurrent fault systems (aligned to the Central American graben pattern), corroborated by geophysical studies north of the Mercedes Umaña area and the Lempa River area.

Through photogeological studies and LandSat satellite images, the lineaments or fault systems are classified into three groups (LAGEO, 2019):

1. **NW-SE:** Represents the area's youngest, most active, and essential fault system, associated with the structures through which geothermal fluids rise to the surface layers. The faults are mainly normal faults.

2. **NE-SW:** A less visible system in the area and associated with reverse faulting.

3. **N-S and W-E:** Associated with strike-slip faults with a little normal component.

In BGF, a recent or active volcanic-tectonic activity has been identified. The recent volcanic structures are of Neogene and Quaternary age: Cerro Pelón, Laguna de Alegría (Berlín-Tecapa Volcanic Complex), El Taburete, Usulután, La Manita, El Tigre and Oromontique (LAGEO, 2019). These volcanic structures make up a semicircular structure (see Figure 2.2). According to dating from ignimbrite deposits, the last eruption in the area dates back to 700 years AD. and corresponds to a phreatic explosion originating in El Hoyón (LAGEO, 2019).

### 2.1.2 Stratigraphy and lithology

The Berlín-Tecapa volcanic complex is a stratovolcano formed by alternation of lava flows, pyroclastites, and epiclastites of andesitic to andesitic-basaltic type. It is composed of a series of peripheral volcanic cones, which emerge in the southeastern part of the caldera rim of the ancient Berlín volcano. The last materials attributed to the Berlín volcano are ignimbrites of andesite composition dated at 0.1 My. The ignimbrites are identified on the surface as fan-shaped deposits and are located around the old volcano (LAGEO, 2019). The main geological formations from youngest to oldest are shown in Figure 2.4.

During the period 2012-2018 four production wells were drilled in BGF, which were included in the conceptual model from 2019. The lithology is divided into four lithological units (I-IV) by thin section analysis for microscopic analysis and petrographic data of cores from 27 wells (LAGEO, 2019).

The principal types of rocks are andesite or andesite-basaltic lavas, pyroclastic rocks

like tuff, and ignimbrites. Unit I is made up of superficial materials, e.g., andesite lavas and basaltic andesite rocks alternating with some pyroclastic rocks. This Unit has high permeability corresponding to the superficial aquifer. The thickness of Unit I is between 600 and 800 m. Unit II is made up of pyroclastic rocks with secondary fractures caused by one or more combined factors of cooling, deformation, faulting, jointing, or weathering. Unit III is related to tuff, and Unit IV is made up of andesitic lava and is related to the geothermal reservoir (LAGEO, 2019).

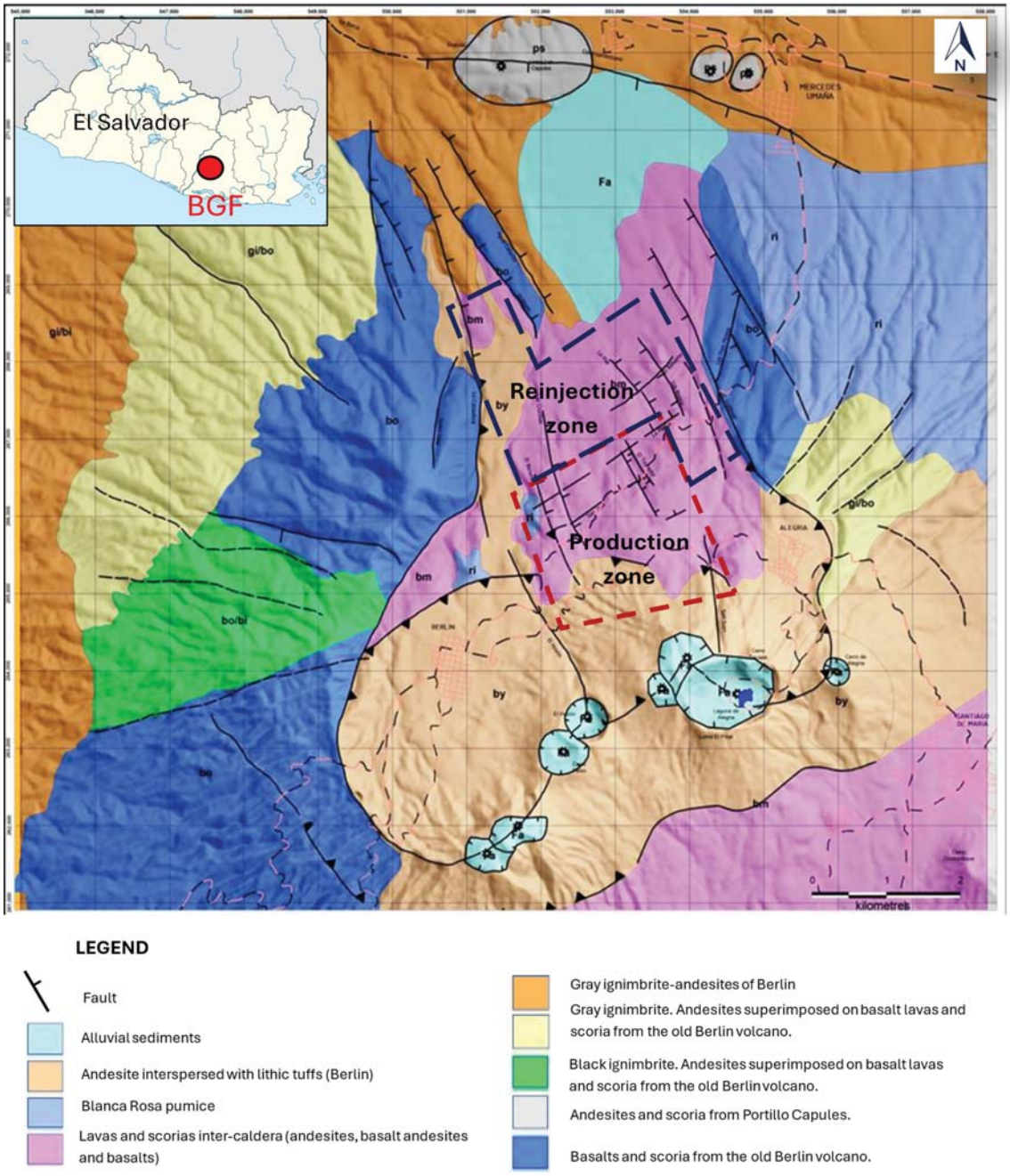


*Figure 2.4. Geological map of BGF (modified from LAGEO, 2019). The dashed blue polygon corresponds to the reinjection zone, and the dashed red polygon corresponds to the production zone. The inset map shows the location of BGF in El Salvador.*

### 2.1.3 Alteration mineral facies

According to the well cuttings samples, BFG has different alteration mineral distribution, changing mainly with depth. The analysis methods used to determine hydrothermal alteration minerals are petrographic microscope and X-ray diffraction analysis. In general terms, the hydrothermal alteration in Berlín is characterized by secondary minerals, like cristobalite, quartz, zeolites, chlorites, epidote, calcite, oxides, hydroxides, and sulfides (LAGEO, 2019).

Based on the rock formation and alteration temperature of secondary minerals, the hydrothermally altered rocks are grouped into five mineralogical facies, argillic, argillic-phyllic, phyllic, phyllic-propylitic, and propylitic. A summary of the mineralogical facies is presented in Table 2.1.

*Table 2.1. BGF mineralogical facies from LAGEO, 2019.*

| **Mineralogical facie** | **Minerals description** | **Temperature [°C]** | **Elevation in the south and north** |
|---|---|---|---|
| Argillic | Clays: smectite and zeolites | 50-150 | 500 m a.s.l. (S)<br>150 m a.s.l. (N) |
| Argillic-phyllic | Clays: quartz, calcite and zeolite | 150-180 | 100 m a.s.l. (S)<br>100 m b.s.l. (N) |
| Phyllic | Less clay, chloride, quartz, calcite and zeolite | 200-230 | 400 m b.s.l. (S)<br>700 m b.s.l. (N) |
| Phyllic-propylitic | Epidote, chloride (penninite) | 230-260 | 950 m b.s.l. (S)<br>1200 m b.s.l. (N) |
| Propylitic | High content of epidote, quartz and calcite | 260-300 | >1200 m b.s.l. |

### 2.1.4 Fumaroles

Fumaroles are geothermal surface manifestations that indicate high temperature and flow at depth. From the fumaroles on the surface, it is possible to evaluate the physical and chemical processes at great depth (Wilson, 1960).

In BGF, 21 fumaroles have been identified (see Figure 2.5). They are located in the southern, central, and northern parts of the area. The fumaroles in the volcanic area contain an acidic pH composition, which is associated with the up-flow located below the volcanic structures (El Hoyón-Laguna de Alegría). In the central part, the fumaroles show a neutral pH composition and are in the surroundings of the high-temperature wells. Finally, in the north, the fumaroles are associated with the discharge and have an intermediate pH composition (LAGEO, 2019).

According to chemical analysis of gases in 2018 the Tronador fumarole, located in the northern part of the field, indicated the highest measured temperature, 98.9°C (see Figure 2.5). This could be associated with the entry of primary steam from a greater source depth of geothermal fluids. The fumaroles, El Hoyón (96°C) and La Laguna de Alegría (93.8°C) are of deep origin with magmatic influence (LAGEO, 2019). The high temperatures in the fumaroles located in the north (>98°C) could be related to the

permeability in the area due to the intersection of El Tronador and La Pila (NW-SE faults), and El Bálsamo and La Planta (NE-SW fault) (LAGEO, 2019).

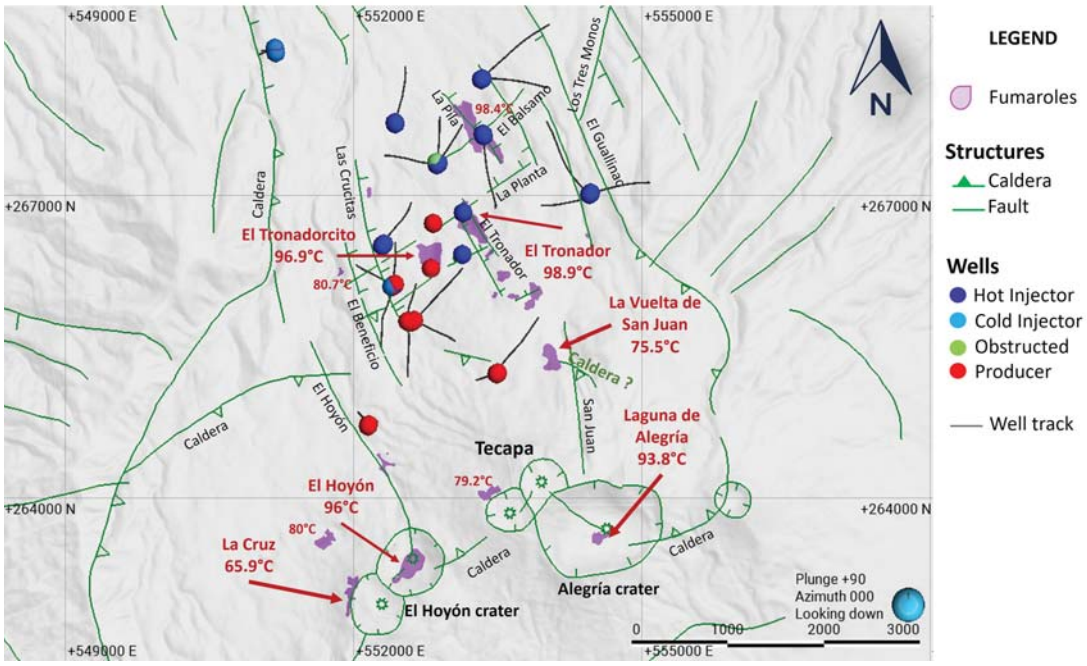


*Figure 2.5. Location map of fumaroles in the BGF. The map shows the crater of Alegría, El Hoyón, and Tecapa volcanic cones, the structural system and geothermal wells.*

## 2.2 Geochemistry

Geochemistry provides information about the type of surface thermal manifestations, the location of upflow zone, outflow zone, water origin, and deep reservoir temperature prediction. Different geochemical studies have been carried out in Berlín, of which the most notable are chemical analysis of surface water outcrops, isotopes analysis of gases and geo-temperatures of fumaroles, measurement of diffuse gases in the soil, geochemical and isotopes analysis, and geothermometry in the well fluids. This section briefly summarizes the main findings to characterize the geothermal reservoir of BGF.

### 2.2.1 Fumaroles

The chemical data analysis of fumaroles indicates that few of them are fed by primary steam, which is associated with a direct connection with a deep source. Other fumaroles are fed by gases from superficial aquifers heated up by convection. Finally, the high concentration of $H_2$ in fumaroles in the south of the field is related to the high temperature in the volcanic complex of Berlín-Tecapa, which gases are due to the magmatic degasification process (LAGEO, 2019).

The gas measurements in fumaroles indicate the existence of two upflows, one associated with the southern zone, specifically in the area of the Berlín-Tecapa volcanic complex, and the other close to the TR-5 and TR-4 wells (LAGEO, 2019).

### 2.2.2 Geothermometry

Geothermometer is the only method to evaluate temperatures related to the geothermal reservoir. Its applications constitute one of the most important tools for the exploration and development of the resource, which leads to providing essential information about the nature of the system and fluids. This section describes the application of chemical and isotopic geothermometry to both natural spring discharges and well fluids at BGF.

In 2013, a new fumarole was found in a fissure located in El Hoyón crater. The geothermometers calculated for these fluids gave temperatures ranging between 285 and 310°C. These values are similar to the temperature calculated in fluids from wells, which is around 300°C (LAGEO, 2019).

The reservoir is considered a saline aquifer with chlorine-sodium neutral characteristics. It has fissured tuff and andesite lavas with high hydrothermal alteration (propylitic facie). According to the cation and gas geothermometers, the temperature is between 260 and 300°C, and 340 and 350°C, respectively. The chemical composition of the El Hoyón fumarole is probably the most representative one of the gas composition of the deep reservoir since it presents the lowest $CO_2/H_2S$ ratio and the maximum temperature calculated with the D'Amore and Panichi geothermometer (LAGEO, 2019).

Figure 2.6 shows the relationship between chlorine and boron of several production wells in the area, where it is possible to observe differences between the physical processes of the geothermal fluids (LAGEO, 2019). For example, boiling processes occur in wells TR-2, TR-3, TR-9, and TR-17, while in well TR-18, an experimental dilution process is possibly due to water mixing at great depth. However, according to the linear correlation shown in Figure 2.6, the fluids in all production wells have the same origin.

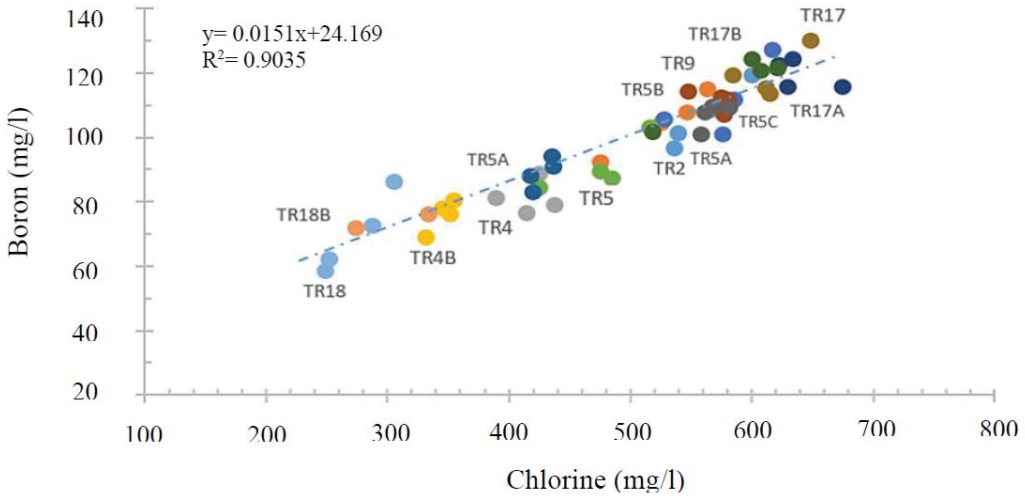


*Figure 2.6. Relationship between chlorine and boron concentration in the production wells in BGF (LAGEO, 2019).*

Geochemical studies helped define two ascent zones: the characterization of fluids emanating from a fissure formed in 2013 in the crater of the El Hoyón volcano (see Figure 2.5) indicates that they are deep fluids with temperatures around 300°C (NaK geothermometer), and in the center of the geothermal field (TR-4 zone) with similar characteristics. In addition, the isotopic composition in the wells located in the south

part indicates an equilibrium temperature between 340 and 350°C. Therefore, based on various information like geo-volcanology, $H_2$, and the temperature measured in the wells, the upflow zones are close to the TR-17 and TR-18 platform and TR-4 and TR-5 platform (LAGEO, 2019).

## 2.3 Geophysical Overview

Geophysical studies provide essential information about geothermal areas; some elements of interest are:

- Subsurface extent of the geothermal system.
- Areal extent and thickness of the reservoir.
- Location of the heat source, and
- Subsurface structures (faults and fissures)

Resistivity soundings, mainly based on the Time Domain Electromagnetic (TDEM) and magnetotelluric (MT) measurements, are the most common geophysical methods used during the exploration stage of geothermal areas due to their resolution and depth of penetration. However, analysis of natural earthquakes, magnetic and gravity surveys are also helpful, both in the exploration stage but also for monitoring purposes during production (Bromley, 2018). Combining all geophysical methods improves the interpretation and identification of the areas of interest and helps to understand the changes in the geothermal system during production. In BGF, three geophysical methods have been applied: MT/TDEM resistivity, gravity, and passive seismic. The most important results are briefly described below.

### 2.3.1 MT/TDEM method

The MT method is a powerful geophysical method that can image the resistivity structure of the subsurface of the Earth down to tens of km in ideal conditions. It uses natural electromagnetic fields. The basic principle of this passive method is that it uses alternating currents induced in the ground by natural oscillations in the Earth's magnetic field, and the measured signal is the electric and magnetic field at the surface. The magnetic ($\vec{H}$) and electric field ($\vec{E}$) are measured as a function of time to calculate the apparent resistivity (Hersir et al., 2022).

The TDEM method is an active geophysical method used to obtain information on the subsurface resistivity (or conductivity) with a penetration depth not higher than 1 km. This method uses a controlled, known, time-varying artificial magnetic field to induce constant currents within the Earth according to the Bio-Savart law. The current is abruptly turned off, and a secondary decaying magnetic field from the induced subsurface current is measured. The decay rate of the magnetic field over time depends on the current distribution, which in turn depends on the resistivity structures of the Earth. The induced voltage, as a function of time, after the current is turned off, can therefore be interpreted in terms of the subsurface resistivity structure (Hersir et al., 2022).

Prior to the last conceptual model of BGF in 2019, 129 MT/TDEM soundings had been carried out. In 2018, a new 3D resistivity model was created using the 129 already existing MT/TDEM soundings and additional 13 new MT/TDEM soundings located in the center, northwest, and south of the field. The MT data were static shift was corrected by using collocated TDEM data before the 3D inversion (2005, 2010, and 2018). The first 3D MT model was made by Geosystem in 2005, the second by WesternGeco in 2010, and the last model by LaGeo in 2018, using remote access to CGG Milan Cluster of Geotools company (CGG) (Campos, 2019).

Figure 2.7 shows a N-S lying resistivity cross-section based on 3D inversion of MT data in 2018. There are three main layers; a low-resistivity layer consisting of altered clay minerals (smectite) and resistivity <10 $\Omega m$; a transition zone of the geothermal system, with resistivity between 10 and 30 $\Omega m$; and the production reservoir with resistivity between 30 and 90 $\Omega m$, extended to the south of the production zone (Campos, 2019).

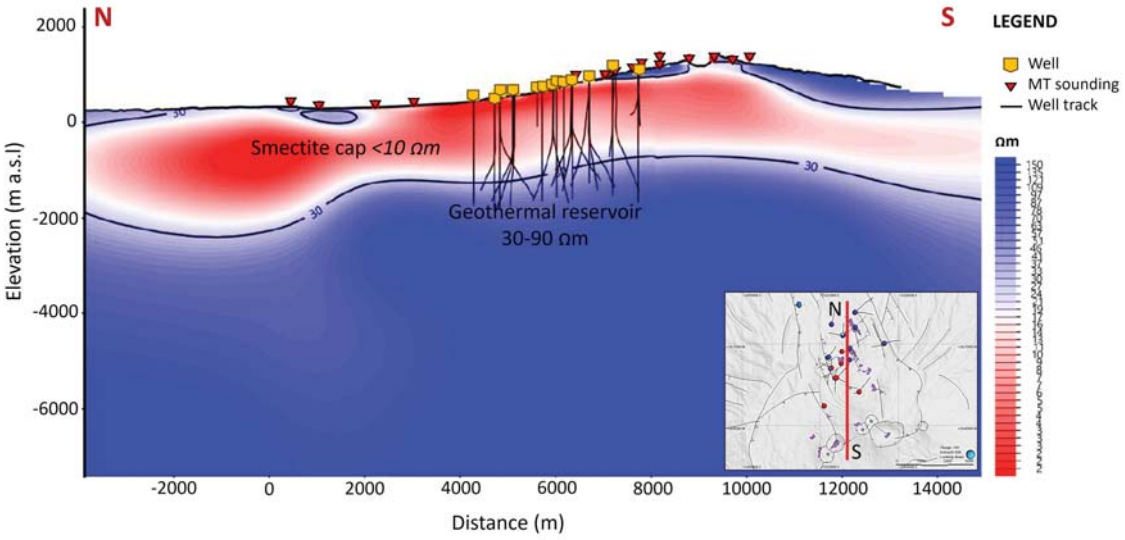


*Figure 2.7. A N-S lying resistivity cross-section based on 3D inversion of MT data (Campos, 2019). The cross-section shows the 30 Ωm contour that represents the top of the reservoir (black contour), the smectite cap above the reservoir with resistivity < 10 Ωm, the location of the geothermal wells close to the profile (yellow boxes and black tracers) and MT/TDEM soundings (red inverted triangles). The inset map shows the location of the cross-section. Image modify from Campos, 2019.*

### 2.3.2 Gravity method

The gravity method is a geophysical prospecting method applied in geothermal resource exploration. The method is based on measuring variations in the acceleration of the gravity field caused by lateral variations of density in the subsurface (Hersir et al., 2022). Differences in rock density produce small changes in the Earth's gravitational field that can be measured using a portable instrument known as gravimeter. Density contrasts may well be related to basement depth variations, rim caldera, instrusions, rock alteration, porosity variations, faults, or dykes (Hersir et al., 2022). A gravimeter is a passive, low-impact, non-invasive geophysical tool that can be applied for different exploration purposes.

The gravity results presented in the Conceptual Model in 2019 were obtained from 684 measurements carried out in 2000, 2008, and 2016. A Bouguer anomaly, Residual Bouguer anomaly, and first horizontal derivative maps were derived from the reduced gravity. However, in this section, only the Complete Bouguer Anomaly (CBA) is shown.

Figure 2.8 shows the CBA map representing the most profound gravity changes. The central aspect observed is the high gravity values between 30 and 40 mGal to the southwest, south, and near the geothermal wells (extraction zone). It has been proposed that the high values are limited in the north by the boundary of the old Berlín caldera; however, the boundary is not visible on the surface (Canjura, 2016). In the north, the limit is close to well TR-9 and TR-1. On the west and east sides, the limits are represented by the Berlín caldera-La Calzadora and Guallinac faults, respectively. The lowest values of the gravity anomaly between 20 and 25 mGal are associated with the injection zone. The E-W trend in the northern part of BGF is associated with the regional structures of the Central Graben (Canjura, 2016).

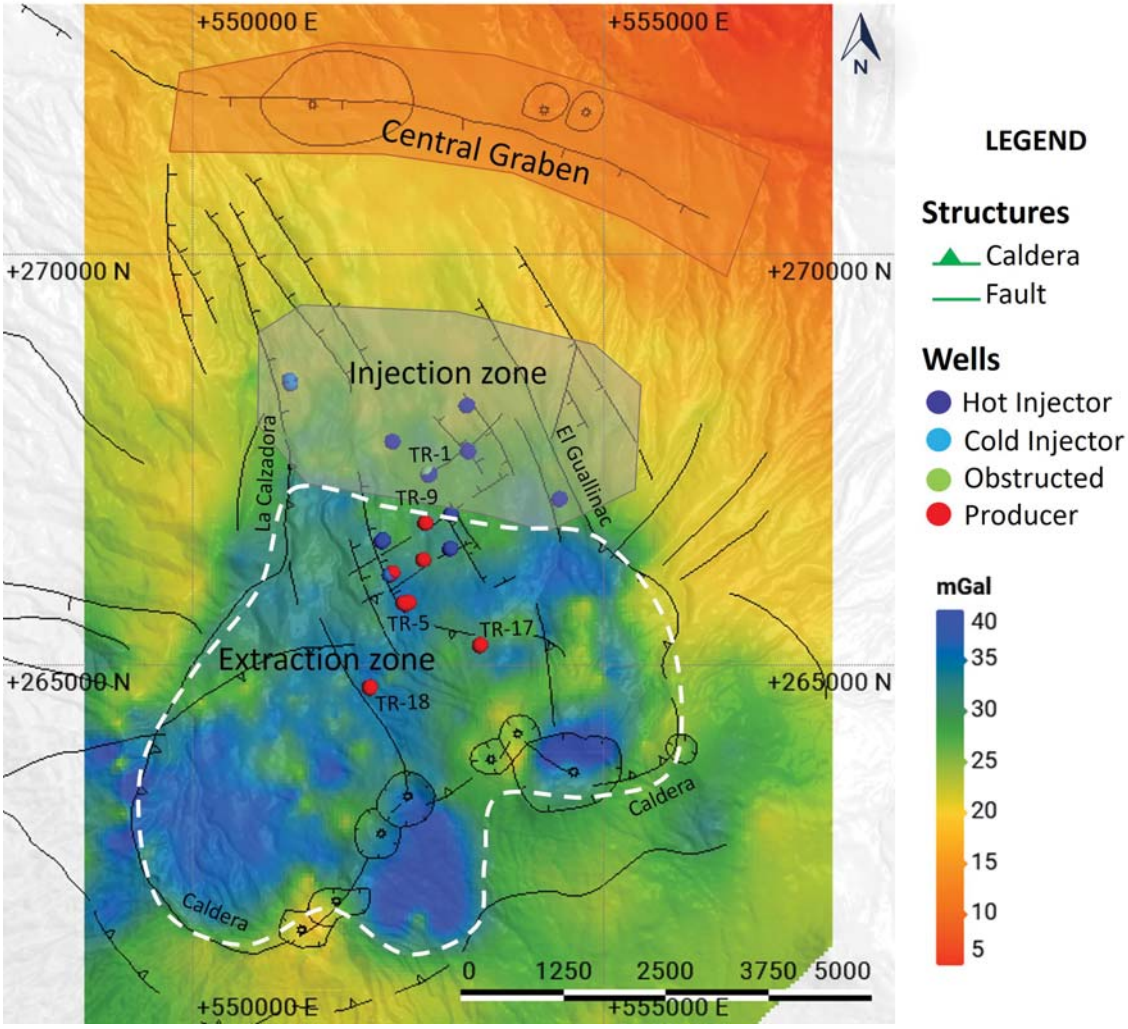


*Figure 2.8. Complete Bouguer Anomaly (CBA) map, using a density $\rho = 2.3\ g/cm^3$ for Bouguer and terrain corrections. The dashed white line corresponds to the highest gravity values (>30 $g/cm^3$ ) in the extraction zone. Map modified from Canjura, 2016.*

### 2.3.3 Passive seismic method

The passive seismic method utilizes natural earthquakes and seismic noise to extract information on the interior of the geothermal system. The basic principle of the passive seismic method is the detection of natural low-frequency earth movements, usually to discern geological structures and locate underground sources or bodies such as oil, gas, or steam. In geothermal exploration, this method helps identify the brittle-ductile boundary, heat sources, and permeable zones by fracturing related to geothermal fluid extraction and injection and their interaction with geothermal fluids (Hersir et al., 2022).

A condition of stress to build up in the Earth's crust and causing earthquakes is that the rock is brittle and behaves elastically. If the rock is ductile, it will creep as a consequence of external stress and no earthquakes will occur. The big majority of earthquakes occur in the brittle part of the Earth's crust, and the boundary between the brittle and ductile crust depends on the type, temperature, and pressure of the rock, but also on the strain rate. The depth distribution of earthquakes, therefore, gives important information on the physical state and properties of the crust, including temperature constraints (Hersir et al., 2022).

The seismicity in the BGF area was recorded in 2013-2019. The hypocenters were compared with the resistivity model based on 1D inversion (see Figure 2.9). The possible presence of a body with ductile properties at approximately 6,000 m b.s.l was identified from the seismic studies due to the absence of earthquakes, and a deep conductive anomaly according to the 1D MT model, which is related to the heat source is assumed at 6,000 m b.s.l. (LAGEO, 2019).

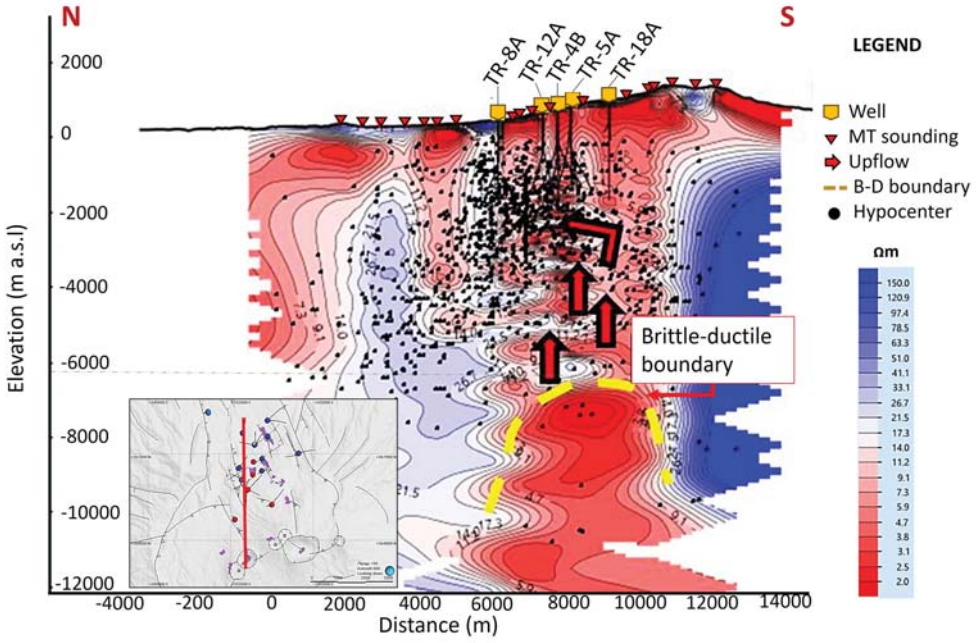


*Figure 2.9. Comparison between the resistivity model based on 1D inversion and earthquake's location (black dots) recorded in 2013-2019. N-S profile shows the upflow in red arrows and the brittle-ductile boundary in dashed yellow line. The inset map shows the location of the cross-section. Image modified from LAGEO, 2019.*

## 2.4 Conceptual model (2019)

A conceptual model is a schematic summary of extensive information from different geoscientific studies. All the data and information are combined and integrated into a unique model of the system to be tested by exploration drilling. In BGF, the static conceptual model includes different data sets and interpreted models from different disciplines, e.g., geology, geochemistry, geophysics, and well data (temperature profiles) presented as 2D cross-sections and maps of the geothermal system. An example of a joint interpretation of resistivity and earthquakes is shown in Figure 2.9. Additionally, in this updated version of the conceptual model, all field data were combined into a 3D geological model using Leapfrog Geothermal software.

From the Geophysical point of view, the reservoir of the Berlín geothermal field is regarded as the upper part of a deep resistive dome, identified by MT, with resistivities in the range of 40 to 90 $\Omega m$. The thickness of this reservoir, estimated from MT anomalies and correlation of measured temperature records (T-thermal recovery profiles), ranges from 600 to 1000 m (see Figure 2.10).

The reservoir is located in a sequence of andesitic lavas and compact fractured tuffs, which present a strong hydrothermal alteration (propylitic facie). It is a saline aquifer of the neutral sodium chloride type, with temperatures of cationic geothermometers in the range of 260 to 300°C, and 340 to 350°C according to the gas geothermometers (LAGEO, 2019).

In the southern sector of the Berlín geothermal field, the aquifer is associated with fractured zones that correspond with permeable horizons and the planes of the NW-SE and NE-SW faults located within the structures of the graben and the Berlín caldera. The permeable zones are found in lithological Unit IV.

The smectite layer is made up of fine tuffs from lithological Unit III. It has been observed that this layer is found at a shallower depth in the southern zone, in wells TR-17 and TR-18, compared to the wells located in the center of the field. This layer is characterized by a conductive layer with values less than 10 $\Omega m$.

The heat source of the Berlín geothermal system is associated with a recently formed magmatic body located under the Berlín-Tecapa volcanic complex, which is predominantly andesitic (LAGEO, 2019). The resistivity model based on the 1D inversion of MT/TDEM data indicates low resistivity which is probably related to the heat source, could be magmatic (cooling intrusive). The hypocenters of seismic events recorded between 2013 and 2019 indicate the brittle-ductile transition zone, related to the probable heat source at -6000 m a.s.l. (see Figure 2.10)

Two upflow zones of deep fluid have been identified, and their outflow is lateral from the southern to the northern part of BGF (see Figure 2.10). One upflow zone is related to the Berlín-Tecapa volcanic complex. The other upflow zone is related to the area near the TR-4 and TR-5 wells, where the top of the geothermal reservoir is at around -1,000 m a.s.l.; furthermore, in this zone, the lithological Unit IV has been identified, and the temperature according to the alteration minerals of the propylitic facie estimated of 300°C. In the other upflow, the hot fluids could rise through the northern edge of the Blanca Rosa caldera, they are cooled by meteoric recharge and reach more directly to

the area of borehole TR-5 and TR-4 (LAGEO, 2019).

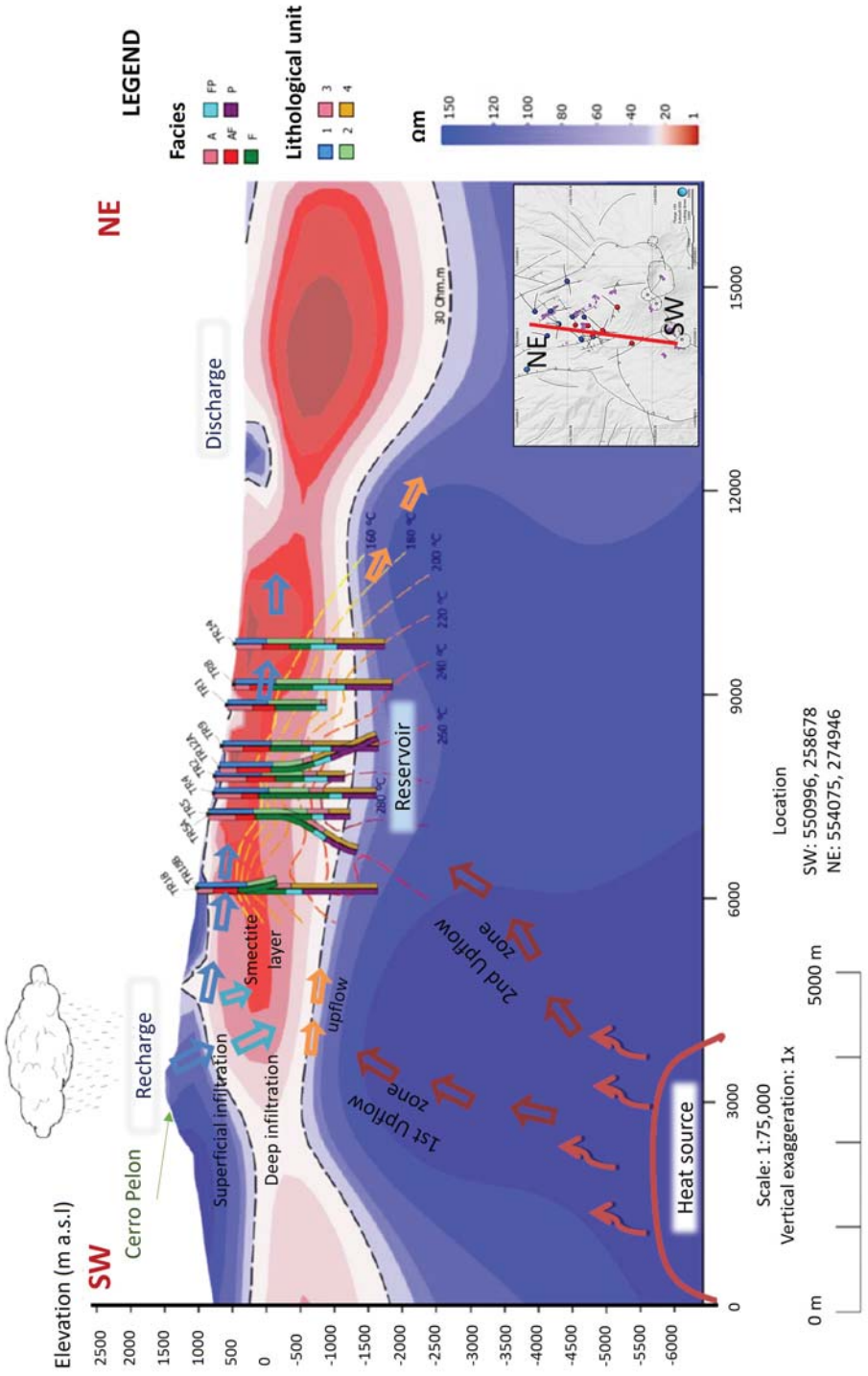


*Figure 2.10. SW-NE cross-section of BGF conceptual model. The hydrothermal alteration facies, lithological units, isotherms, and flow patterns are shown. The inset map shows the location of the cross-section. Image modified from LAGEO, 2019.*

# 3 3D inversion of gravity data

Inversion of gravity data is a tool that can be used to estimate the density distribution in the subsurface. Several inversion techniques have existed for many years, which have been studied and, in a certain way, developed to the present day. The most recent studies include the characterization of the Guemassa massif in Morocco (Soulaimani et al., 2020), in Way Ratai area (Sarkowi & Wibowo, 2021) and others to delineate subsurface structural geometry in a geothermal system (Omollo & Nishijima, 2023) and combining magnetic and gravity data inversion to delineate geothermal systems (Didas et al., 2022). The gravity data inversion can lead to linear or non-linear approaches depending on the method's choice or the problem to solve. However, the problem inherent to all inversions is the non-uniqueness of the solution, which means many solutions can correspond to the density distribution of the study area.

The results of the geophysical inversion are essential as they serve as a guide to show where and how the boundaries of the geothermal system may need to be adjusted. Gravity modeling has significant importance at both the exploration and monitoring stages of geothermal areas. This technique provides essential data for understanding subsurface density variations related to faults, fractures, and magma intrusions, as well as the presence of hot fluid, which are potential sites for drilling new wells. To confirm some structures, such as faults, fractures, or caldera rims, a complementary analysis of gravity gradient has been applied in the area of interest.

In this study, three-dimensional geophysical inversion of gravity data has been performed to characterize the geothermal system in BGF, El Salvador using the Oasis Montaj software (Inc, 2023) by Seequent Company. Geophysical density modeling was implemented in two different ways: (1) entirely unconstrained (i.e., no geological data included), (2) constrained by the 3D resistivity model using homogeneous rock unit densities corresponding to the conductive layer consisting of the smectite cap of the geothermal system, and (3) constrained by the bulk density of granite intrusive and altered andesite lavas in boreholes TR-19B and TR-19C by petrophysical analysis.

## 3.1 Gravity data

Several gravity surveys have been carried out in BGF since 2000, these consist of a total of 684 gravity points, of which 207 are from the last campaign in 2016. The measurements aimed to identify the possible extension of the NW-SE fault system towards the northern part of BGF (see section 2.1.1).

The data were collected in 2000, 2008, and 2016, and the average distance between each gravity point is approximately 250 m. The gravity data were previously processed and corrected by experts from LaGeo using the GravMaster and WinGLink software

to obtain a Complete Bouguer Anomaly (CBA) using $\rho = 2.3\ g/cm^3$. The results are shown in section 2.3.2.

In this study, the data were reviewed, and some points were removed, assuming they were outliers (Figure 3.7.a and 3.7.b clearly show these outliers and why they were removed). The total number of gravity points considered in this study was 656 out of 684. The new dataset was analyzed using two different interpolation methods (Kriging and minimum curvature) to observe their statistical results and decide on which method to use before applying filters and creating the 3D density models. The distribution of the gravity points around the geothermal system is shown in Figure 3.1.

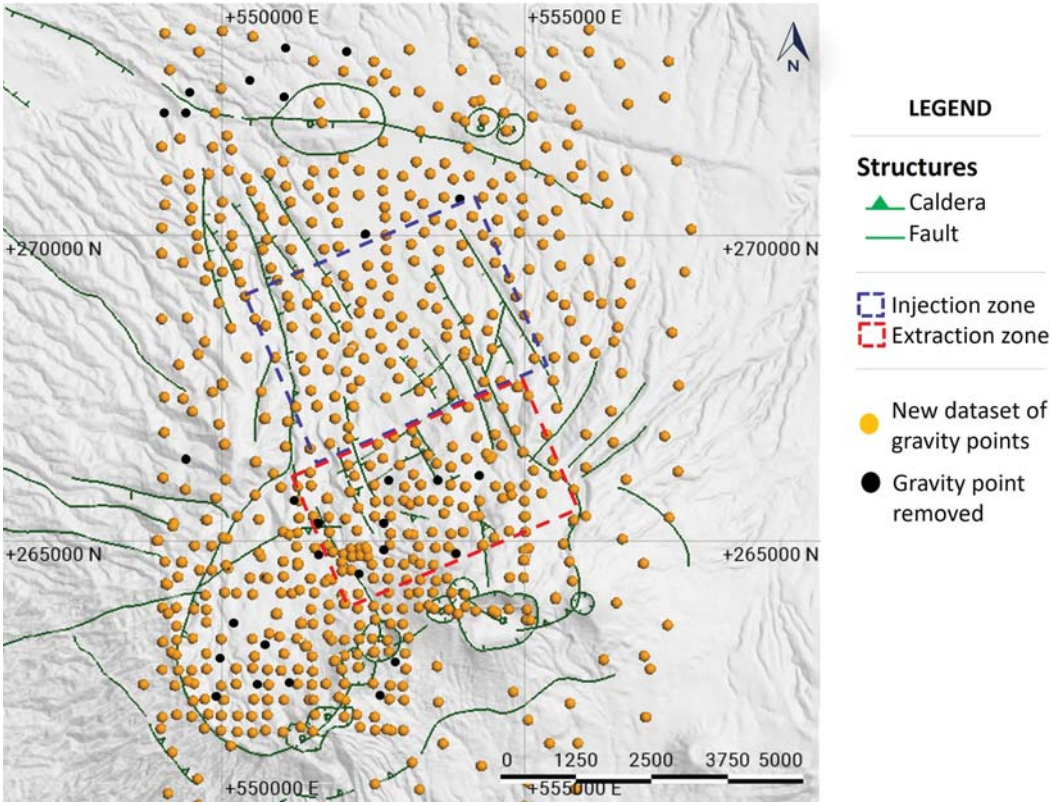


*Figure 3.1. Map of gravity points distribution in BGF. The map shows the structural system in green lines, the new data set of gravity points 656 (yellow dot), and the removed gravity points (black dot).*

## 3.2 Interpolation and statistical analysis

This section evaluates the differences in gravity changes using a statistical analysis tool from Oasis Montaj software. For this part, the data must be in the form of a grid to be processed. Therefore, the gravity data must be converted, usually distributed arbitrarily in the survey area, into a uniform grid by gridding.

Before having our final grid of gravity data interpolated, two different interpolation methods are analyzed to verify which one is more confident according to the statistical results, dummies (fictitious values), and valid data. The dummy values result from the blanking distance specified in the interpolation setting; this means the grid cells

farther than the blanking distance value from a valid point will be set to dummies in the output grid. Usually, the blanking distance should be set to a value just greater than the maximum distance through which interpolation is desired. The equation varies for each interpolation method used (Seequent, 2023). These are described below.

The Kriging method is a geostatistical gridding technique for randomly distributed data, non-parallel line data, or orthogonal line data. The method is used if the data are not sampled along lines that run roughly in the same direction; it is variable between sample locations or clustered. The method is ideally suited to geochemical or other geological sample-based data; it is rarely used for geophysical data, which tends to follow a natural smooth surface. The equation to calculate the blanking distance for the Kriging method is shown in Equation (1) (Seequent, 2023).

The minimum curvature gridding method fits a minimum curvature surface, which is the smoothest possible surface that will fit the given data values. The process is suitable for data with a relatively large number of samples (it can work well with geochemical data from comprehensive regional and local surveys), and it is best used when data are randomly distributed, sampled along arbitrary lines, or if one wants to include tie lines. The equation to calculate the blanking distance for the minimum curvature method is shown in Equation (2) (Seequent, 2023).

$$2\sqrt{\frac{Area_{grid}}{\#Data\,points}} \tag{1}$$

$$2\sqrt{\frac{8 * Area_{grid}}{\#Data\,points}} \tag{2}$$

Where: $Area_{grid}$= $X$ * $Y$, $X = 9,100\ m$, $Y = 14,700\ m$ and #Data points=656.

Figure 3.2 and 3.3 show the grid preview pane of Kriging and minimum curvature results for the 656 gravity points, respectively. The graphs next to each map show the statistics calculated for each method, which includes the minimum value, the maximum value, the arithmetic mean, the median, the standard deviation, the number of valid points, and the number of dummy points. These are calculated for the entire selected data set.

For the statistical analysis, the best grid corresponds to the one with a low standard deviation; in other words, the grid of a data set that deviates the least from a normal Gaussian distribution. In reality, data are rarely perfectly Gaussian; however, to use better-distributed data, the results are more reliable (Livingston, 2004). The standard deviation in the Kriging method is 0.12 lower than for the minimum curvature method, which is not significant but suggests a better distribution of gravity data using the Kriging method. This is reflected in the normal Gaussian distribution plot shown in the inlet graph in Figure 3.2 and 3.3.

The statistical results show that the mean, standard deviation, and median values are slightly different for the two methods; however, the valid items and dummies are significantly different. In this sense, it is recommended to use the criteria of less amount of dummy data and more valid data rather than a lower standard deviation value.

Using the Kriging method results in 554 dummies while the minimum curvature method results in 397 dummies. However, the standard deviation is 0.12 lower for the Kriging method than for the minimum curvature method.

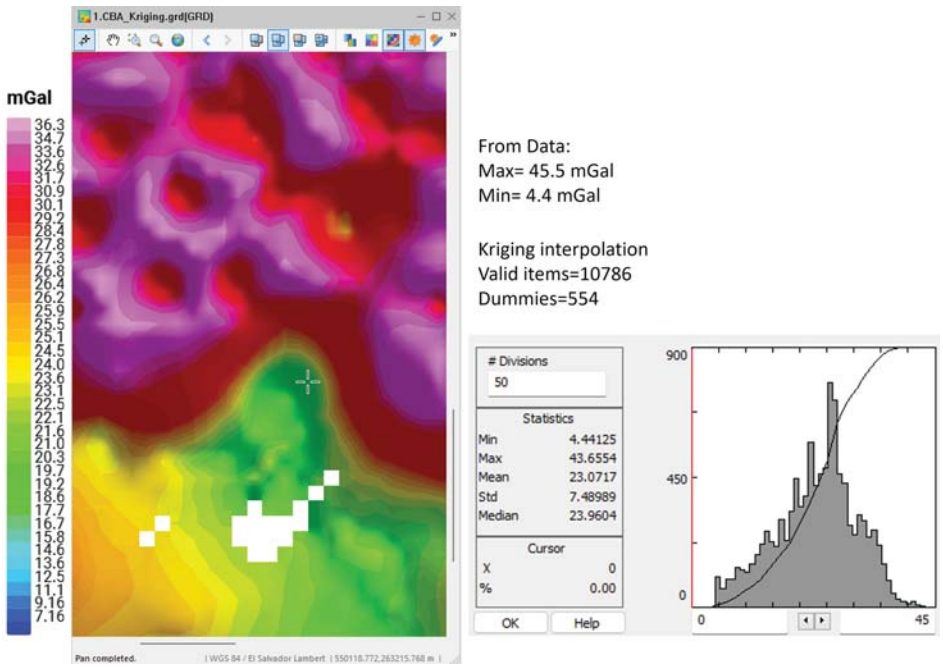


*Figure 3.2. Kriging curvature interpolation method for a section of gravity points. The inlet graph shows the statistical data for the method.*

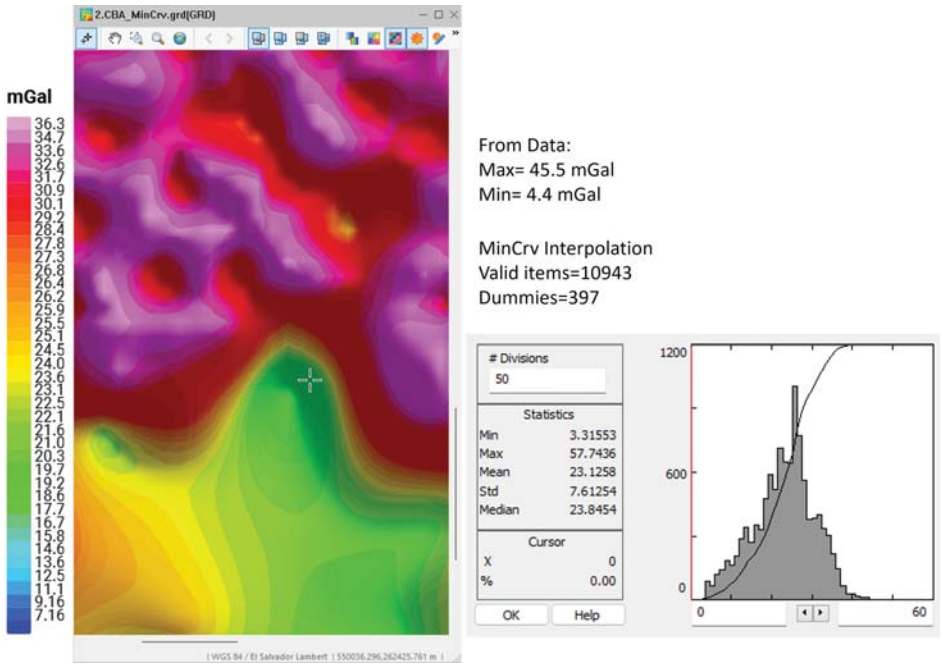


*Figure 3.3. Minimum curvature interpolation method for a section of gravity points. The inlet graph shows the statistical data for the method.*

To create the interpolated grid using the minimum curvature method, it is necessary to define the grid cell size (the distance between grid points in the X and Y directions),

which should normally be 1/4 to 1/2 of the line separation or the nominal data sample interval. If not specified, the data points are assumed to be evenly distributed, and the area rectangular. The default size is then defined by Equation (3).

$$\frac{1}{4}\sqrt{\frac{Area_{grid}}{\#Data\,points}} \tag{3}$$

The Complete Bouguer Anomaly (CBA) using the minimum curvature method is shown in Figure 3.4. The gravity value vary from 4.4 to 45.5 mGal. A low gravity anomaly is found in the northern part of the area. The anomaly pattern may correlate with the presence of low-density rocks, the injection fluids in the area, and the Central Graben in the north. Moreover, high gravity anomaly can be observed in the CBA map and aligned with the caldera's boundaries, El Guallinac and La Calzadora Fault. This resulting grid is used for filtering and mapping before creating the 3D density model.

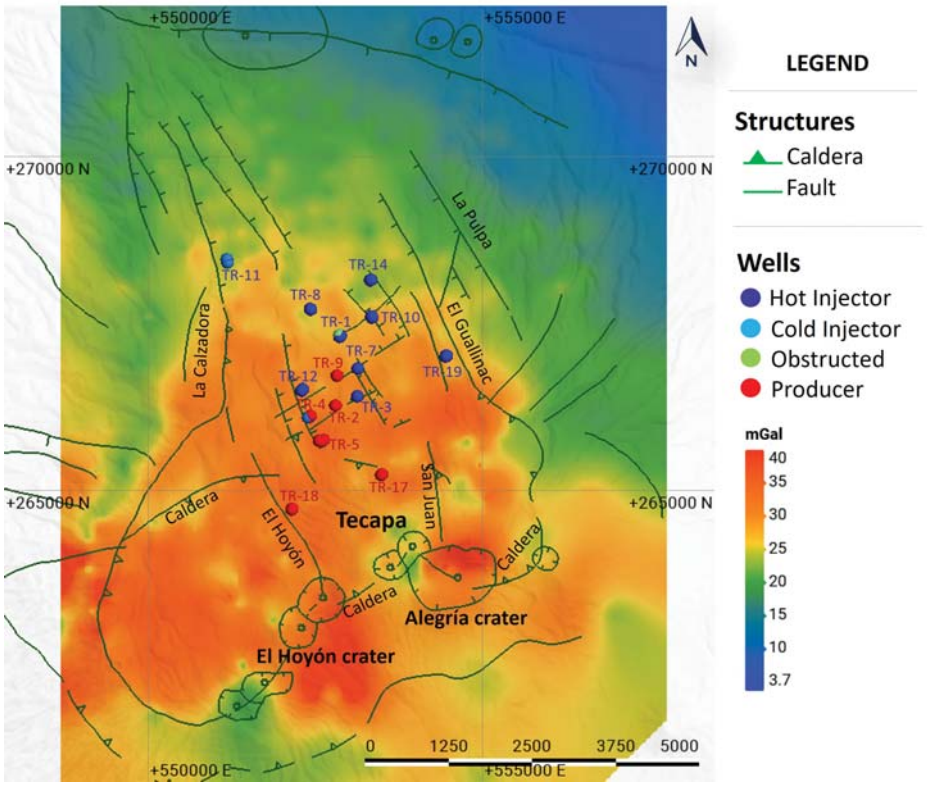


*Figure 3.4. Complete Bouguer Anomaly ($\rho = 2.3\ g/cm^3$). The interpolation method is the Minimum Curvature method with a cell size=112 m and blanking distance=1277 m.*

## 3.3 Regional and residual anomaly

The gravity data are commonly presented in two ways (residual and regional anomalies) often through Fourier spectrum analysis from the CBA values. The residual anomaly is caused by local density contrasts related to subsurface faults and superficial sources. In contrast, the regional anomaly is due to more regional changes related to the most profound sources, such as intrusive bodies and a geothermal reservoir.

After correction for instrumental drift, latitude, solar and lunar effects, elevation, mass between the measurement site and the geoid, and terrain, a map of gravitational acceleration, the CBA map, is presented. The CBA value for each gravity station used in this study was calculated using a density of 2.3 $g/cm^3$. The 2.3 $g/cm^3$ represents the average density of the rocks in the area and is the density commonly used for gravity surveys in the BGF in El Salvador. The corrections of the gravitational acceleration were made by experts at LaGeo in 2016 (Canjura, 2016).

In this study, Low and High-Pass Butterworth filters were used to calculate the residual and regional anomaly, respectively. Before applying the filters, the Fast Fourier Transform (FFT) was applied to infer the depths of the different sources. The depth of an ensemble of sources is determined by measuring the slope of the energy (power) spectrum and divided by 4. The power spectrum of the gravity data in Figure 3.5 can be divided into four parts (slopes) - a deep source component (Slope1), two shallow source components (Slope2 and Slope3), and a noise component (Slope4).

Figure 3.5 shows the wavelength (m) on the X-axis and the Y-axis in the log(power) of the CBA. This is because the grid (in the space domain) is transformed to the wavelength domain using the Fast Fourier Transform (FFT).

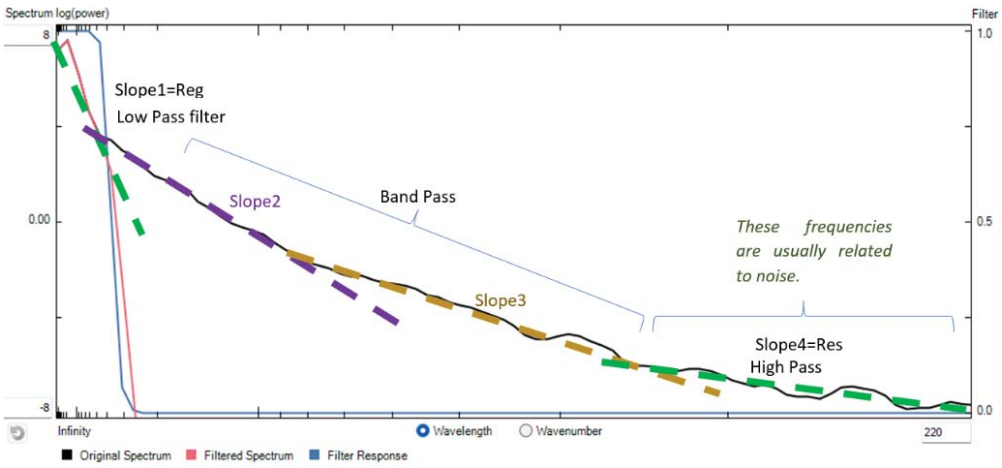


*Figure 3.5. Energy spectrum profile of the gravity data. The wavelength is shown on the X-axis decreasing along the X-axis (towards the right on the graph) towards the high frequencies slope (Slope4) and increasing towards the low frequencies slope (Slope1). The spectrum log(power) is shown on the Y-axis.*

The regional and residual anomalies of the CBA were calculated using spectrum analysis with 10% of the square expansion and the maximum entropy grid fill method. The square expansion is recommended because it minimizes side effects that result from having different wavelength samples in the $X$ and $Y$ directions; in this case, 10% of the average grid coverage is used. To apply the FFT routine requires a filled and periodic grid, which means all dummy areas are extrapolated using the real data that are located in their immediate vicinity (Seequent, 2023). This study uses the default grid fill method called maximum entropy.

Finally, the CBA values were filtered using three different filters: Butterworth Low Pass (cutoff wavelength=3670 m and filter order=15), Butterworth Band Pass (cutoff wavelength range=3670-407 m and filter order=15), and Butterworth High Pass (cutoff

wavelength=407 m and filter order=15), to get the deepest, intermediate, and superficial anomalies, respectively. The interpolation indicates that the most residual part could be related to noise, which should not be considered in the 3D inversion model. Figure 3.6 shows the four grids:

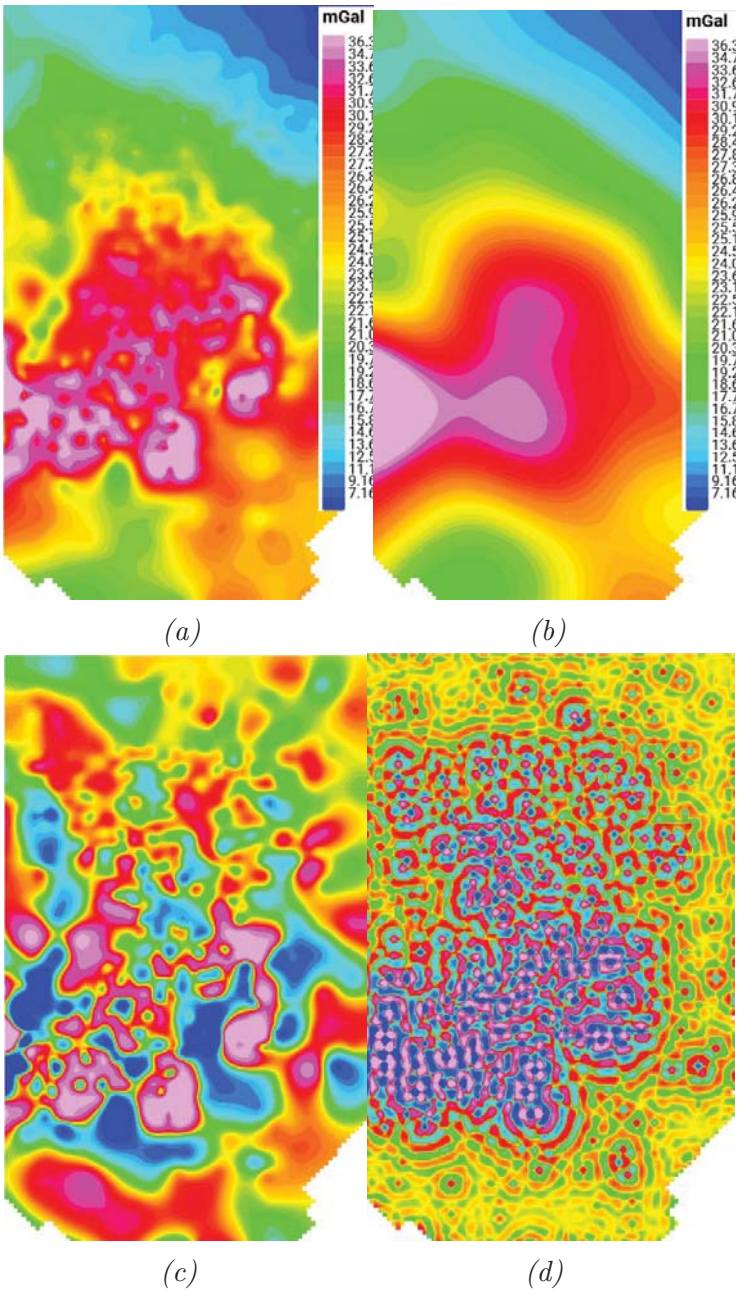


*Figure 3.6. a) New CBA grid using the minimum curvature method, b) Butterworth Low-Pass filter, c) Butterworth Band-Pass filter, and d) Butterworth High-Pass filter.*

The Grid Math toolbox of Oasis Montaj was used to remove the noise part shown in the power spectrum (see Figure 3.5). In this part, a new grid that represents the clear signal of CBA is derived using the sum of the regional grid (Low-Pass Filter or LP) and the intermediate grid (Band-Pass Filter or BP) shown in Equation (4). Figure 3.7 shows the result of the new CBA grid, which is very similar to the original one.

$$\boldsymbol{C}BA_{csignal} = CBA_{LP} + CBA_{BP} \tag{4}$$

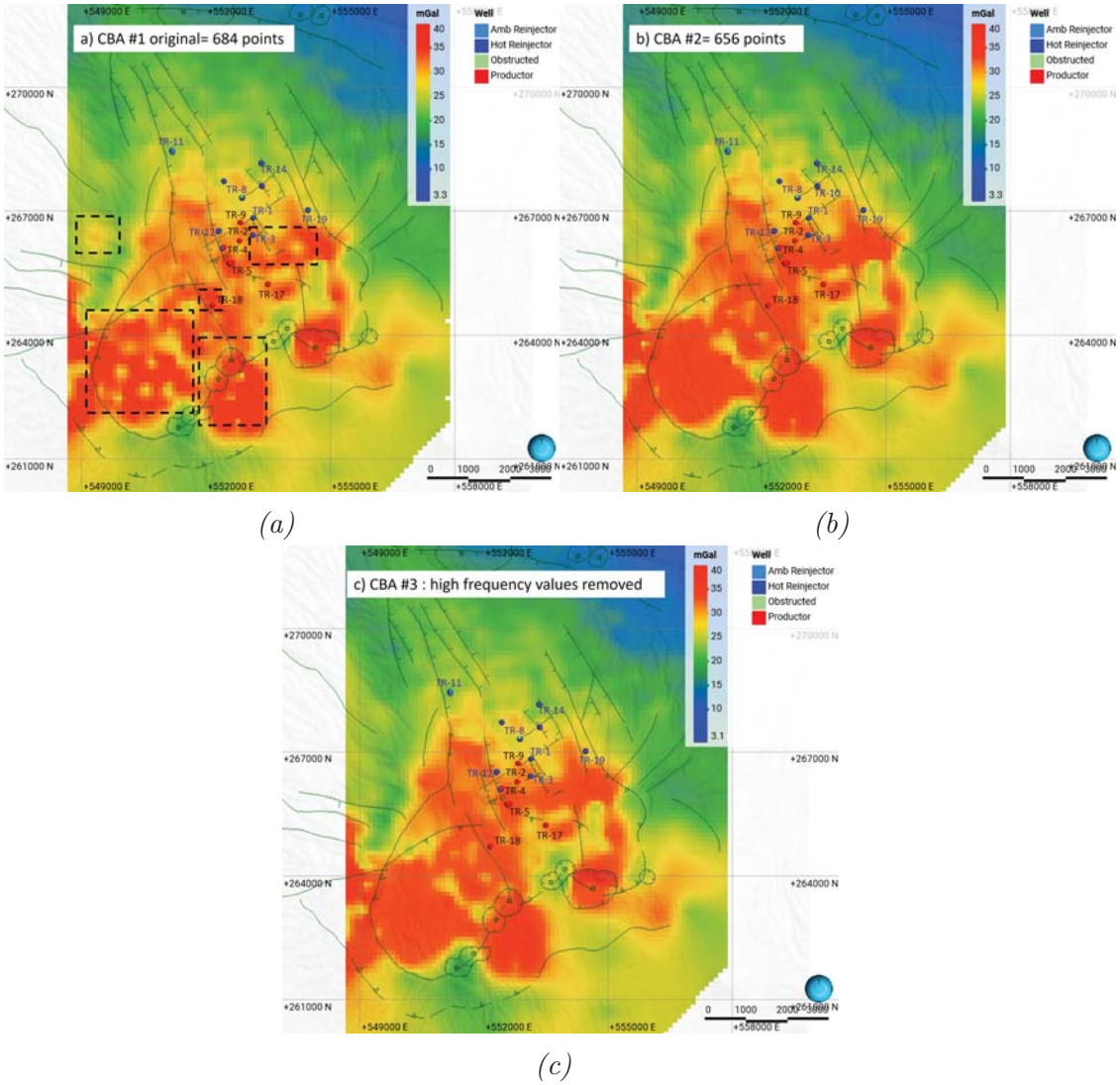


*Figure 3.7. a) Original CBA grid, b) CBA with 28 points removed, and c) new CBA grid with high frequencies removed from the power spectrum. The dashed black boxes indicate the areas of outliers. The green lines represent the structural system of the area.*

The new power spectrum shown in Figure 3.8 is composed of a small range of wavenumbers (reciprocal of wavelength) related to low frequencies (Slope1), which are related to regional anomalies, and a second one of high frequencies (Slope2), which are related to residual anomalies. The regional and residual maps from the new CBA are shown in Figure 3.9 and 3.10, respectively.

Figure 3.9 shows a gravity high anomaly related to a deep source below the production wells in the southern and southwestern part of the geothermal field. In contrast, the residual anomaly shown in Figure 3.10 indicates several gravity high anomalies aligned with geological faults (white dashed lines) and other inferred structures (purple dashed lines).

The horizontal inferred structural lineaments between wells TR-18 and TR-17 could be related to the Blanca Rosa Caldera boundary and between the production and reinjection zone related to The Old Berlin Caldera Boundary. Another interesting aspect of the residual map is the visualization of other lineaments close to well TR-11 and TR-14 that suggest a relation to a third Caldera border, which will be discussed in the following sections.

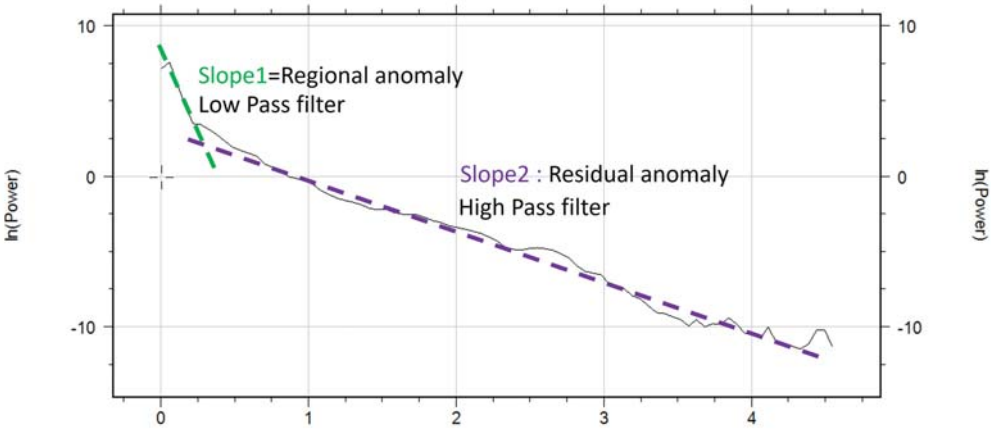


*Figure 3.8. Power Spectrum of Complete Bouguer Anomaly after removal of the high frequencies related to noise. The wavenumber is on the X-axis and the the log(power) in the Y-axis.*

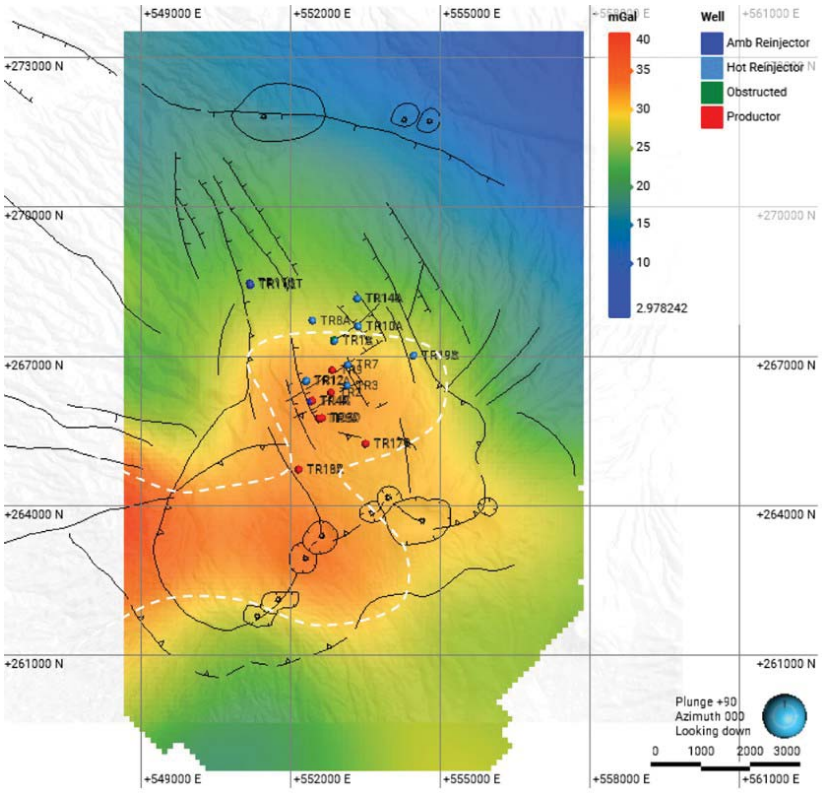


*Figure 3.9. Regional CBA anomaly. The highest gravity values are located in the southern and central part of BGF (dashed white line).*

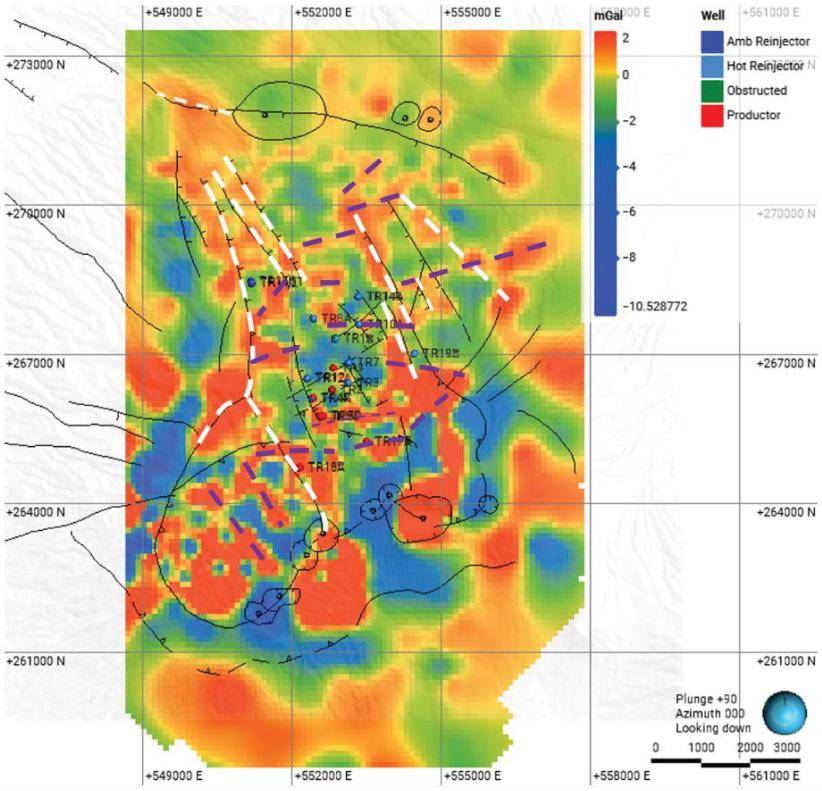


*Figure 3.10. Residual CBA anomaly. The dashed purple lines represent the inferred faults or fissures, and the dashed white line confirmed structures or faults.*

## 3.4 Density inversion model by VOXI earth modeling

The inversion model based on gravity data is a geophysical inversion used to infer the density distribution of the subsurface due to variations in the Earth's gravitational field. The little variations in the gravitational field are caused by different materials with varying densities in the subsurface, which can provide significant insights into subsurface's geological structures.

Geophysical inversion process is non-unique and this is the main problem to solve for geophysicists. For gravity data inversion, different subsurface density distributions can produce similar gravity anomalies. For that reason, additional data, geological-geophysical constraints are often neccessary to improve the inversion results and reduce ambiguity.

In this study, the unconstraint and constraint inversion models are built using VOXI Earth Modelling by Seequent (Seequent, 2023). The software is a cloud-based geophysical inversion tool integrated within the Oasis Montaj platform. VOXI Earth Modelling allows geoscientists to generate 3D models of the subsurface from gravity and magnetic data. The software employs an iterative inversion process to create models that can help understand geological structures, intrusions, and mineral exploration for different environmental studies.

The CBA, regional, and residual anomaly grids have been used as sensor grids. For the inversion process, the general steps to follow are listed below:

- Preparing the gravity data (corrected) and imported into Oasis Monjas as an ASCII format file.
- Apply enhancement filters to the gravity data to highlight or suppress specific features.
- Setting up the inversion, in this step, the geoscientist must define the model space (setting up a mesh) and the sensor grid to use.
- For a constrained inversion model, defining an initial model and its constraints is necessary.
- Analyzing and interpreting the results using 3D view of Oasis Montaj or Leapfrog Energy software.

In this section, the geophysical modelling was implemented in two different ways: (1) entirely unconstrained (i.e., no geological data included), (2) constrained by the 3D resistivity model using homogeneous rock unit densities corresponding to the conductive layer related to the seal cap of the geothermal system, and (3) constrained by the density measured in granite intrusive and altered andesite lavas from well TR-19B and TR-19C. The apparent density inversion models from CBA data are described in the following sections.

### 3.4.1 3D-Unconstrained density model

In this context, an unconstrained model refers to a geophysical inversion process that is performed with no a priori geological or geophysical information about the subsurface. This means the inversion is carried out only mathematically using the gravity data only to retrieve the formation of the subsurface model. In contrast, constrained modeling using additional geological or geophysical information (borehole data, seismic profiles, or known rock properties) are used to guide and inform the inversion process, aiming to reduce the inherent non-uniqueness of the geophysical inversion.

The input in the unconstrained inversion is the Complete Bouguer Anomaly data. A 3D mesh is generated of the area of interest. The mesh divides the subsurface into discrete cells or elements, each with a density value adjusted during the inversion process. The high frequencies related to noise in the CBA data were not considered in the inversion. For this type of inversion (density), the absolute error value equals 0.2591 mGal, corresponding to 5% of the data standard deviation. Figure 3.11 shows the VOXI mesh for the 3D model using the CBA grid.

The mesh of subsurface volume of interest is divided into discrete units. The volume size is the same for the unconstrained and constrained inversion models. The parameters setting for the mesh (see Figure 3.11) is shown below.

- Volume cell size: X=25 m, Y=25 m, and Z=12.5 m
- Maximum depth: 3,000 m.

The VOXI mesh represents the discretized subsurface volume for the inversion of CBA data. The statistics of the observed data (CBA) in the VOXI mesh (cell size: 50 x 50 x 50 m) are estimated after choosing the default linear trend background removal (to avoid

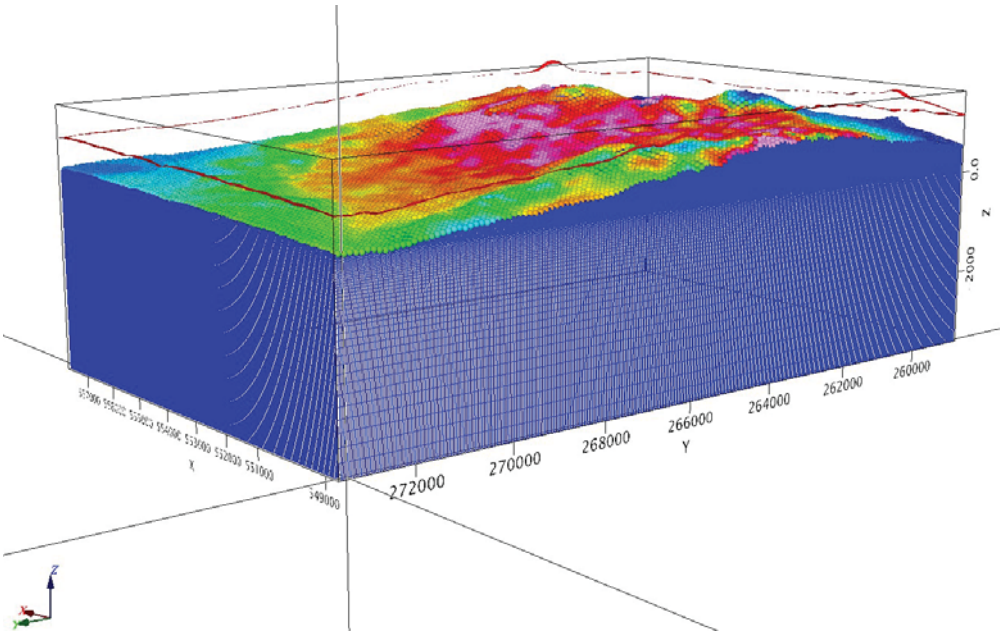


*Figure 3.11. The VOXI model grid for the 3D density inversion model.*

erroneous results and undesirable edge effects). In this case, the default minimum error is 5 % (0.2591 mGal) of the standard deviation of the overall gravity measurements.

- Valid items: 10,756.
- Minimum value: -15.5 +/- 0.3 mGal.
- Maximum value: 27.5 +/- 0.3 mGal.
- Standard deviation: 5.2 +/- 0.3 mGal.
- Absolute error value: 0.3 mGal.

The inversion is run without applying specific constraints that would direct the solution toward a particular geological scenario. The inversion algorithm iteratively adjusts the density values in each cell to minimize the difference between the observed data and the predicted data by the inversion model.

The CBA inversion model is shown in Figure 3.12 and 3.13. Both figures show several bodies of different densities from the surface to the bottom of the conductive layer of 10 $\Omega m$ (at around 500 m b.s.l.), which could be related to the surficial heterogeneity of the geothermal field, besides the structural system of the area. The heterogeneity may be related to the rocks deposited from different eruptions and their non-uniform distribution due to the collapse of Berlin and Blanca Rosa Caldera.

Figure 3.14 shows the density inversion model of the regional gravity anomaly. The statistically calculated values are similar to the CBA model: standard deviation=4.7952 and absolute error value of 0.2398 mGal. The W-E and N-S cross-sections show a strong lateral contrast, which is probably related to the Blanca Rosa Caldera and Berlin Caldera. Furthermore, the bottom of the conductive layer might be related to the bottom of the surficial low-density bodies, which are also related to the calderas' boundary. In the northern part of the field, a third caldera is inferred.

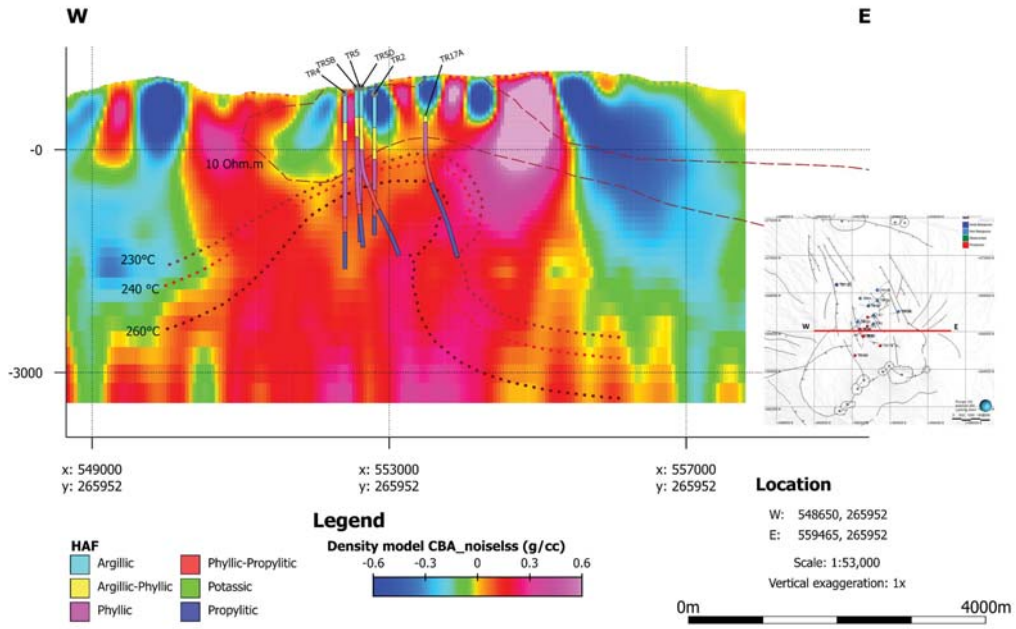


*Figure 3.12. Density cross-section (W-E) of the geophysical inversion of gravity data (CBA). Temperature iso-lines are shown for 230, 240, and 260°C (dotted lines), low-resistivity contour (dashed line in red), and boreholes (their alteration mineralogy is shown in the legend). The inlet map shows the location of the cross-section.*

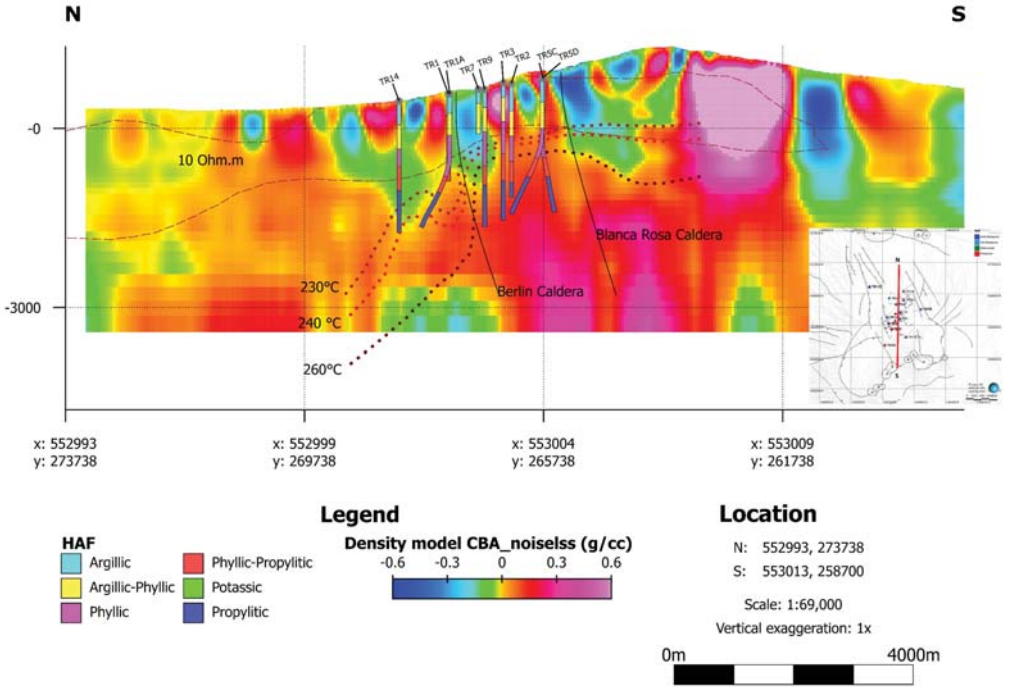


*Figure 3.13. Density cross-section (N-S) of the geophysical inversion of gravity data (CBA). Temperature iso-lines are shown for 230, 240, and 260°C (dotted lines), low-resistivity contour (dashed line in red), and boreholes (their alteration mineralogy is shown in the legend). The inlet map shows the location of the cross-section.*

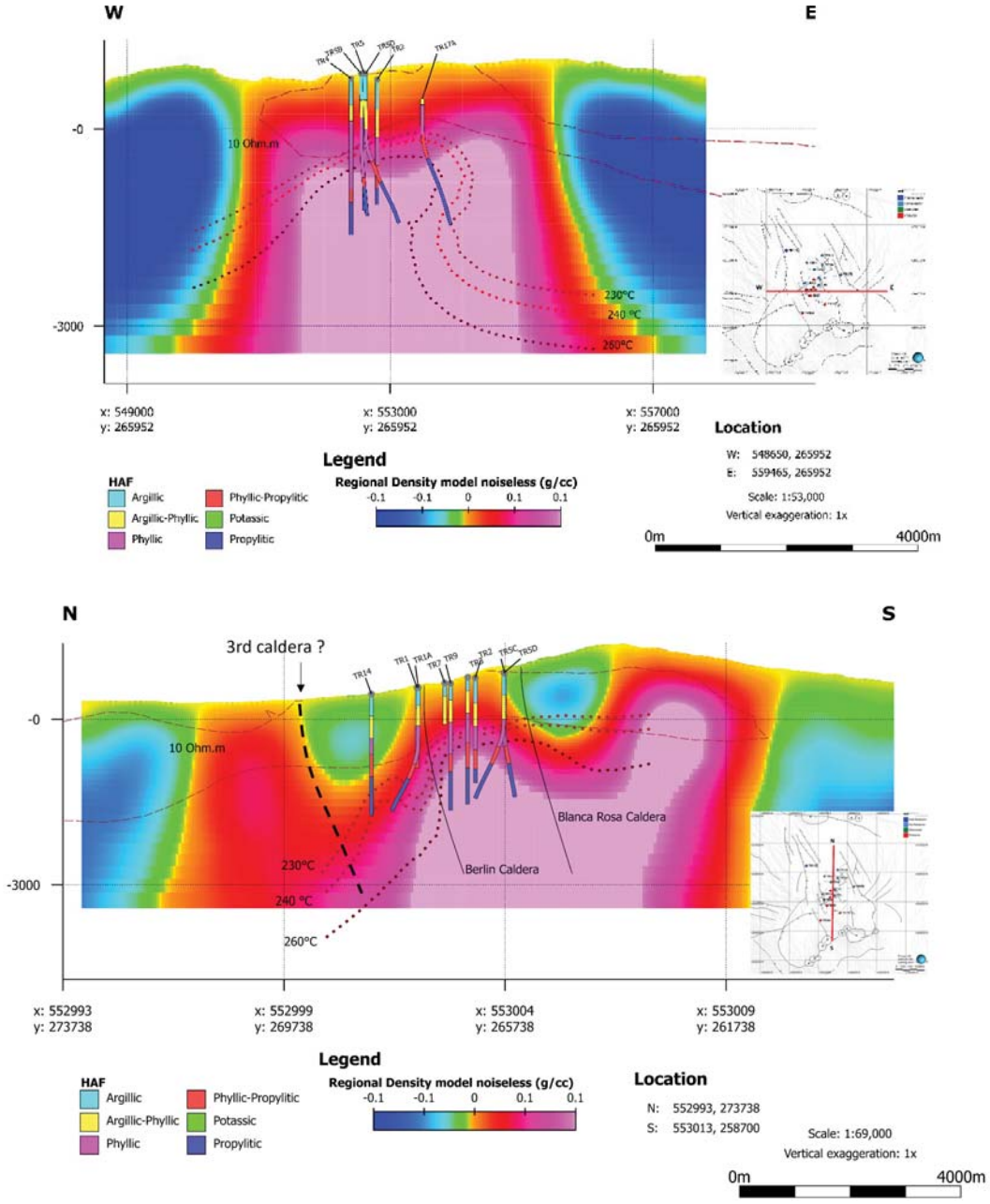


*Figure 3.14. a) Density cross-section (W-E) and b) (N-S). Both of them are from the inversion of the regional gravity data. Temperature iso-lines are shown for 230, 240, and 260°C (dotted lines), low-resistivity contour (dashed contour line), and boreholes (their alteration mineralogy is shown in the legend). The inlet maps show the location of the cross-sections.*

The residual anomaly was inverted to identify the surficial sources (see Figure 3.15). However, the low-resistivity layer related to the seal cap of the geothermal system is not clearly shown as a homogenous layer with similar density values. Below 500 m b.s.l., the anomalies are very sparse, which is normal due to the resolution of this grid for surficial material or rocks and not for deep sources. According to these results, it could be helpful to get a constrained inversion model that helps to determine this vital zone

of the geothermal field. The standard deviation of the residual anomaly is 0.1045 and the absolute error value is 0.1052 mGal.

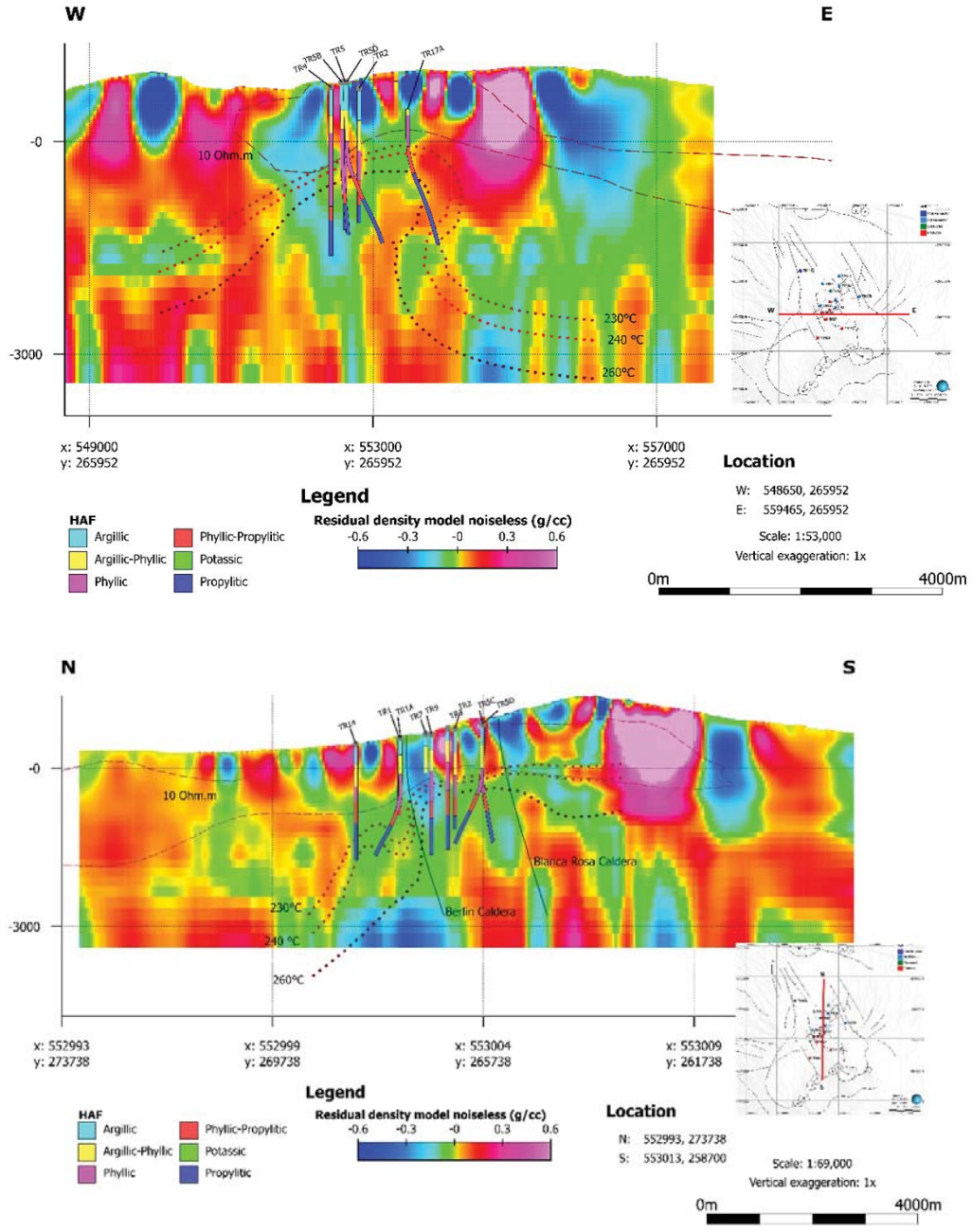


*Figure 3.15. a) Density cross-section (W-E) and b) (N-S). Both of them are from the inversion of the residual gravity data. Temperature iso-lines are shown for 230, 240, and 260°C (dotted lines), low-resistivity contour (dashed contour line), and boreholes (their alteration mineralogy is shown in the legend). The inlet maps show the location of the cross-sections.*

### 3.4.2 3D-Constrained density model

The unconstrained geophysical modelling described in the previous section provides a general guidance about some characteristics of the geothermal system. However, the problem of non-uniqueness always exists (Saltus and Blakely, 2011). In this sense, it is necessary to increase the geological relevance of geophysical models, and incorporate additional information into the density inversion modelling process to guide it toward a more reliable result (Grandis and Dahrin, 2014).

The constrained models for CBA have been constructed using a flexible constraint named "parameter of reference", which guides the inversion to have a specific solution or a priori model. The parameter reference here is related to data from the 10 $\Omega m$ resistivity iso-surface based on 3D inversion, and the bulk density values of granite intrusive and altered andesitic lava rocks from boreholes TR-19B and TR-19C. The methodology for each type of constraint is described below.

**a) Constraint inversion using 10 $\Omega m$ resistivity iso-surface**

The constraint model is based on additional geophysical data from the last 3D MT/TDEM resistivity model shown in section 2.3.1 (see Figure 2.7). The model indicates three main resistivity layers: high-low-high. The low-resistivity of 10 $\Omega m$ is exported from Leapfrog Energy software to be used in the constraint density inversion of gravity data in Oasis Montaj software.

The general workflow shown in Figure 3.16 proposes the general steps to build the constrained density model. The low-resistivity iso-surface is related to the geothermal reservoir's smectite layer or cap-rock (Figure 3.17). The smectite layer is confirmed according to the argillic and argillic-phyllic hydrothermal alteration facies from boreholes, which makes it reliable in constructing the 3D density model to improve the results.

After importing the iso-surface into Oasis Montaj as a Voxel file, the next step is to create a new VOXI model. The VOXI mesh has a dimension of 250 x 250 x 100 m. The mesh is exported as a Voxel file with a value=1. From VOXI, the constraint menu is used to build a new model. The iso-surface and the mesh voxel files are used, and a density value inside the iso-surface is needed to guide the inversion process.

The density of a smectite mineral range from 2.3 to 2.6 $g/cm^3$ at 105°C (Kaufhold et al., 2013). Other studies, e.g., in the exhumed high-temperature paleo-geothermal system on Terre-de-Haut Island, the smectite is between 1.9 and 2.08 $g/cm^3$ at temperatures >180°C (Beauchamps et al., 2019). According to previous findings, this study suggests a density between 1.8 and 2.0 $g/cm^3$ for the cap-rock or conductive layer. The relative density value corresponding to the density value is -0.3. The weight value defined inside the iso-surface is low (0.2) because the density inside the cap rock is not unique.

The next step is to convert from voxel to geodatabase (GDB). In the GDB, replacing the inside surface value of -0.3 with a different value up to 0.1 is necessary. The replacement value has a weight value of 0.20, and the rest of the values around the cap rock layer had a weight value of 0.0001, indicating that the areas outside the iso-surface will not be affected during the inversion. After these modifications, the GDB with the new weight values is converted to a voxel file. The new voxel is used as a parameter weighting, and the mesh voxel is used as a parameter reference model in the constraints setting.

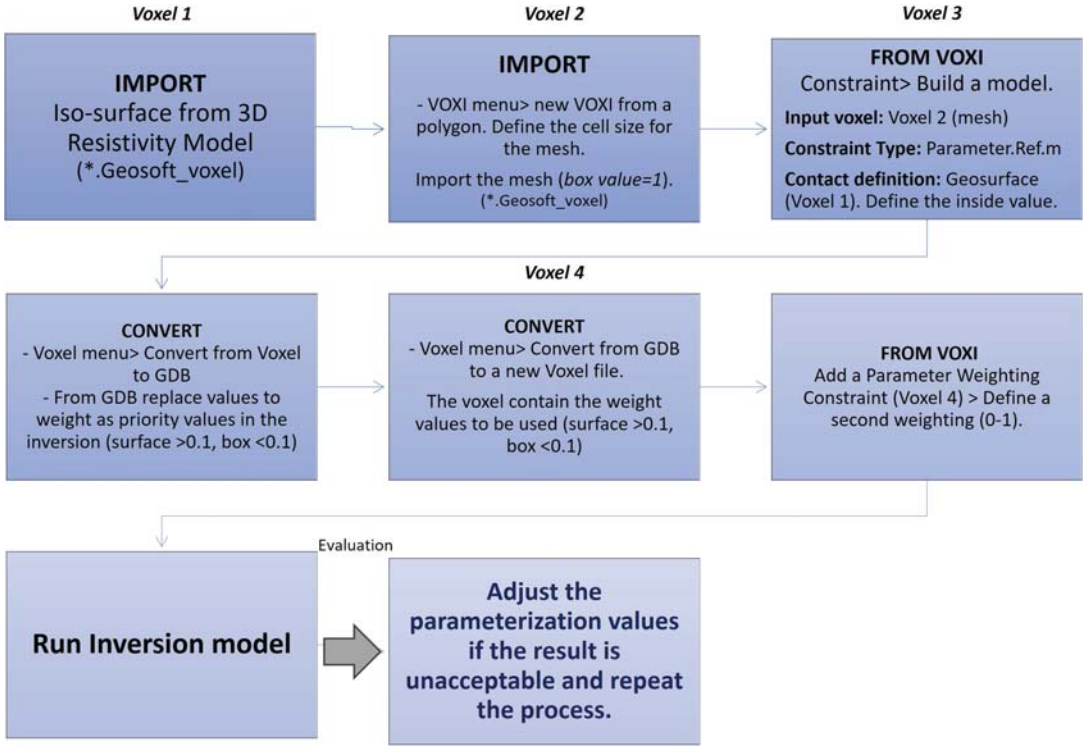


*Figure 3.16. Workflow to construct a 3D resistivity constrained density model with homogeneous rock units in a 3D density inversion. GDB stands for geodatabase.*

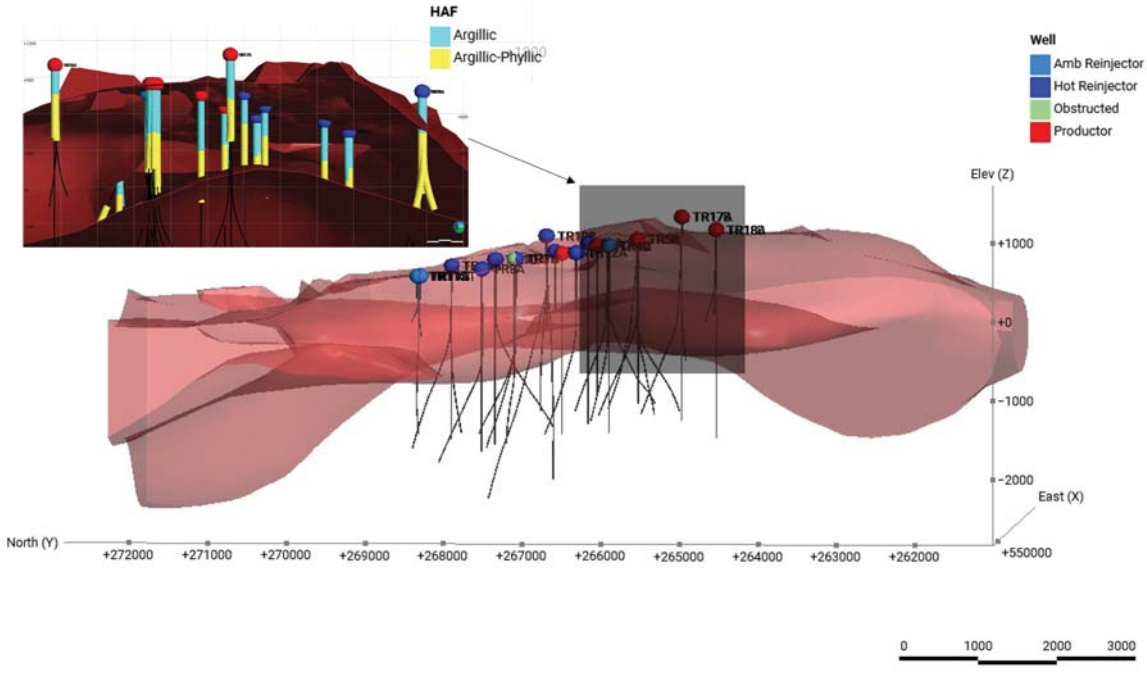


*Figure 3.17. An iso-surface of 10 Ωm resistivity based on 3D resistivity modelling created in Leapfrog Geothermal software. The argillic (light-blue color) and argillic-phyllic (yellow color) hydrothermal alteration facies are shown inside the iso-surface.*

The parametrization to build the constrained model in this study is:

- Input voxel: CBA VOXI mesh.
- Constraint type: Parameter reference model.
- Contact definition: Geosurface (iso-surface of 10 $\Omega m$ resistivity).
- Relative density value inside the surface: -0.3.
- Weight of value inside the surface: 0.2 (range 0-1).
- Weight of value inside the box: 0.0001.
- Weighting value of weights: 0.001 (range 0-1).

Figure 3.18 and 3.19 show the unconstrained and constrained inversion model using the low-resistivity layer of density around 2.0 $g/cm^3$. The relative density values in the unconstrained model varies from -0.6 (1.7 $g/cm^3$) to 0.6 (2.9 $g/cm^3$). The model indicates a density value between 1.75 and 2.06 $g/cm^3$ for the cap-rock and between 2.4 and 2.55 $g/cm^3$ for the geothermal reservoir, respectively. The highest density values are below the volcanic structures, which suggests it could be related to the ascent of hot fluid and deposition of minerals in the area.

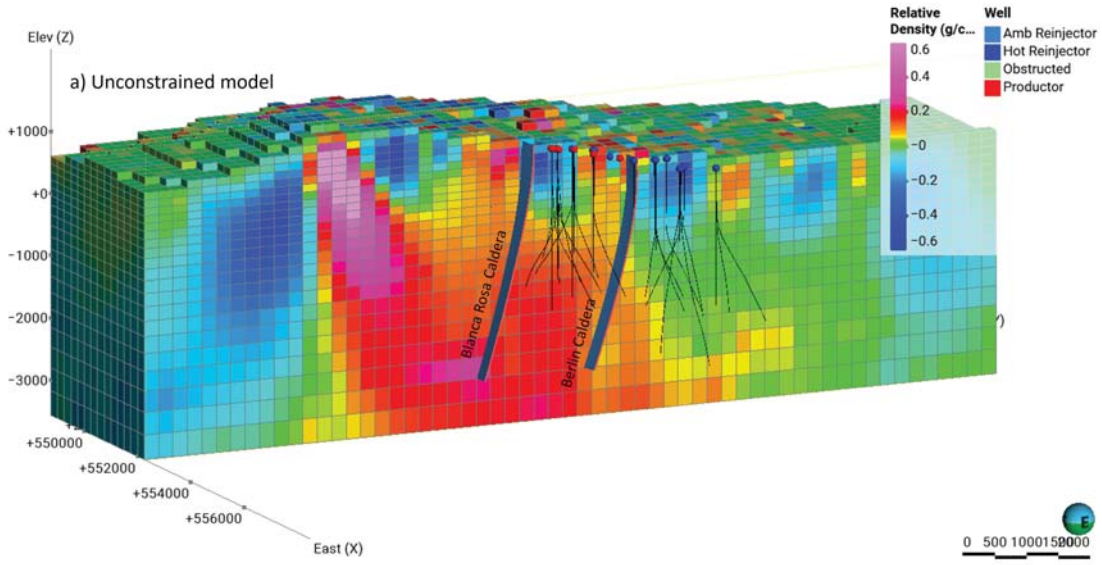


*Figure 3.18. Unconstrained density model of CBA. The geothermal wells and calderas boundaries are shown as blue thin and thick lines, respectively.*

In the constrained inversion model, the 10 $\Omega m$ iso-surface is used because it is not clearly defined in the unconstrained inversion model due to the presence of several gravity contrasts in the surficial materials that are probably related to faults and fractures or the heterogeneity of volcanic deposits in the area; besides, in section 3.4.1 we can observe that the base of the cap rock has a good correlation with the resistivity iso-surface (see Figure 3.13). Figure 3.19 shows some density contrasts related to the Blanca Rosa and Berlin caldera border, besides a third caldera in the northern part of the reinjection area. The possible up-flow in the southern area, related to the Berlin-Tecapa volcanic

zone, is better defined. The cap-rock is better defined, with density values between -0.69 (1.61 $g/cm^3$) and -0.60 (2 $g/cm^3$). The values of relative density are similar and vary from -0.69 (1.61 $g/cm^3$) to 0.62 (2.92 $g/cm^3$).

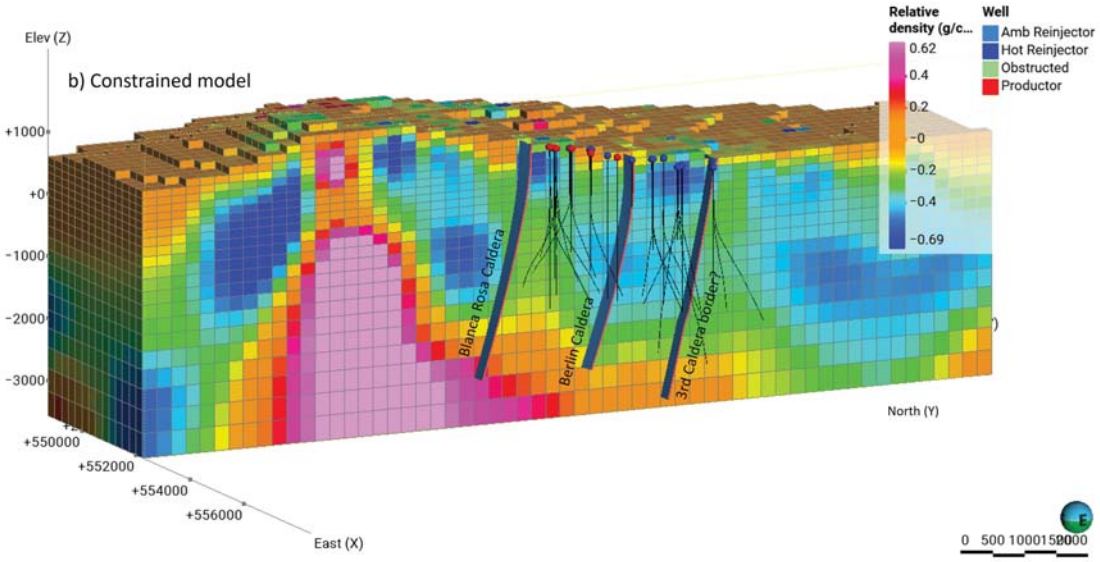


*Figure 3.19. Constrained density model of CBA. The low-resistivity iso-surface of 10 Ωm is used as a parameter reference with a relative density value of -0.3 g/cm$^3$ corresponding to an estimated density value of 2.0 g/cm$^3$. The geothermal wells and calderas boundaries are shown as blue thin and thick lines, respectively.*

### b) Constraint inversion using densities from boreholes

The constrained density inversion model uses the bulk density of granite intrusive rock from five borehole cuttings. The granite intrusive is intercepted by three injection boreholes (TR-19A, TR-19B, and TR-19C) and two production boreholes (TR-5A and TR-17A) at different depths in the geothermal system. However, the bulk density values of granite and altered andesitic lava rocks have only been identified from cutting samples in boreholes TR-19B and TR-19C (see Figure 3.20) through petrophysical analysis (Torio-Henriquez, 2007). This information makes it ideal for applying the constraint inversion model to CBA data to estimate the variations due to deep sources and minimize the ambiguity of the density inversion model.

Figure 3.20 shows the projection of well TR-19B and TR-19C and the general lithological distribution based on geological cuttings used to measure the bulk density of the granite intrusive. Furthermore, Table 3.1 shows the depth ranges where the core samples were taken and the inferred density of granite intrusive in boreholes TR-5A, TR-17A and TR-19A.

In this area, two core samples (CS1 and CS2) from borehole TR-19B were used for petrophysical analysis, identifying the granite's bulk density, which varies between 2.56 and 2.64 g/$cm^3$ (Torio-Henriquez, 2007). The exact depth for each density of granite is not revealed in the technical report, however, to simplify the model, for borehole TR-19B the average density of granite and altered andesitic lava rock is used. The average density of the granite intrusive is 2.60 g/$cm^3$ and for the altered andesitic lava a

density of 2.64 g/$cm^3$. The analysis of two fragments of the core samples from borehole TR-19C indicates the granite's bulk density of 2.65 g/$cm^3$, and an altered andesitic lava's bulk density of 2.75 g/$cm^3$ (Torio-Henriquez, 2007). For well TR-5A, TR-17A and TR-19A, the bulk density of the granite nearest to them, is used (samples from TR-19B and TR-19C).

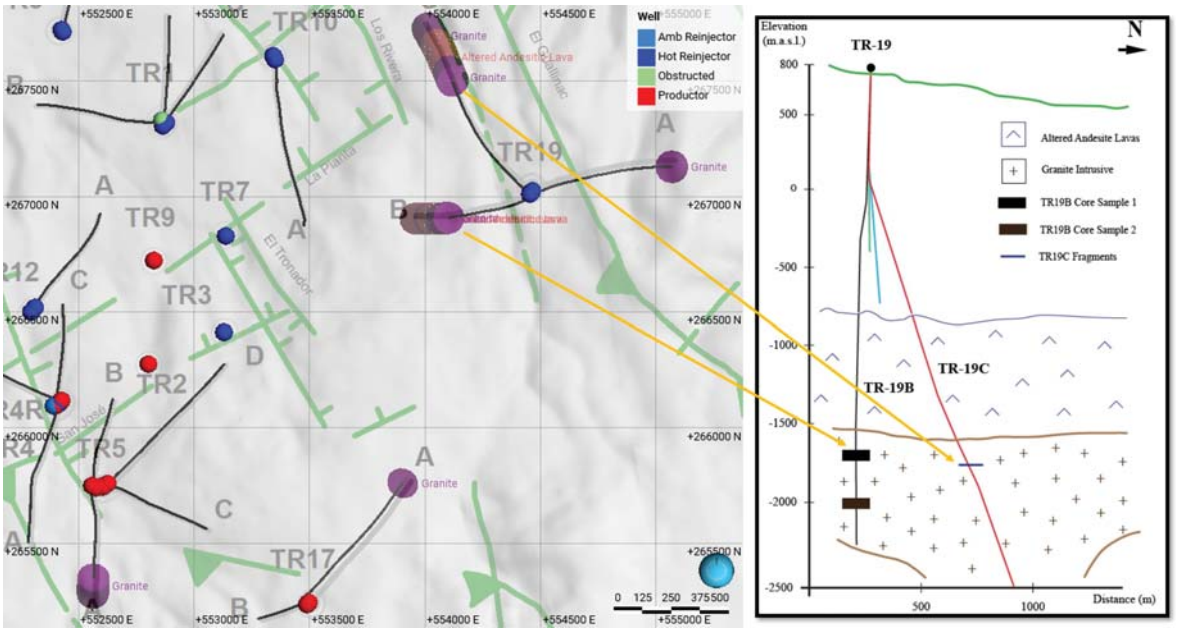


*Figure 3.20. Projection of boreholes TR-19B and TR19C, general lithological distributions, and elevations of core samples and fragments for petrophysical analysis. Image modified from Aparicio, 2023.*

*Table 3.1. Lithology distribution at depth of borehole cutting samples (Torio-Henriquez, 2007)*

| **Borehole** | **Depth (m)** | **Description** | **Bulk density (g/$cm^3$)** |
|---|---|---|---|
| TR-19A | 2330-2362 | Granite intrusive | 2.65 (ref.TR-19C) |
| TR-19B | 2350-2515 | Granite | 2.60 (avg. CS1 and CS2) |
| TR-19B | 2515-2695 | Altered andesitic lava | 2.64 (CS2) |
| TR-19B | 2695-2715 | Granite | 2.60 (average CS1 and CS2) |
| TR-19B | 2715-2720 | Altered andesitic lava | 2.64 (CS2) |
| TR-19B | 2720-2780 | Granite | 2.60 (average CS1 and CS2) |
| TR-19B | 2780-3125 | Altered andesitic lava | 2.64 (CS2) |
| TR-19C | 2630-2770 | Granite | 2.65 (Fragment 2) |
| TR-19C | 2770-3170 | Altered andesitic lava | 2.75 (Fragment 3) |
| TR-19C | 3170-3545 | Granite | 2.65 (Fragment 2) |
| TR-5A | 1960-2120 | Granite intrusive | 2.60 (Ref.TR-19B) |
| TR-17A | 2628-2629 | Granite intrusive | 2.60 (Ref.TR-19B) |

The workflow for this type of constraint changes slightly from the first constrained model described in Figure 3.16. The general steps to construct the constrained inversion model using drillhole property information are described in Figure 3.21.

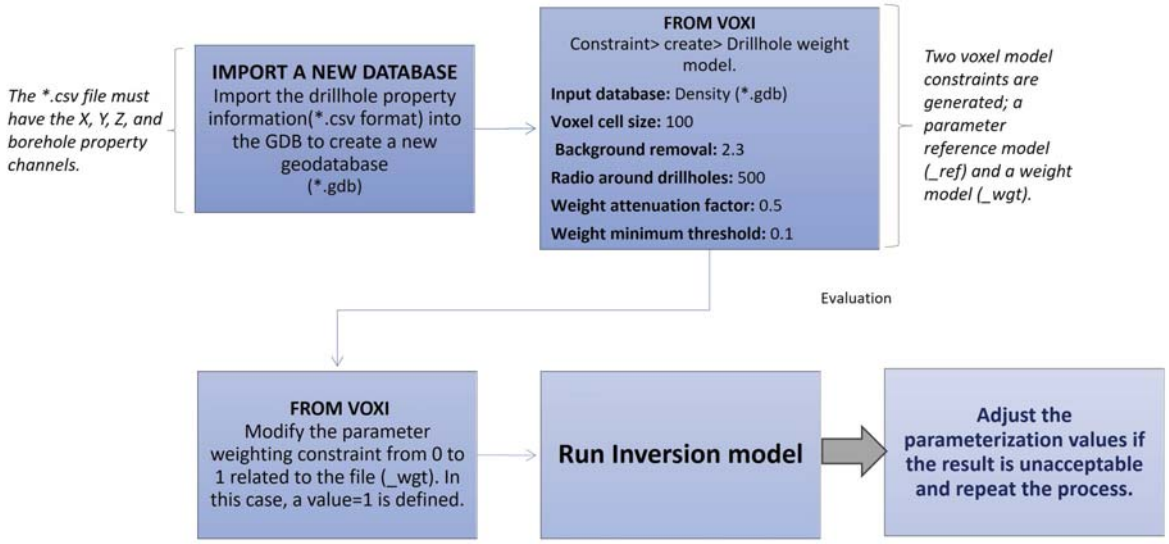


*Figure 3.21. Workflow to build a constrained inversion model using information from geothermal boreholes. For this study, the bulk density from granite intrusive and altered andesite lava rocks are used*

The parametrization for the constrained inversion model, is very sensitive, and for that reason it is necessary to verify the best values to improve the apparent density inversion model. The data along the drillholes are linearly interpolated at the smallest voxel cell size. Then a set of two voxel model constraints are generated.

For this study, the density data are gridded using the 3D Kriging method to produce the parameter reference model. The density data are gridded using a voxel cell size of 100 m. The background removal parameter is the mean of the property to remove (this is optional). This is highly recommended because, a real value of density is considered in the inversion, while VOXI models use the contrast in the property. After several routines, the absolute density of 2.3 $g/cm^3$ is removed. The radius around drillhole parameter is related to the influence of the density of rocks extended a reasonable distance from the borehole. By default, the constraint is extended to a distance of 4 cells, however, for this study, a value of 500 is used. The weight attenuation factor (1), is the weight assigned to the reference model that decreases exponentially away from the drill path, in other words, this is how quickly the weight is attenuated in the normal direction to the borehole trace until it reaches the minimum threshold. Finally, the last parameter to set up is the weight minimum threshold (0.01), which is the value to which the weight attenuates (Seequent, 2023).

The equation applied to produce the weight voxel model is (Seequent, 2023):

$$\boldsymbol{V}_w = (e^{-pd} * (0.9 - Min)) + Min \tag{5}$$

Where:

- $V_w$: weight voxel
- p: power =1

- d: distance from the drill trace
- Min: minimum threshold = 0.01

Figure 3.22 shows the constrained inversion model using the bulk density of the granite and altered andesite lava rocks from boreholes described in Table 3.1. Figure 3.23 shows the zoom-in of the lithology of boreholes TR-17A, TR-17B and TR-17C and their comparison with the constrained inversion model. The resulting constrained inversion model seems to be more confident, especially to analyse the geothermal system that is discussed in Chapter 4.

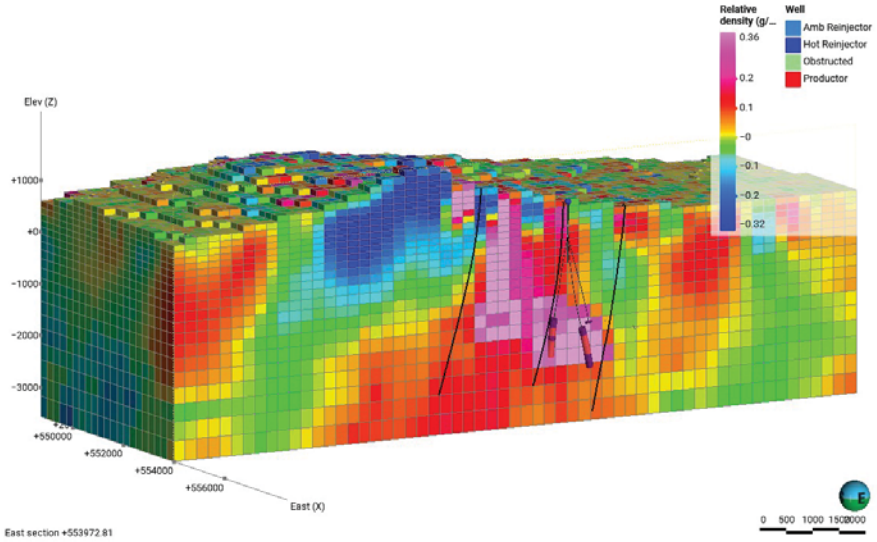


*Figure 3.22. Constrained inversion model using the bulk density values of the granite intrusive and altered andesitic lava from boreholes TR-19B and TR-19C by petrophysical analysis. The density values for boreholes TR-5A, TR-17A and TR-19A are assumed using similar values from the nearest borehole cutting. The geothermal wells and the calderas boundaries are shown as black thin and thick lines, respectively.*

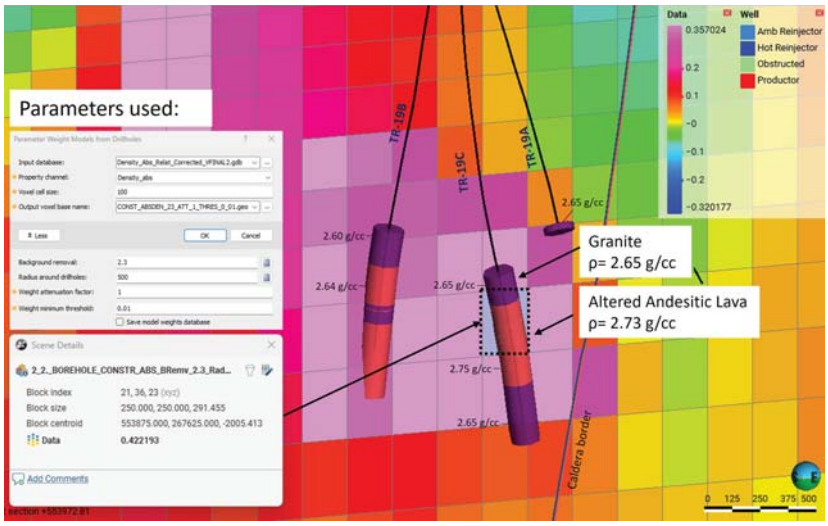


*Figure 3.23. Evaluation and comparison between the constrained inversion model and the bulk density values from core samples in borehole TR-19B and TR-19C*

## 3.5 Horizontal gradient analysis

The previous section presented a density model of the geothermal system based on gravity data, which was conducted using 3D inversion. In this section, the modeling result is integrated with the result of derivative analysis (horizontal gradient) through the Oasis Montaj software with the aim of finding new characteristics in BGF.

Before applying the horizontal gradient, the CBA must be separated into a regional and residual anomaly. The regional anomaly is calculated by using the Butterworth filter for low frequencies. The wavelengths to analyze are 1000, 2000, 3000, and 4000 m. Figure 3.24 shows the results for each wavelength, indicating the strong influence of deep sources in the geothermal area. The regional anomalies for 1000, 2000, and 3000 m are quite similar, however for 4000 m, which is related to the deepest anomaly it is more remarkable in the area.

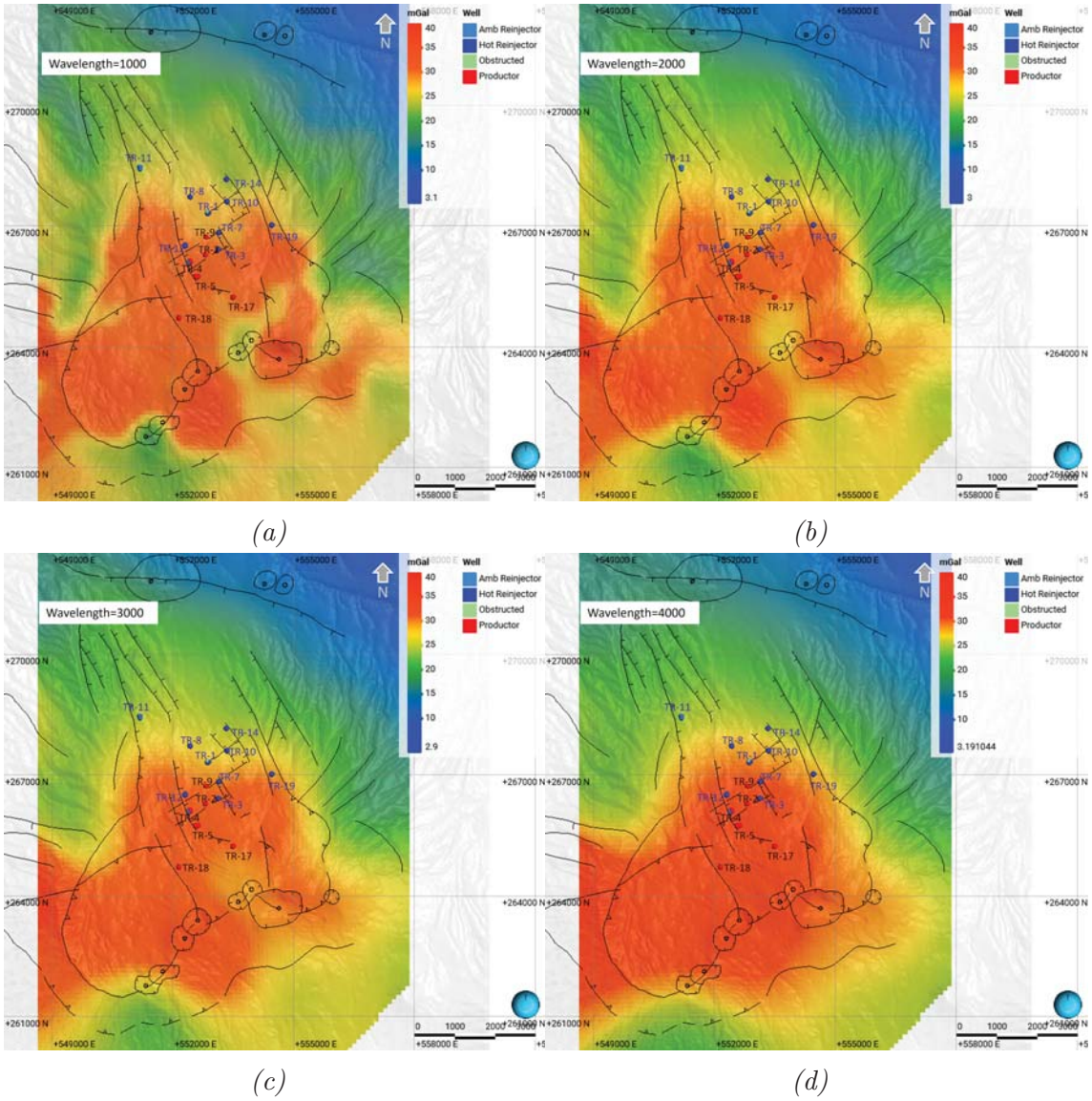


*Figure 3.24. Regional maps for a) 1000, b) 2000, c) 3000, and d) 4000 wavelength [m]. The filter applied is the Low-Pass Butterworth filter*

The Butterworth filter is excellent for applying straightforward "Low-Pass" filters to gravity data because the degree of filter could be fixed while the central wavenumber can be easily controlled. If the results are distorted, the degree can be reduced until it is acceptable (Seequent, 2023). The wavelength cutoff is in ground units (m), degree of filter =8 (default) and filter type=low pass.

The regional anomaly for each wavelength is analyzed using a horizontal derivative analysis which is abbreviated as the "HDG" method by using the Equation (6). This method aims to identify the gravity contrasts due to different sources at different depths below the surface. The method is useful to identify and characterize faults in a geothermal system (Rosid & Sibarani, 2021).

$$HDG = \sqrt{(\frac{dg}{dx})^2 + (\frac{dg}{dy})^2} \tag{6}$$

Where:

- $HDG$: Horizontal Derivative Gradient.
- $dg/dx$: Horizontal gradient in the X-direction=0.
- $dg/dy$: Horizontal gradient in the Y-direction=90.

Figures 3.25, 3.26, and 3.27 show the results of the horizontal gradient of the regional anomaly with cutoff wavelength= 1000, 2000 and 3000 m, respectively. The high horizontal gradient indicates a strong relationship between some structures, e.g., the Blanca Rosa caldera, the old Berlin caldera, the W and E limits of the geothermal system, and the volcanic structures in the southern part of the field. The results suggest a low horizontal gradient in the production zone for wavelengths of 3000 and 2000 m.

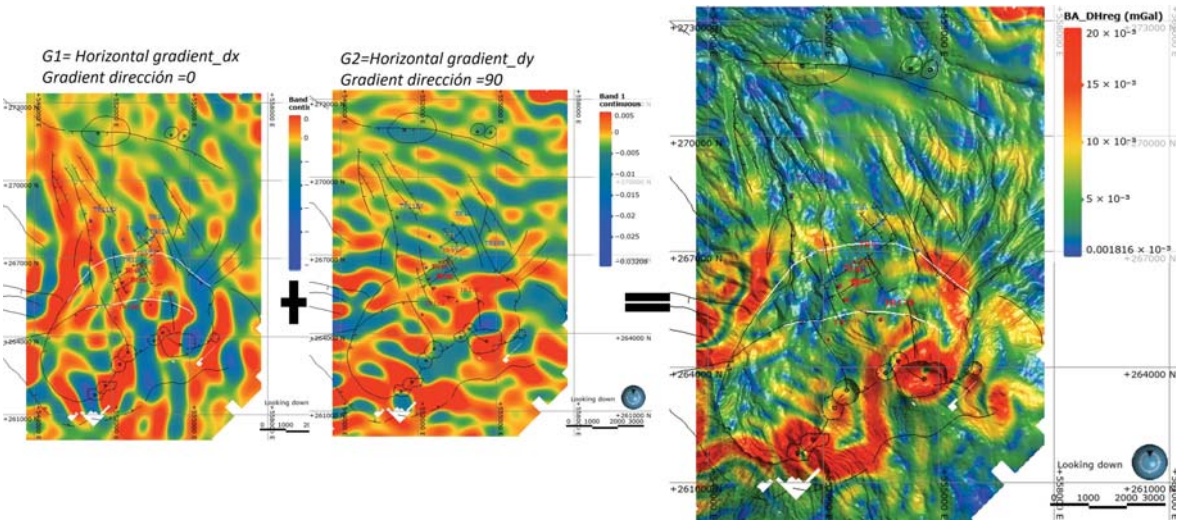


*Figure 3.25. HDF of the regional anomaly with a cutoff wavelength= 1000 m.*

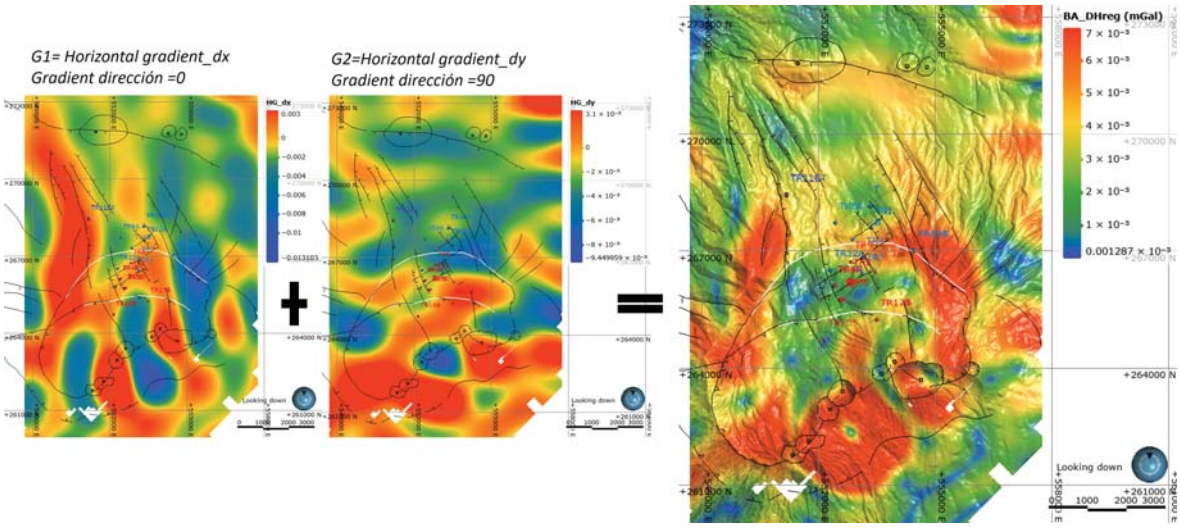


*Figure 3.26. HDF of the regional anomaly with a cutoff wavelength= 2000 m.*

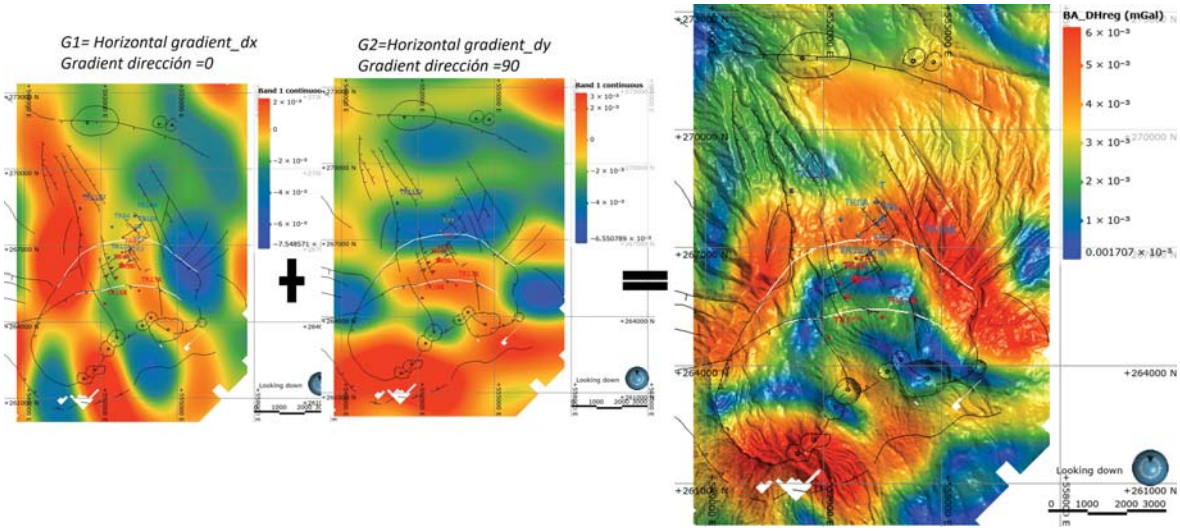


*Figure 3.27. HDF of the regional anomaly with a cutoff wavelength= 3000 m.*

## 3.6 Conclusions

Geophysical inversion has the problem of non-uniqueness, which means that a model result generated by an inversion modeling algorithm is one of many that can explain the measured data. Mathematically the results can be acceptable, but at the same time be incorrect geologically. Due to this reason, it is necessary to include additional information related to the geology of the geothermal area, and test different inversion processes to improve the results. In this study, the constrained models improved the ambiguity of an unconstrained density inversion model. The first constrained model using a homogeneous density layer linked to the cap-rock reflects fewer heterogeneities due to the restrictions of density inside the iso-surface ($<2.0\ g/cm^3$); however, the high contrast due to the presence of caldera borders (Blanca Rosa caldera, Berlin Caldera and an inferred third caldera) always appear, which indicates a strong source in the inversion model, as well as, the high anomaly below the Berlin-Tecapa volcanic structures. The second constrained model reflects a good response to the bulk density

of granite and altered andesitic lava rocks. This is observed with the comparison of density between the inversion model and the measured density from the cutting samples from boreholes TR-19B and TR-19C (see Figure 3.22)

Regional and residual anomaly results show a good correlation between high-gravity anomaly and the presence of several structures in the geothermal area. 3D inversion of gravity data shows low-density contrast which can be seen from topographic level to 500 m b.s.l. related to the low-resistivity layer (smectite layer), while high-density contrast can be seen below 500 m b.s.l. The contrast of low-high density is associated with the presence of Blanca Rosa caldera and old Berlin caldera, faults, and a third caldera boundary in the northern of the field (see Figure 3.14 and 3.18). The horizontal gradient of gravity data results confirms the presence of those calderas' boundaries at a similar location (see Figure 3.27). In general, the low-density anomalies between the faults are interpreted as a weak zone which can be interpreted as a graben or horst within the geothermal system.

# 4 New contributions to the conceptual model of BGF

The conceptual model of geothermal systems is used to describe and illustrate the geological conditions and delineation of important processes that occur in a geothermal field (Ponggohong et al., 2020). In this study, some relevant features are described in the construction of a static conceptual model of a geothermal system, which means, time-dependent data is not included (this is for a dynamic model), such as production history data. A static conceptual model needs to propose some main features of the geothermal system, e.g., the heat source, flow channels, flow patterns, and fluid chemical conditions of the reservoir, recharge zone and temperature (Hersir et al., 2022). Usually, it is visualized as 2D cross sections or as 3D models through the various available visualization softwares; in any case, it is necessary to consider some essential elements, that make a comprehensive conceptual model of a geothermal system (Axelsson, 2013):

- Provide an estimate of the size of the system, more specifically information on areal extent, thickness and depth range as well as external boundaries (vertical).
- Explain the nature of the heat source(s) of the system.
- Include information on the location and strength of the up-flow/recharge zones, including the likely origin of the fluid.
- Define the general flow pattern of the system, both in the natural state and changes in the pattern induced by production.
- Define the temperature and pressure conditions in the system (i.e., initial thermodynamic conditions through formation temperature and pressure models).
- Indicate locations of two-phase zones, as well as steam-dominated zones.
- Describe locations of main permeable flow structures (faults, fractures, horizontal layers, etc.).
- Indicate the location of internal boundaries (vertical and/or horizontal) such as flow barriers.
- Delineate the cap-rock of the system (horizontal or semi-horizontal boundaries).
- Describe the division of the system into subsystems, or separate reservoirs, if they exist.

The last version of the conceptual model of BGF was constructed in 2019 and has been updated over the years thanks to the integration of more information from new boreholes and geoscientific studies. In this study, an update and a 3D view of the static conceptual model is focused on using the results of the 3D density model, the 3D

seismic tomography of Vp, Vs velocity, and the Vp/Vs ratio, the 3D temperature model, and the structural system.

The results and interpretations are described in the next sections.

## 4.1 Up-flow zone

In the conceptual model from 2019, it is described how the isotope analysis suggested that deep fluids ascent towards boreholes TR-18 and TR-17 (LAGEO, 2019). The minimum temperature of the deep fluids measured in the southern part of BGF is around 305°C. The maximum temperature evaluated by geothermometers of gas in fumarole is estimated to be around 350°C. Besides, SiO2 geo-temperatures of fluids from production wells and temperature loggings indicate a second up-flow of deep fluids towards the area of boreholes TR-4 and TR-5 (LAGEO, 2019).

The proposed up-flow zones are furthermore supported by the 3D unconstrained and constrained density inversion, which reveals density anomalies related to the ascent of deep hot fluids. Figure 4.1 shows an anomaly of high density (2.5-2.6 g/$cm^3$) near boreholes TR-4 and TR-5, indicating the up-flow zone, as well as, the isotherms of 270 and 280°C and temperatures measured in The Tronadorcito (96.9°C) and Tronador (98.9°C) fumaroles in the same area, which evidence the ascent of hot fluids.

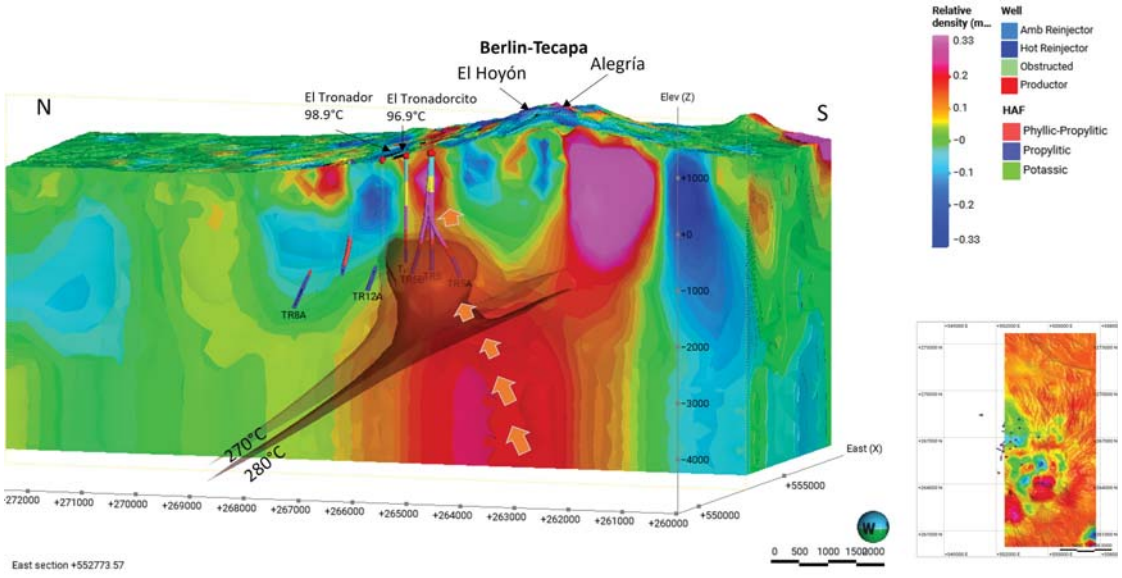


*Figure 4.1. 3D unconstrained density model and the proposed up-flow zone toward boreholes TR-4 and TR-5. On the surface, El Tronador and Tronadorcito fumaroles evidence the ascent of hot fluids in the area.*

The second proposed up-flow zone toward boreholes TR-17 and TR-18 is shown in Figure 4.2. According to the 3D unconstrained density model, the same high density anomaly is divided into two flow paths in the area; one towards platform TR-17, which has three production wells crossing the Blanca Rosa border, and a second one toward platform TR-18. Finally, boreholes TR-18A and TR-18B were directionally drilled without crossing the caldera boundary, which could be related to intercepted the steam

cap. The deep hot fluid follows the caldera border, however, the highest temperature is in the northern part of the caldera.

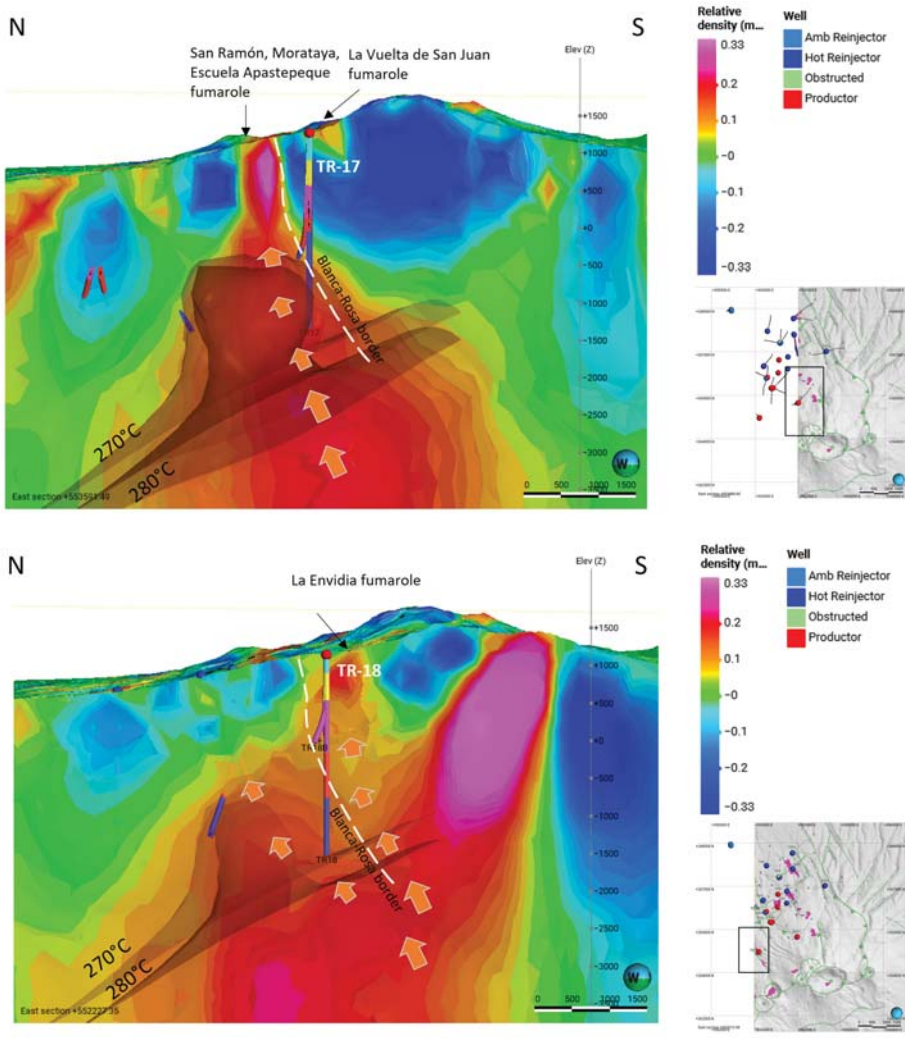


*Figure 4.2. 3D unconstrained density model and the up-flow zone toward boreholes TR-17 and TR-18. On the surface, San Ramon, Morataya, Escuela Apastapeque, La vuelta de San Juan, and La Envidia fumaroles evidence the ascent of hot fluids in the area.*

Gravity measurements reveal density anomalies; however, a joint interpretation of results from seismic tomography and gravity measurements could enhance the modeling results. Seismic wave velocities, both Vp and Vs, reflect fundamentally seismic properties. Seismic velocities generally increase with depth, although they vary with changes due to internal and external conditions like, e.g., confining stress, temperature, pore pressure, fluid saturation, porosity, and crack density (Hersir et al., 2022).

In 2021, LaGeo provided micro-earthquake (MEQ) seismic data sets from two time periods, 1996-2005 and 2014-2021 to perform 3D tomographic velocity modeling by CGG Geoscience, Multiphysics Company (CGG, 2021). For each period, a specific seismic network was employed (see Figure 4.3 (e-f)); in 1996-2005, 15 receivers and during 2014-2021, 7 receivers were collecting data. The map of earthquakes distribution used to build de seismic tomography by the CGG company is shown in Figure 4.3 (a-b).

Figure 4.3 (c-d) shows the histograms as a function of time, number of events, P-wave and S-wave picks, and number of receivers. This illustrates that the network is not permanent in BGF.

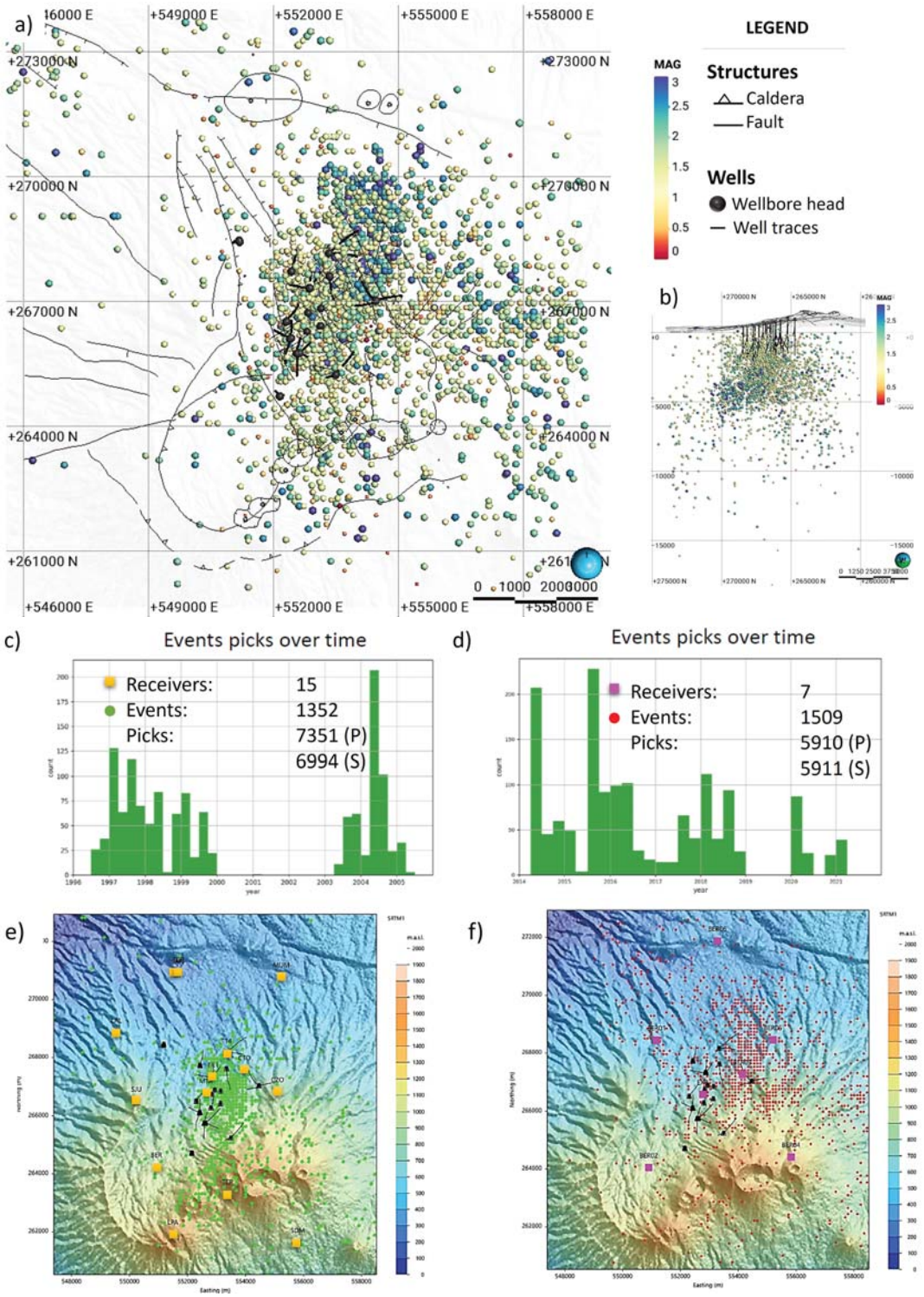


*Figure 4.3. (a) Map of BGF and earthquake distribution recorded in 1997-2021. (b) N-S cross-section of the event distribution and trajectories of all wells. (c-d) Histograms illustrating the number of events for each period, P-wave and S-wave picks, and number of receivers. (e-f) Receivers location and events for each period (CGG, 2021).*

After a quality analysis, the seismic data were inverted to estimate the subsurface velocity structure of the area. The output is a 3D view velocity model of P and S wave velocities and the Vp/Vs ratio from both data sets. The Vp/Vs ratio refers to the ratio of P wave velocity (Vp) to S wave velocity (Vs) within the subsurface of the Earth. The resulting model is used to conclude about the physical and geothermal properties of the geothermal field (CGG, 2021).

In general, a high Vp/Vs ratio is found when the rock temperature approaches its melting point, the shear strength reduces, and S-waves are attenuated far more than the P-waves. A high Vp/Vs ratio indicates high temperature, but very little if any, partial melt as we still record S-waves (Amoroso et al., 2022). Besides, low Vp/Vs velocity anomalies are related with high temperatures zones, steam saturated formations and hydrothermally altered zones (Pavez et al., 2016). Figure 4.4 shows areas of similar Vp/Vs ratio values, that are related to the active conduits of steam saturated formations. At 2000 and 2500 m b.s.l. the same anomaly of around 1.65-1.70 is observed, which is ascending and extending laterally to 1000 and 1500 m b.s.l. of the main production area.

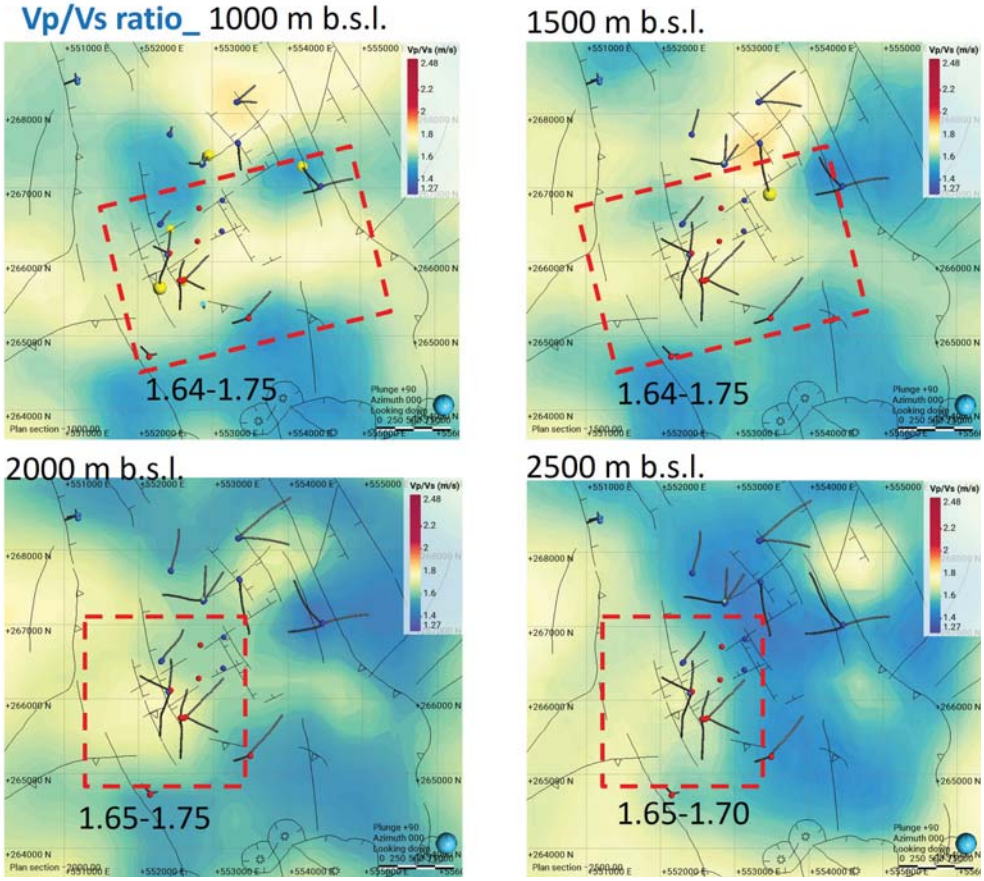


*Figure 4.4. A 3D seismic tomography velocity model of BGF. Selected maps at 1000, 1500, 2000 and 2500 m b.s.l. show the Vp/Vs ratio. The areas of similar range of values are closed in the dashed red square. Model is taken from (CGG, 2021)*

Complementary, the upflow is shown on three slices of the Vp/Vs seismic tomography in the same areas where the upflow is identified in the 3D density model (see Figure

4.5, 4.6 and 4.7) . The deep hot fluid travels from hot solid rocks that heat up the infiltrated fluid and ascents towards boreholes TR-4 and TR-5 (see Figure 4.5). A clear discontinuity in the low Vp/Vs anomaly is identified, which suggests an indication of the flow path of hot fluids. Similar results are seen in areas close to boreholes TR-17 and TR-18 (see Figure 4.6 and 4.7).

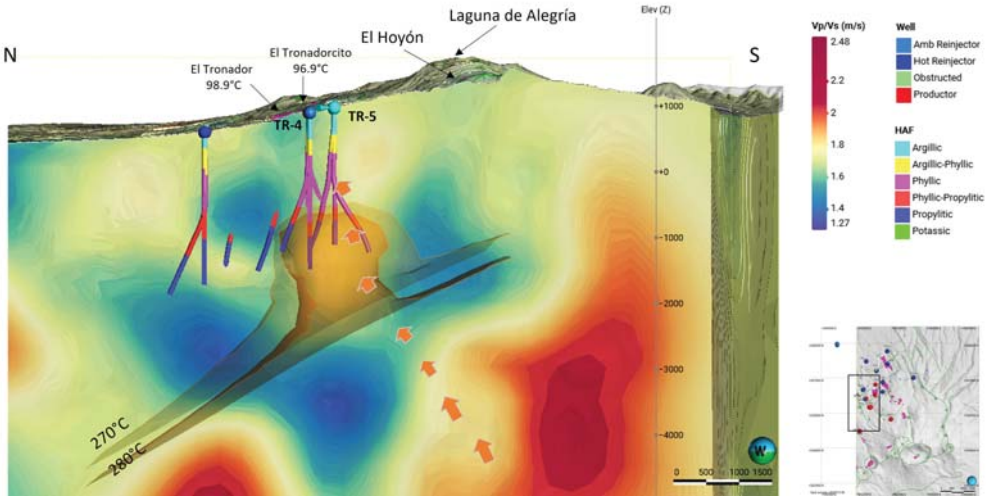


*Figure 4.5. Seismic tomography of the Vp/Vs ratio (CGG, 2021). The cross section runs from north to south near borehole TR-4 and TR-5. The arrows indicate the upflow zone. The 270 and 280°C isosurfaces are used for comparison with the seismic tomography. The hydrothermal alteration facies in borehole are shown as well. The inset map shows the location of the cross-section.*

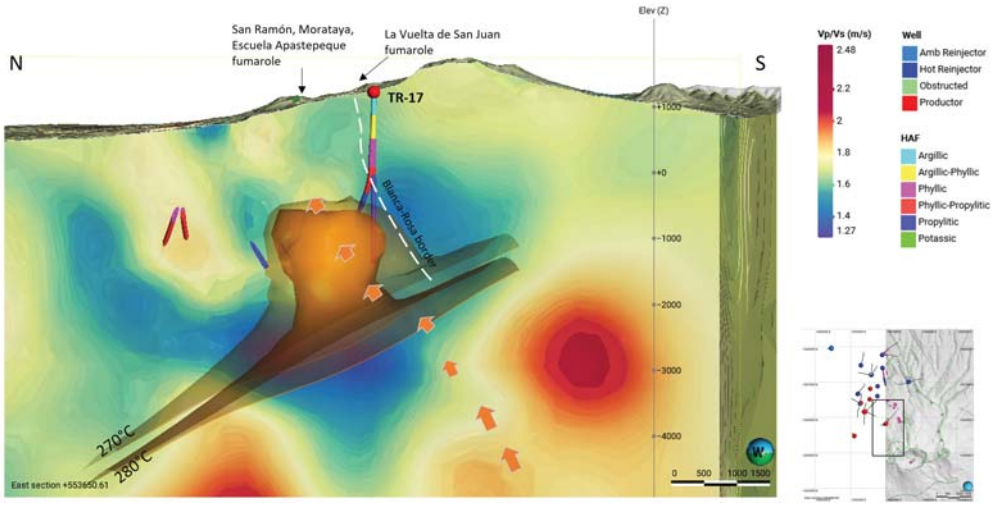


*Figure 4.6. Seismic tomography of the Vp/Vs ratio (CGG, 2021). The cross section runs from north to south near borehole TR-17. The arrows indicate the upflow zone. The 270 and 280°C isosurfaces are used for comparison with the seismic tomography. The hydrothermal alteration facies in borehole are shown as well. The inset map shows the location of the cross-section.*

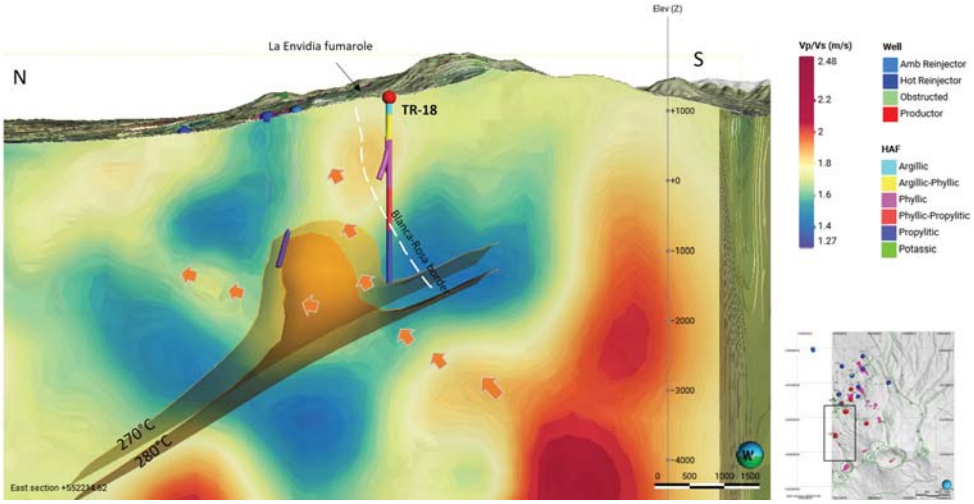


*Figure 4.7. Seismic tomography of the Vp/Vs ratio (CGG, 2021). The cross section runs from north to south near borehole TR-18. The arrows indicate the upflow zone. The 270 and 280°C isosurfaces are used for comparison with the seismic tomography. The hydrothermal alteration facies in borehole are shown as well. The inset map shows the location of the cross-section.*

## 4.2 Granite intrusions

In this section, the 3D constrained inversion density model based on gravity data (see Chapter 3.4.2) and the Vp velocity model (CGG, 2021) are used to confirm and characterize the granite rock identified in boreholes TR-5A, TR-17A, TR-19A, TR-19B and TR-19C.

The 3D density model, was built using the bulk density of granite and altered andesite lava rocks from boreholes TR-19B and TR-19C. The borehole data are used to intepretate the granite intrusive rock to reduce the ambiguity of the inversion model (see Figure 3.23). The model indicates a high-density anomaly at 1000 m b.s.l. related to the top of the granite body with density values around 2.5-2.67 $g/cm^3$. Solid rock intrusions in volcanic geothermal systems appear as high-density anomalies, which are detected as high P-wave velocity anomalies (Hersir et al., 2022); however, in this study, the areas near to the granite intrusions are detected as low velocity anomaly, which could be due to fluid injection in the subsurface (see Figure 4.8). The Vp velocity at 1000 and 1500 m b.s.l. is around 4200 $m/s$ (intermediate), however, at 2000 m b.s.l. high velocity related to the granite is observed to the north of boreholes TR-19B and TR-19C.

The Vp and Vp/Vs velocity models do not show the granite rock clearly in the uppermost 2000 m b.s.l., which suggests that the area is affected by the injected fluid from injection wells, as well as, the natural recharge of the system by meteoric water near boreholes TR-5, TR-17 and TR-18. Figure 4.9 shows the possible base of the granite intrusion around 2500 and 2600 m b.s.l. from the 3D density model and 3D Vp seismic velocity model, respectively. In volcanic systems, high Vp/Vs (1.75-1.80) velocity anomalies, represent structural features associated with cooled magma bodies (Lees, 2007). The high Vp/Vs ratio velocity is directly related to high Vp velocity anomalies. In this case, the high Vp velocity identified at 2500 m b.s.l. could be related to a cooling heat source

in the geothermal system (see Figure 4.9).

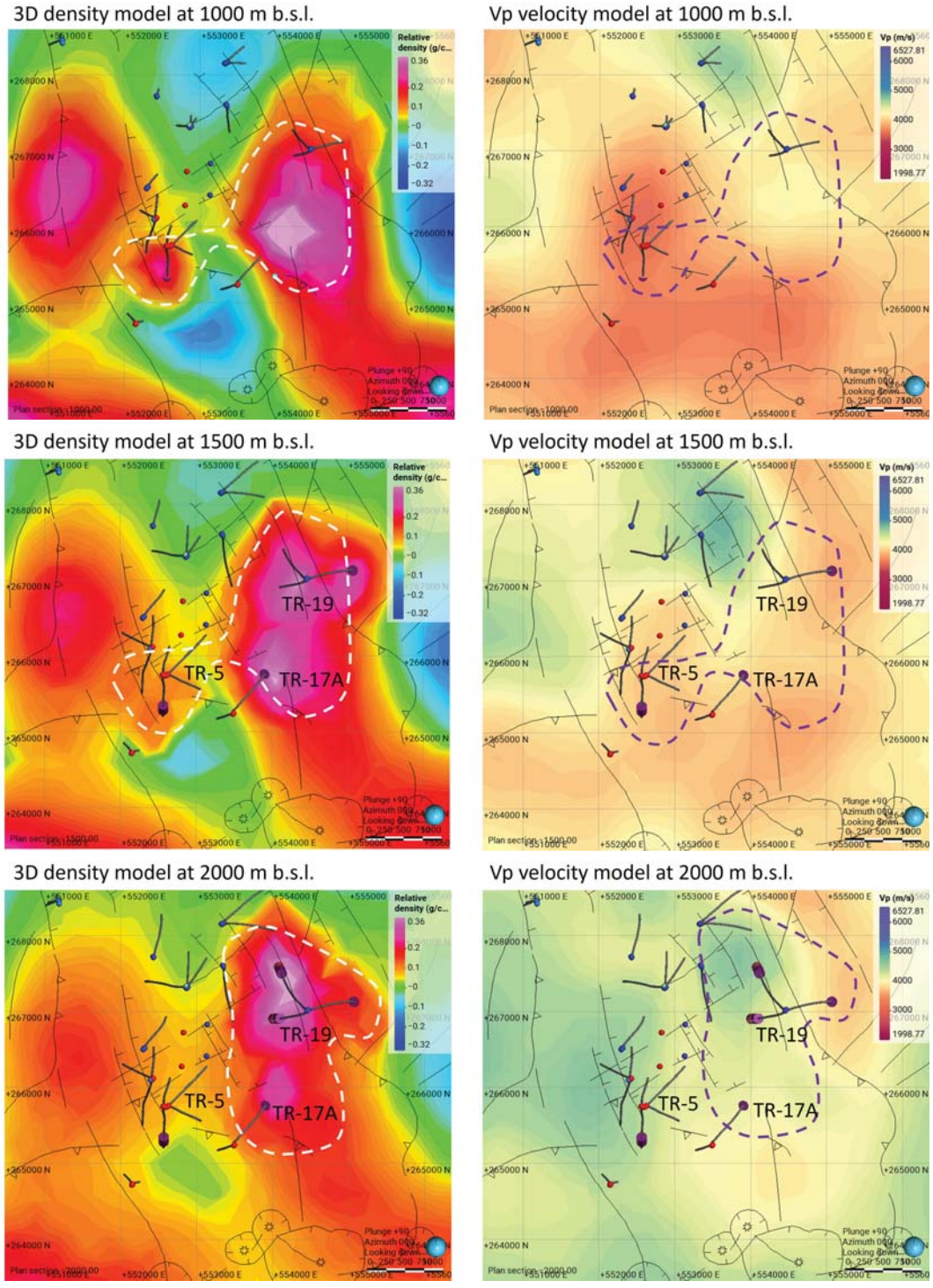


*Figure 4.8. 3D density model and Vp seismic tomography model (CGG, 2021) at different elevations. The maps emphasize the correlation between high-density anomalies and the P-wave velocity at 1000, 1500 and 2000 m b.s.l. The dashed white and purple lines represent the granite intrusion areas. The cutting samples are shown in boreholes TR-19A, TR-9B and TR-19C as purple-filled cylinders. The structural system is shown as black lines.*

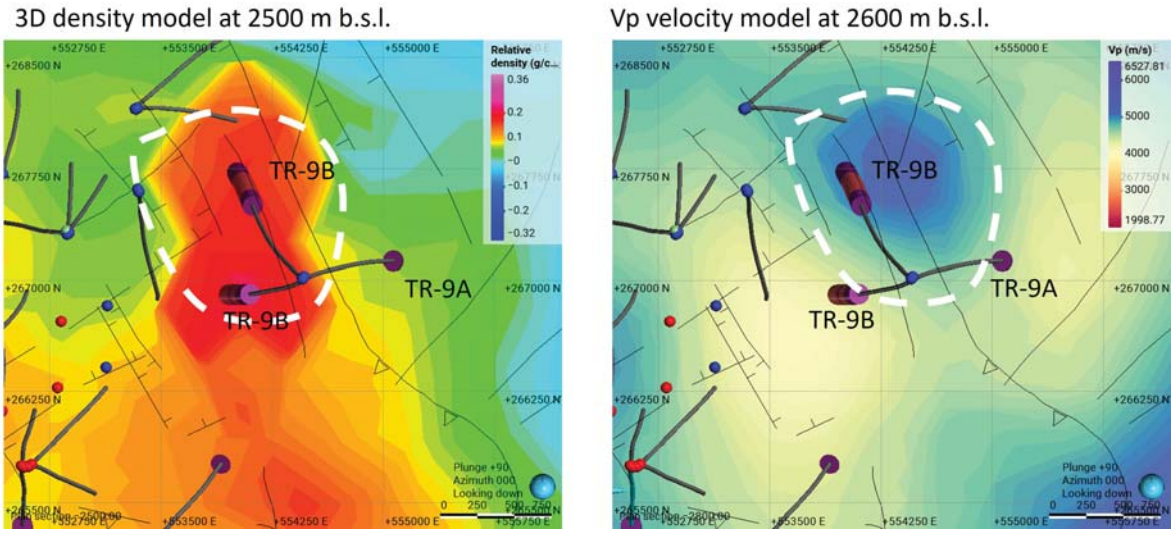


*Figure 4.9. 3D density model and Vp seismic tomography model (CGG, 2021) at 2500 and 2600 m b.s.l, respectively. The maps emphasize the correlation between high-density anomaly and high P-wave velocity related to the base of the granite rock in the area. The dashed white line represents the granite intrusion areas. The cutting samples are shown in boreholes TR-19A, TR-9B and TR-19C as purple-filled cylinders. The structural system is shown as black lines.*

## 4.3 Geothermal reservoir and steam zone

According to some authors, the low Vp/Vs velocity anomalies are related to high-temperature zones, steam-saturated formations and hydrothermally altered zones (Pavez et al., 2016). The hydrothermal reservoir of BGF has a liquid-dominated zone at its bottom and an upper zone that is vapour-dominated as a result of a boiling process in deeper parts of the reservoir (CGG, 2021). Figure 4.10 shows the liquid zone identified in boreholes TR-2, TR-4R, TR-4C, TR-5A, TR-5B, TR-5C, TR-5D and TR-18, the current steam zone identified in boreholes TR-18B, TR-18A and TR-17B and the probable steam zone still to be explored further in the Eastern part of BGF. The static water level in the wells is around 100 m a.s.l. The maximum temperature in each borehole is shown in Figure 4.10.

The reservoir is hosted in andesitic lavas and tuff compacted and fractured, which presents high hydrothermal alteration (propilitic facie) (LAGEO, 2019). The reservoir is identified between 800 and 1700 m b.s.l. in the southern part of the geothermal field and is liquid-dominated. Figure 4.11 shows a map at 500 m b.s.l. that corresponds to the base of the steam zone intercepted in boreholes TR-18B and TR-17B and a map at 700 m b.s.l. that corresponds to the top of the liquid-dominated reservoir. Both maps show a high-density anomaly in the southwest part of BGF with values around 2.4-2.5 $g/cm^3$, which is limited in the south by a low density between 2.18 and 2.16 $g/cm^3$ in TR-18B and TR-17B, respectively, related to the steam zone (see Figure 4.11). In the northern part of BGF, a low-density anomaly is observed, which could be related to a boundary structure.

The steam zone (low-density anomaly) is confined by the El Hoyón and San Juan faults,

which probably create a horst in the area. The low-density anomaly is limited to the north by the Blanca Rosa caldera border and the structural border in the west and east of BGF.

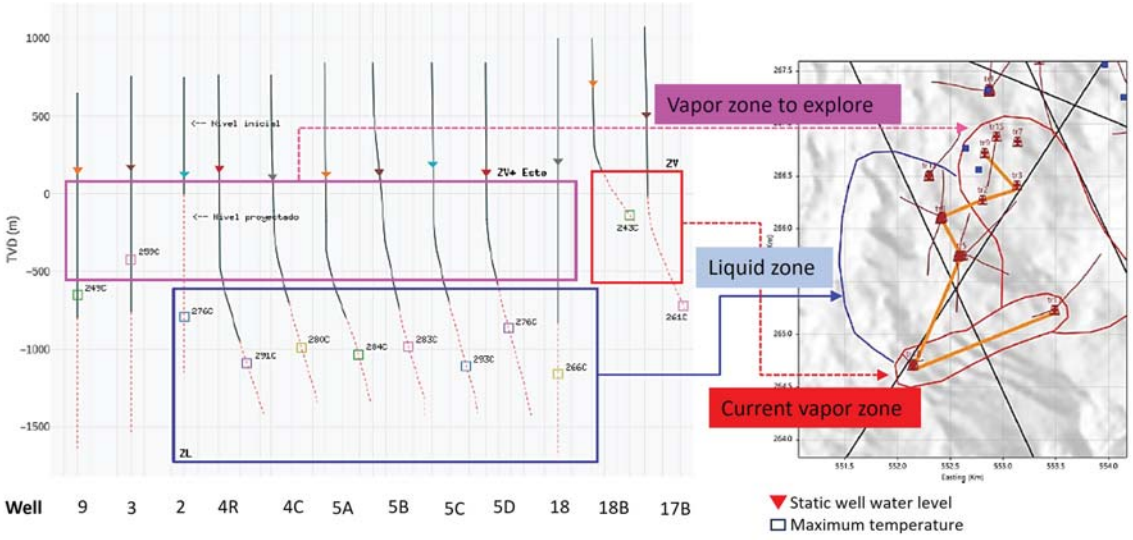


*Figure 4.10. Schematic well distribution as a function of depth (TVD in meter) and map of the steam and liquid zone and the proposed steam zone for future explorations in BGF.*

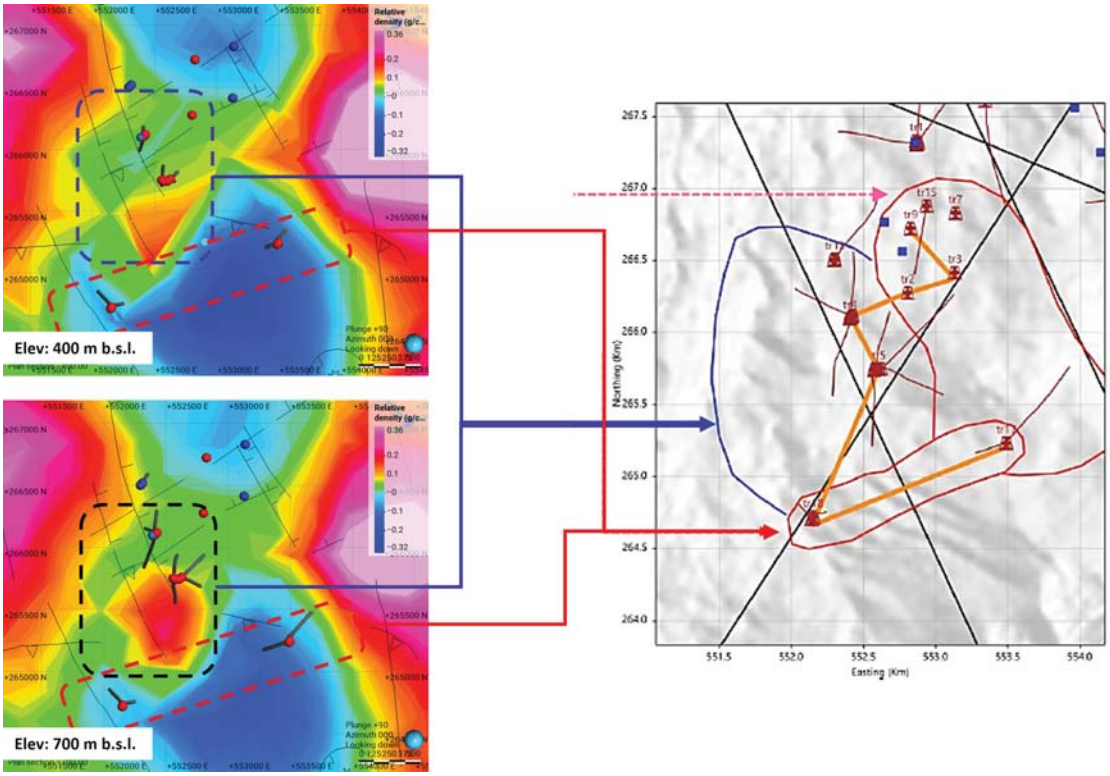


*Figure 4.11. 3D density model at 400 and 700 m b.s.l. The inset map shows the correlation between the high-density anomalies related to the top of the liquid-dominated zone and the low-density anomalies in the south area related to the steam zone.*

In the main production area, the low-density material is identified below 2000 m b.s.l. and deepens to 4500 m b.s.l. in the southern part of BGF (see Figure 4.12). The low Vp/Vs ratio values are between 1.4 and 1.45, which, according to some references, is related to rock with steam/gas-filled pores (Hersir et al., 2022) and zones with steam saturated to high temperature (Pavez et al., 2016). Figure 4.13 shows the SW-NE cross section of low-density anomaly related to the steam zone intercepted by boreholes TR-17B and TR-18B.

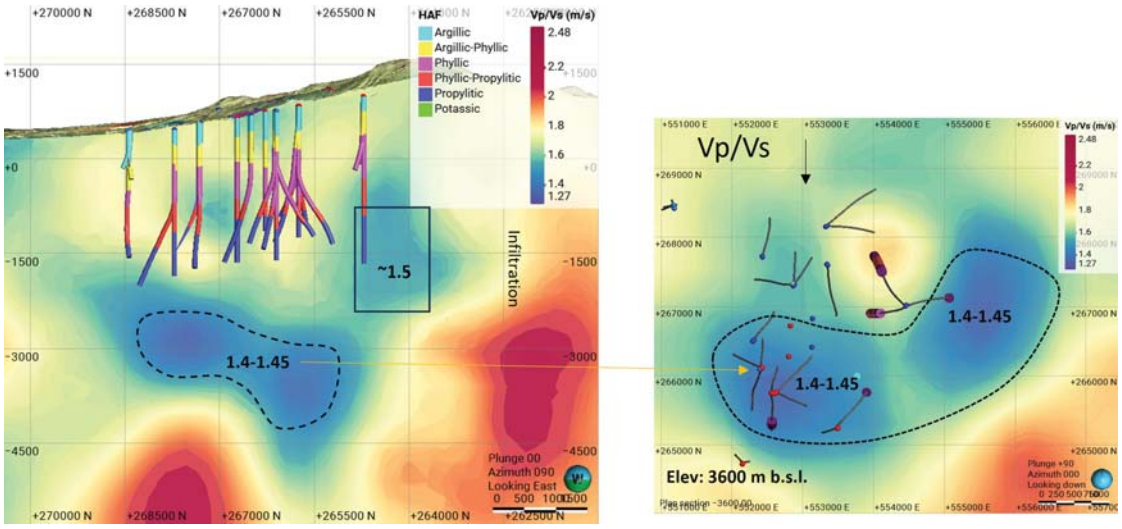


*Figure 4.12. Seismic tomography of Vp/Vs ratio (CGG, 2021). The N-S cross section shows the area with high content of steam storaged in the geothermal system (dashed black contour and black box). The map at 3600 m b.s.l. shows the base of the low Vp/Vs ratio (dashed black contour) in the main production area of BGF.*

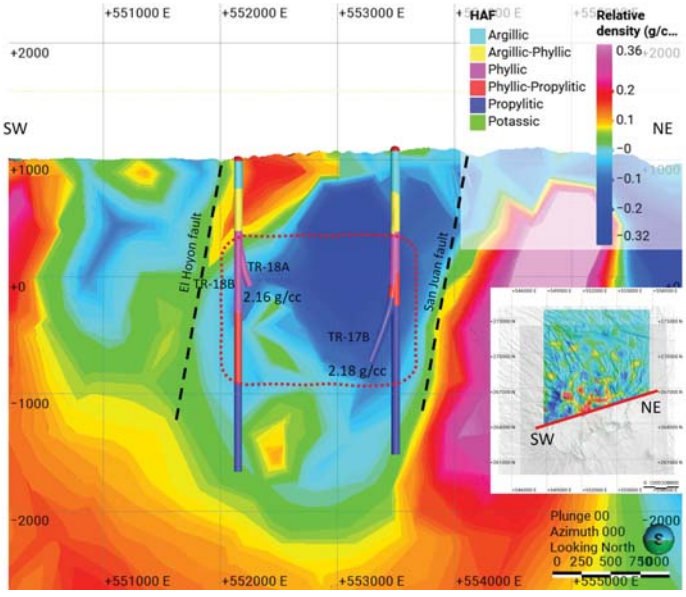


*Figure 4.13. 3D density model. The SW-NE cross section shows the area of low-density anomaly related to the steam zone intercepted by boreholes TR-17B and TR-18B. The faults are shown as dashed black lines, the steam zone with similar density values inside the red box. The inset map shows the location of the cross-section.*

## 4.4 Structural system

Some geological structures have not been confirmed by geological evidence in BGF. However, in this study, some fractures and caldera borders that cross the geothermal field are proposed based on the density inversion model and the horizontal gradient of CBA.

In section 3.4.1, the unconstraint and constrained density model of the regional anomaly based on gravity data reveals three high-density contrasts that could be related to three caldera borders (see Figure 3.18 and 3.19). In the southern part is inferred the Blanca Rosa caldera, in the center the Berlin Caldera and a third caldera in the northern part of the geothermal field. The caldera borders have not been evidenced on the surface by geological studies; however, in this study, the caldera borders are inferred as high-low density contrast. The horizontal gradient at different wavelengths (1000, 2000, and 3000 m) is used to confirm the caldera border in the south and north of BGF (see Figure 3.25, 3.26 and 3.27).

Figure 4.14 shows the horizontal gravity gradient using a wavelength of 1000 m. The map shows several low-gravity contrasts (blue color) related to surficial structures as fractures (inferred) and confirmed faults. Three fractures coincide with the feedzones of boreholes TR-5C, TR-17B and TR-17C, indicating their probable existence.

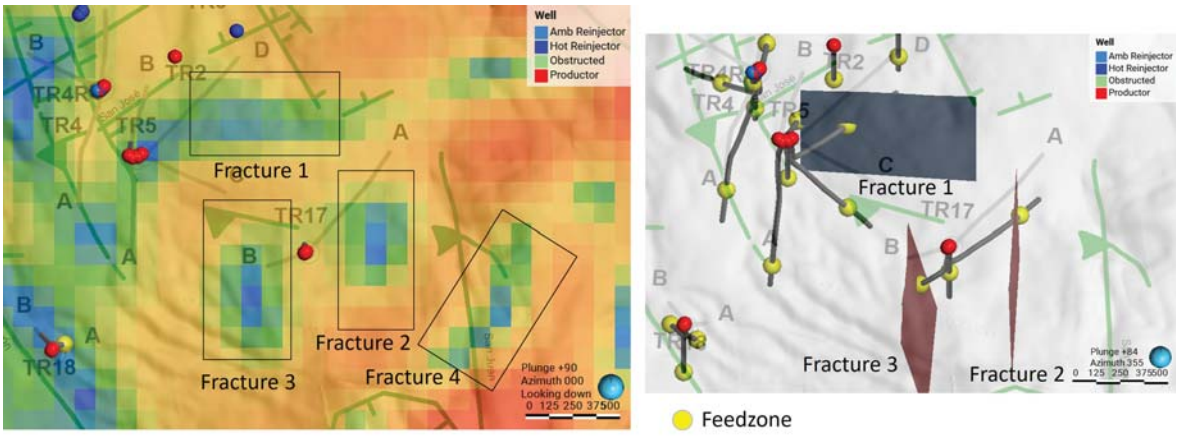


*Figure 4.14. Horizontal gravity gradient map of CBA with a wavelength=1000 m. The map shows surficial anomalies that could be associated to inferred fractures. The fractures coincide with the feedzones of boreholes TR-5C, TR-17B and TR-17A.*

## 4.5 Conclusions

The 3D density model from gravity data and the seismic tomography have demonstrated to be complementaries to characterize some features of BGF.

The upflow zone is identified as a high-density anomaly (2.5-2.6 $g/cm^3$), related to the deep hot fluids that travel from a transition zone (liquid-steam) to the reservoir related to low Vp/Vs anomalies. The high-density anomaly is associated with hot fluids and the deposition of minerals through its pathway until it reaches the convection zone. The

ascent of hot fluids towards boreholes TR-17 and TR-18 is probably influenced by the Blanca Rosa Caldera. The high-temperature isotherms confirm the identified upflow.

The 3D constrained inversion model and Vp velocity model confirm and characterize the granite intrusion rock. The 3D density model evidences the granite from 1000 to 2500 m b.s.l., however, the Vp seismic velocity model doesn't show a strong relation between high-density anomalies and the granite rock at the same depth, probably due to the influence of injection of fluids in the zone. The granite is identified in both models at 2500 m b.s.l., which suggests the bottom of the granite rock. The density for the granite is approximately 2.67 $g/cm^3$ and the P-wave velocity is around 5200 $m/s$ at 2600 m b.s.l.

The deep geothermal reservoir is related to low Vp/Vs anomalies and high temperatures. The low Vp/Vs ratio is related to steam-saturated formations and hydrothermally altered zones (andesitic lavas and tuff, with high hydrothermal alteration). The liquid-dominated reservoir is located between 800 and 1700 m b.s.l. in the southern part of the geothermal field with values around 2.4-2.5 $g/cm^3$.

The steam zone is confined by the El Hoyón, San Juan faults, and Blanca Rosa caldera, possibly creating a horst geological formation in the area. The low-density material is found below 0 m b.s.l. near borehole TR-18A and TR-18B and deepens toward the TR-17B with a density around 2.16-2.18 $g/cm^3$.

# 5 Play Fairway Analysis (PFA): A 3D favorability model of BGF

Play Fairway Analysis (PFA) is a spatial and geostatistical approach that has been applied in the gas and oil industry. In recent years, it has also been used to improve success rates for geothermal exploration drilling (Pauling et al., 2023). This method helps to identify the most prospective areas for further exploration and development, which reduces the cost of drilling and a the same time the cost of geothermal projects.

The geothermal PFA methodology involves systematically screening a set of geographical areas for promising qualities, typically related to the presence of heat, permeability, and fluid. Successful application of PFA can identify hidden hydrothermal systems (Pauling et al., 2023). The key parameters of the resource from each geological and geophysical model are identified and integrated to constrain the favorability model that shows areas with prospectivity. As more data and parameters are added, the favorability model is influenced, resulting in different target zones. A proportional factor number (weight number) is assigned to the parameters to evaluate their influence and impact on the favorability model.

In 2021, the first PFA model was developed based on the updated conceptual model from 2019 with additional information from boreholes (temperature, lithology, hydrothermal alteration facies), geophysical studies (resistivity and seismic hypocenters), and geological faults. The results suggested eight favorability areas between 80-100% in BGF (Hernández, 2021). This study applies an updated PFA model using the previous models and the addition of new 3D models such as the 3D density, Vp and Vs velocity models, and the Vp/Vs ratio model. The updated PFA model is concordant with their importance as related to the geothermal system. Twelve parameters were categorized and combined to construct the favorability model of BGF.

The purpose of this analysis is to select the best sites for drilling new production or exploration wells. It does not consider the selection of drilling sites for injection wells.

## 5.1 Data

Geothermal PFA projects require specific combinations of datasets and weightings, depending on data availability, the conceptual understanding of the study area and the geothermal system present. In a geothermal system, key elements must be identified, such as the reservoir, caprock, upflow, flow paths, high-temperature zones, faults or fractures, hydrothermal alteration minerals, recharge and discharge. The key elements play together to construct a model that shows the most favorable areas for drilling, which must have high temperatures, permeability, steam, and hot fluids circulating in the system. The identification of the geothermal reservoir is not only the criteria for

the exploitation to be feasible; it also tells if it is economically viable.

All surface and subsurface data contribute to identifying these elements. For this study, the following datasets were available: 1) hydrothermal alteration facies, 2) lithological units, 3) distribution of faults, 4) seismic hypocenters, 5) resistivity model, 6) P-wave velocity model, 7) S-wave velocity model, 8) Vp/Vs ratio, 9) density model, 10) static temperature logs, 11) feedzones, and 12) location of recent wells. Volumes were generated in Leapfrog Energy softwares for each dataset; however, other specialized softwares can also be used.

The weighting process in geothermal PFA projects commences with a thorough review of each data set. These datasets must be available as a 3D layer or volume and strictly related to the geothermal reservoir. After verifying the parameters related to the reservoir, an index model for each parameter is categorized into six types based on specified conditions, representing their favorability from zero to five. Finally, each categorized parameter is weighted by multiplication with a unique factorization number, which measures the sensitivity of the parameters proportionally. In the following paragraphs the 3D inputs models are briefly explained.

### 5.1.1 Temperature model

In a geothermal reservoir it is critical to identify areas of highest temperature. It is an indicator of potential targets for exploration and exploitation. Figure 5.1(a) shows a model of the stabilized temperature (temperature profiles were measured approx. five years after drilling), indicating the highest temperature from the south to the center of BGF. In this case the most favorables areas correspond to temperatures $> 260$°C.

### 5.1.2 Lithology and hydrothermal alteration facies

The 3D lithology and hydrothermal alteration facies models are the same ones as used in previous studies (Hernández et al., 2023), which correspond to the information given in the conceptual model from 2019 (LAGEO, 2019) and described in Chapter 2. The reservoir is located in Unit IV, which is made up of andesitic lavas (see Figure 5.1(b)) and the propylitic alteration facie, which is related to high content of epidote, quartz and calcite formed at temperatures between 260°C and 300°C (see Figure 5.1(c)).

### 5.1.3 Feedzones

The feedzones are good indicator of permeability in a geothermal system and, for that reason are key target areas in geothermal boreholes. They indicate the productivity of a borehole in terms of hot fluids (water or steam) from the reservoir to the surface. In this study, the areas near to the feedzones are used to construct a distance function from the feedzone (0 m) to a specific distance (250 m). Figure 5.1(d) shows the 3D distance function of the feedzones.

### 5.1.4 Resistivity model

According to the resistivity model discussed in Chapter 2, the reservoir of BGF is identified as an upper part of a deep resistive dome, identified by MT, with resistivity in the range of 40 to 90 $\Omega m$ (LAGEO, 2019). A transition zone above the reservoir

is identified with a resistivity between 10 and 30 $\Omega m$. Figure 5.1(e) shows the 3D resistivity model.

### 5.1.5 Density model

In Chapter 3 a 3D density model based on gravity data was discussed, where the reservoir is identified with density values around 2.4-2.7 $g/cm^3$. A transition zone is observed with density between 2.0 and 2.4 $g/cm^3$ and the caprock with density around 1.7-2.0 $g/cm^3$ (see Figure 5.1(f)).

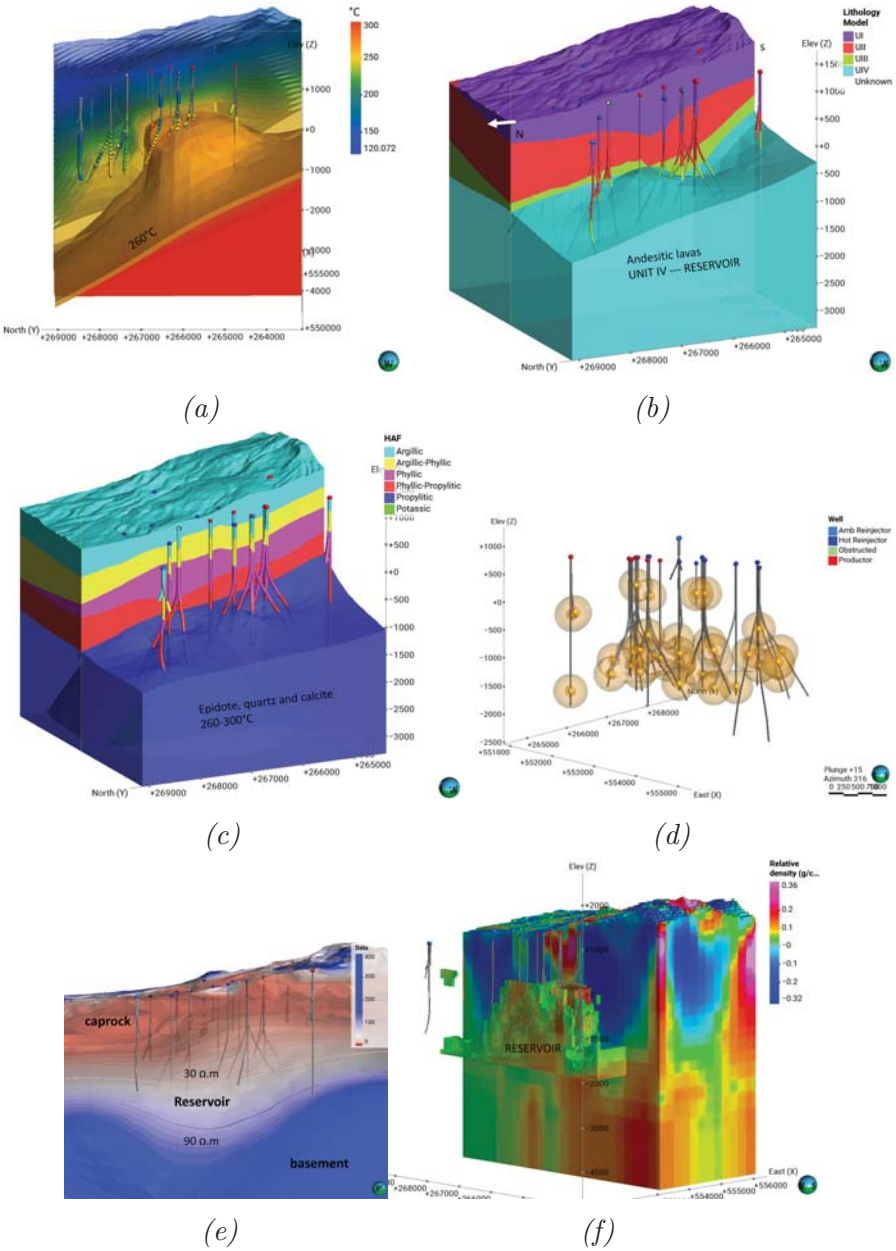


*Figure 5.1. Index models used to create the favorability model of BGF (a) stabilized temperature model (b) lithology model (c) hydrothermal alteration facies (d) distance function of feedzones (e) resistivity model from MT/TDEM surveys (f) density inversion model.*

### 5.1.6 Vp and Vs seismic tomography

P- and S-wave seismic velocities are a valuable tool for characterizing geothermal reservoir, as it helps to understand the subsurface properties and optimize drilling and production strategies. In this study, the P-wave velocity (see Figure 5.2(a)), which is a compressional wave velocity (Vp), varies from 3850 to 4250 $m/s$ in the geothermal reservoir, and the S-wave velocity (see Figure 5.2(b)), which is a shear wave velocity (Vs) ranges between 2275 and 2600 $m/s$. The Vp/Vs ratio (see Figure 5.2(c)), which helps identify potential reservoir zones, has values between 1.60-1.75 in the reservoir. However, a possible zone of steam-filled rocks has been identified below 2000 m b.s.l. with values between 1.4 and 1.45.

### 5.1.7 Hypocenters

The hypocenters refer to fracture zones in the subsurface, where a rupture or release of energy occurs due to earthquakes. The areas where the hypocenters are located could be related to the movements of fluids within the subsurface and can provide insights into the distribution of faults and fractures within the reservoir. In this study, the hypocenters are regarded as indicators of permeability and have been used to construct a distance function from the hypocenter to a specific distance. Figure 5.2(d) shows the 3D distance function of the hypocenter.

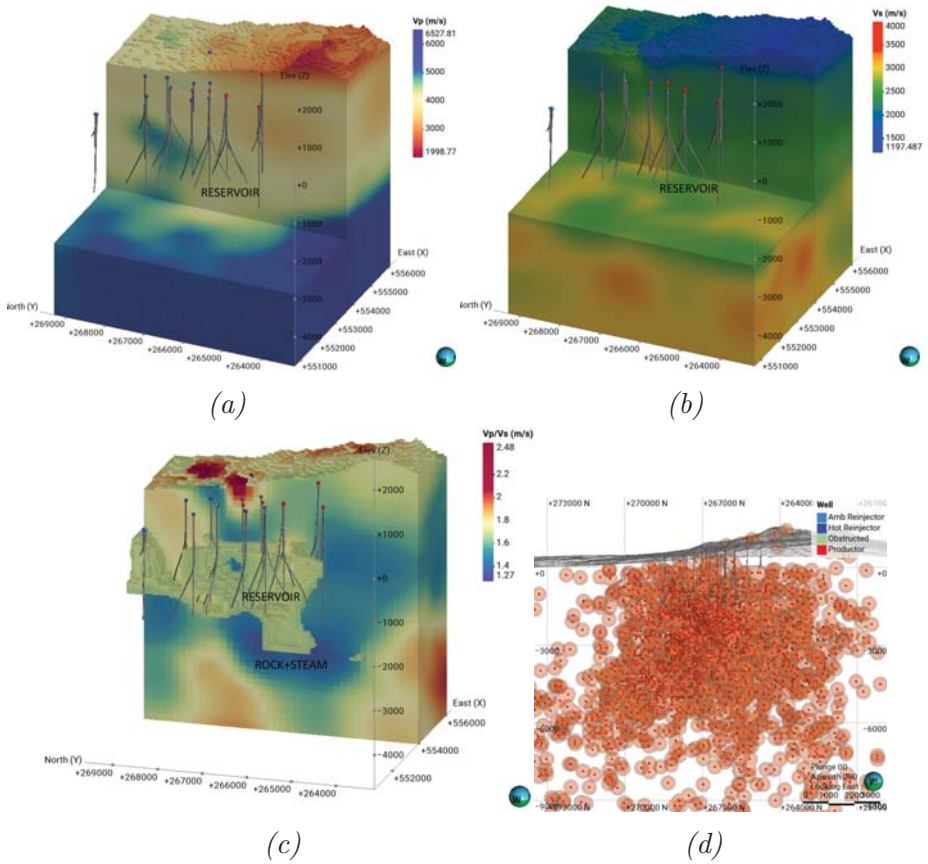


*(a)* *(b)*

*(c)* *(d)*

*Figure 5.2. Index models used to create the favorability model of BGF (a) P-wave seismic velocity model (b) S-wave seismic velocity model (c) Vp/Vs ratio model and (d) distance function of hypocenters.*

### 5.1.8 Faults

The structural system is a key parameter to identify possible permeable areas where the hot fluids travel from the reservoir to the surface. The faults have been delimited to the production area and include the confirmed faults, three fractures inferred from the horizontal gradient of CBA, and Blanca Rosa caldera (see Figure 5.3(a)). The most favorable areas correspond to those that are closer to the faults (< 50 m).

### 5.1.9 Boreholes

The purpose of this study is to propose areas that do not affect the production of the current wells in BGF. Therefore, a distance function is constructed using the traces of the production and reinjection wells. To avoid possible interference, areas nearest to the traces are not selected as a constraint for the favorability model. In this case, distances >200 m from the traces are the most favorable (see Figure 5.3(b)).

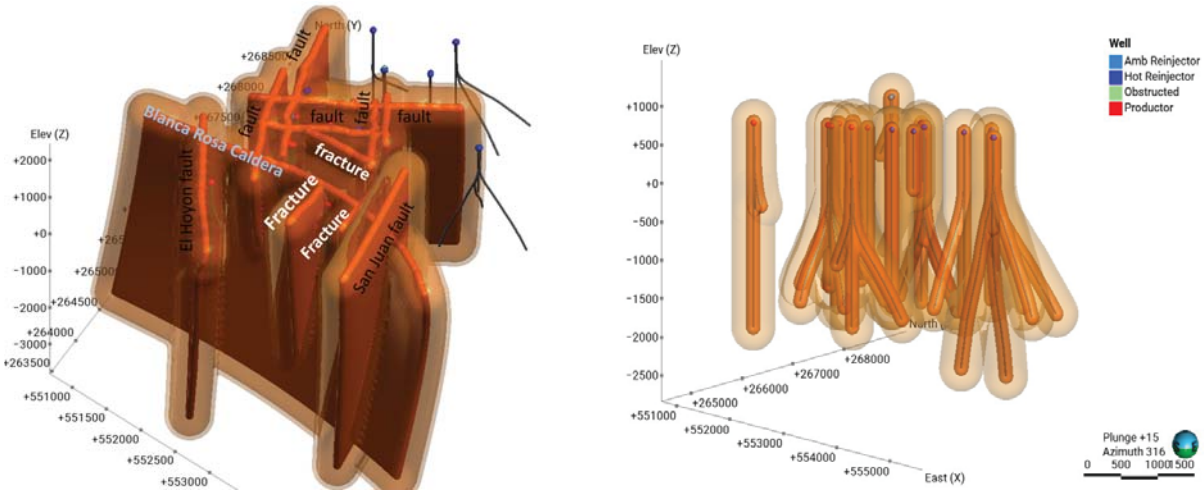


*(a)* *(b)*

*Figure 5.3. Index models used to create the favorability model of BGF (a) distance function of faults, fractures, and caldera (b) distance function of boreholes.*

## 5.2 Method

In this work, the favorability model is related to the parameters that best describe the geothermal reservoir (see Figure 5.1, 5.2 and 5.3), which have been carefully selected. The parameters are categorized into an Index Model (IM) for each 3D model based on specified conditions into six types representing their favorability from zero to five. The five categories represent the most favorable layer or volume, and zero attributes to the least favorable area.

The categorization is made through a regular block model with cells of the same size, 50 x 50 x 50 m, for the X, Y, and Z axes. The block model is widely used in the mining industry for mineral resource estimation as it also facilitates the use of advanced geostatistics (Poux & O'Brien, 2020). Figure 5.4 shows the block model used in the application of the PFA method.

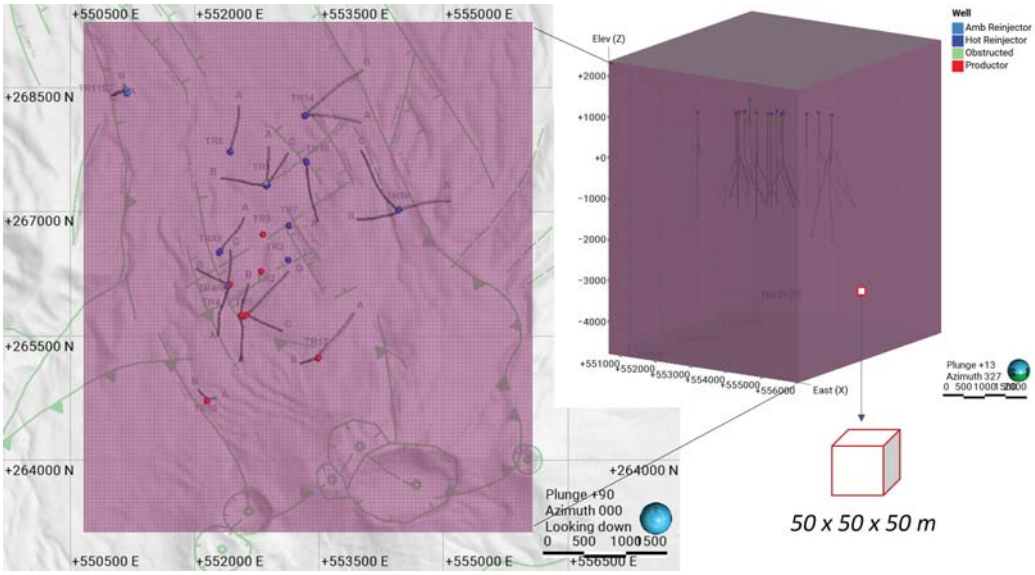


*Figure 5.4. Block model used for the categorization and weighting of parameters related to the geothermal system. The map shows the extension of the block model inside the exploited area. The red cube on the figure to the right indicates the size of each cell in the block model.*

For the analysis, twelve 3D IMs were constructed based on geoscientific data and borehole parameters within Leapfrog Geothermal, which gives the tool to run calculations, apply filters and to do conditional queries on the data for each of the blocks to complete the Play Fairway Analysis. The IMs were created using a conditional query (type IF) on the values or layer assigned into six categories representing their degree of favorability from zero to five, where five is assigned to the most favorable cell, and zero attributes to the least favorable area. Table 5.1 shows the categorization for each IM from boreholes and Table 5.2 shows the categorization for geoscientific data.

Once, all the IMs are created, the last step consists in combining them all into one main Favorability Index Model, which shows the most promising areas for drilling based on the convergence of the best parameters.

*Table 5.1. Index Model (IM) from well data and categorization*

| **Index Model (IM)** | **Categorization** | | | | | |
|---|---|---|---|---|---|---|
| | **0** | **1** | **2** | **3** | **4** | **5** |
| 1. Lithology IM | Otherwise *ignored* | empty *ignored* | Unit I *superficial materials* | Unit II *pyroclastics* | Unit III *tuff* | Unit IV *andesite and lavas* |
| 2. Hydrothermal facies | Otherwise *ignored* | argillic *50-150°C* | argillic-phyllic *150-180°C* | phyllic *200-230°C* | phyllic-propylitic *230-260°C* | propylitic *260-300°C* |
| 3. Temperature | Otherwise | <75°C | 75-175°C | 175-225°C | 225-260°C | >260°C |
| 4. Dist. to feedzones | Otherwise | 200-250 m *low-perm* | 150-200 m | 100-150 m | 50-100 | <50 m *high-perm* |

*Table 5.2. Index Model (IM) from geoscientific data and categorization*

| Index Model (IM) | Categorization | | | | | |
|---|---|---|---|---|---|---|
| | **0** | **1** | **2** | **3** | **4** | **5** |
| 5. Resistivity IM | Otherwise *ignored* | <10 $\Omega m$ *caprock* | 10-20 $\Omega m$ *transition zone* | 20-30 $\Omega m$ *top reservoir* | 30-90 $\Omega m$ *reservoir* | <100 $\Omega m$ *bottom reservoir* |
| 6. Density IM | Otherwise *ignored* | <1.6 $g/cc$ | 1.7-2.0 $g/cc$ *caprock* | 2.0-2.4 $g/cc$ *transition zone* | 2.4-2.5 $g/cc$ *reservoir* | <2.7 $g/cc$ *bottom reservoir* |
| 7. Vp tomography IM | Otherwise *ignored* | <2249 $m/s$ *recharge zone* | 2249-3242 $m/s$ | 3242-3700 $m/s$ *transition zone* | 3700-3950 $m/s$ *top reservoir* | 3950-4250 $m/s$ *reservoir* |
| 8. Vs tomography IM | Otherwise *ignored* | < 1940 $m/s$ *recharge zone* | 1940-2000 $m/s$ | 2000-2050$m/s$ *steam zone* | 2050-2275$m/s$ *transition zone* | 2275-2600$m/s$ *reservoir* |
| 9. Vp/Vs ratio IM | Otherwise *ignored* | <1.3 | 1.3-1.40 | 1.40-1.45 *rock+steam* | 1.45-1.60 *transition zone* | 1.60-1.8 *reservoir* |
| 10. Distance to faults IM | >300 m | 250-300 m | 200-250 m | 150-200 m | 100-150 m | <100 m |
| 11. Distance to hypocenter IM | >300 m | 250-300 m *low-perm.* | 200-250 m | 150-200 m | 100-150 m | <100 m *high-perm.* |
| 12. Distance to boreholes IM | <100 m *high-risk* | 100-150 m | 150-200 m | 200-250 m | 250-300 m | >300 m *low-risk* |

After categorizing, each index model is weighted by multiplication with a unique factorization number between 0 and 2 for an easier interpretation of the results (see Figure 5.5). The lowest factor represents the least important parameter and the highest factor the most important parameter. The influence of each index model is based on the parameter that best characterizes the reservoir, steam areas and upflow zones. The rest of the factor numbers are related to intermediate values that suggest evidence of favourable areas but not strongly.

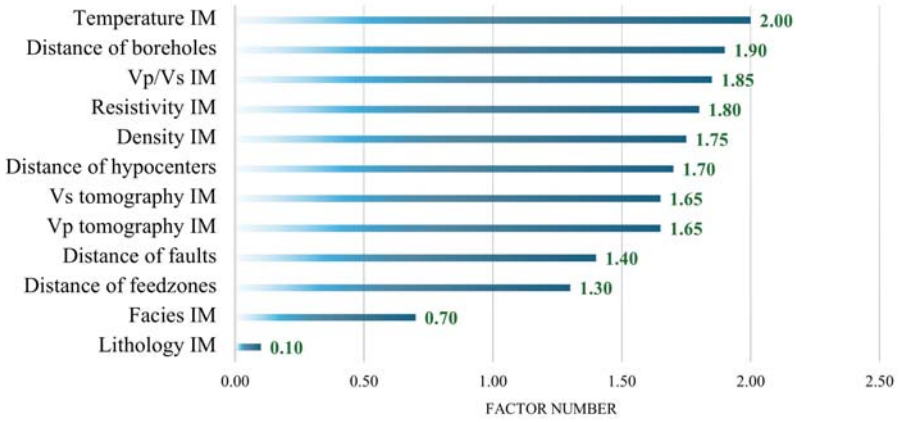


*Figure 5.5. Factorization number for the Index Model (IM) used in the Favorability Model assessment*

## 5.3 Results

The results show the critical role played by each parameter in the PFA method. Therefore, it is easy to see that as more parameters are added to the Favorability Index Model, the area with the best characteristics related to the reservoir is increasingly delimited. Figure 5.6 shows six Favorability Index Models (FIM) with an index >0.75 from a simple model that is limited to information from boreholes to a more complex model that includes all the area's available data.

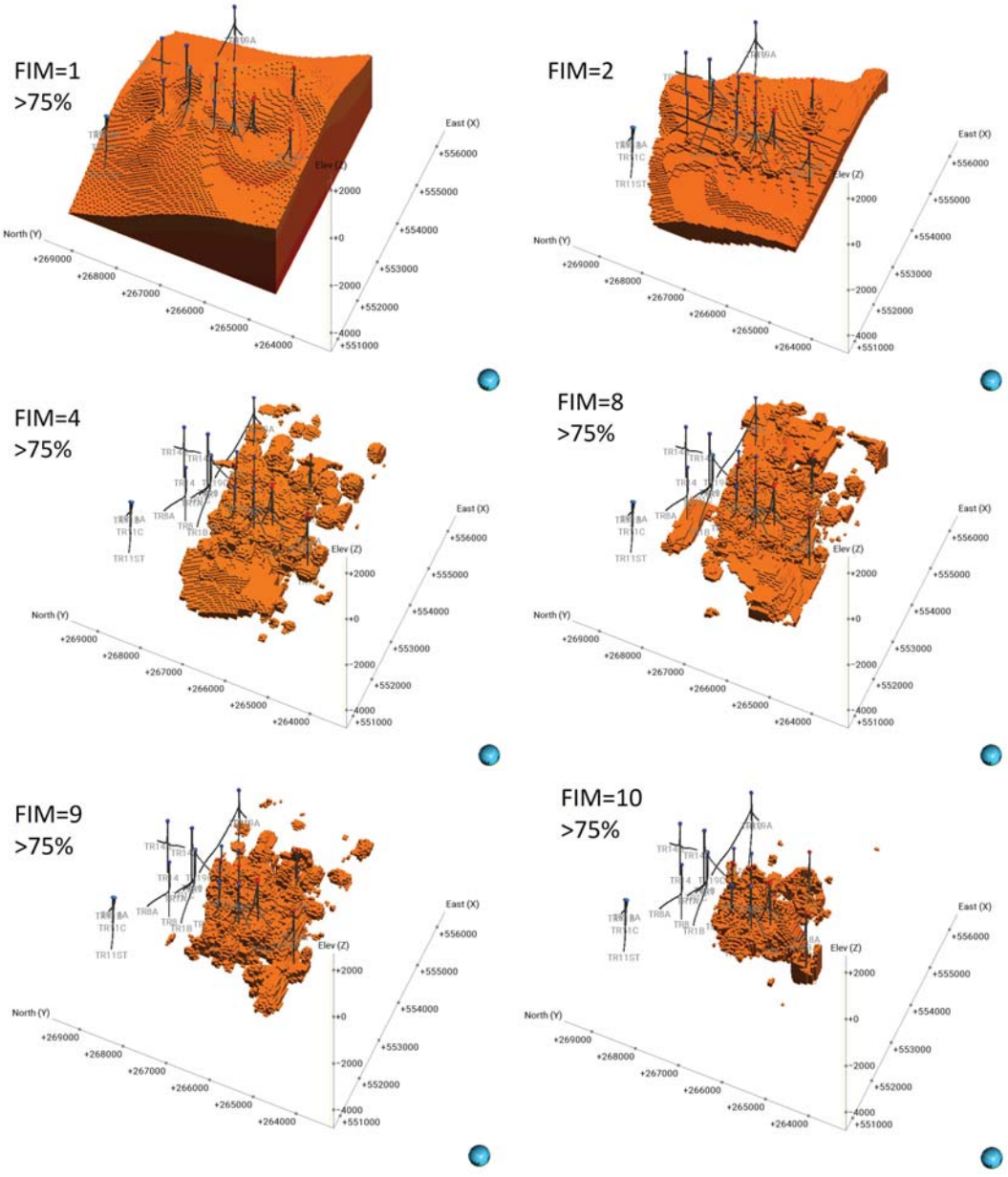


*Figure 5.6. 3D Favorability Index Model (FIM), orange blocks show the Index of 0.75 (75%) and above.*

The selection of the best Favorability Index Model is based on the statistics of each FIM shown in Figure 5.7 and 5.8. The spider chart visualizes a dataset's highest and lowest values, which is ideal for showing the influence of the variance and standard deviation

from each FIM. The standard deviation is a measure of the amount of variation or dispersion of the values. It is smaller for FMI 10 than for the others. The variance, which indicates how spread out the data are from the mean, is smaller for FIM 10 than for the rest. The graphs show that statistically, the FIM 1 is the least accurate model with the highest standard deviation and variance, while the FIM 10 is the best FIM with the slightest standard deviation and variance.

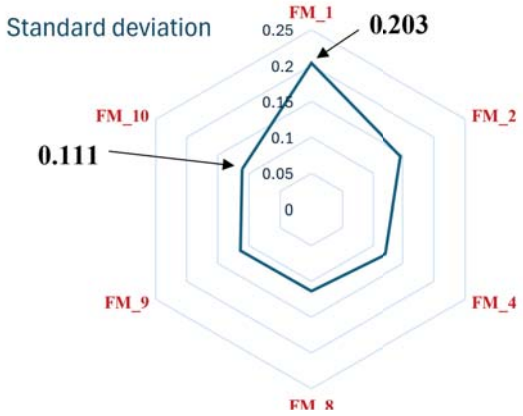


*Figure 5.7. Distribution of standard deviation. The spider chart depicts the influence between the parameters of each FIM. The FIM 1 is least accurate model with highest standard deviation and FIM 10 is the best index model with the smallest standard deviation.*

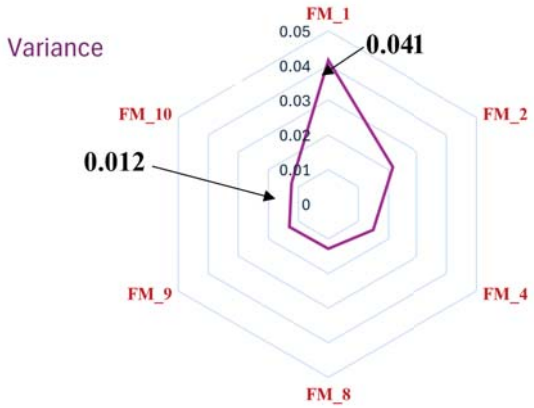


*Figure 5.8. Distribution of variance. The spider chart depicts the influence between the parameters of each FIM. The FIM 1 is least accurate model with highest variance and FIM 10 is the best index model with the smallest variance.*

The resulting 3D FIM 10 is shown in Figure 5.9 and 5.10 with Index of 0.65 and 0.75, respectively. The models are sliced through to better visualize the production area with high favorability. The unsliced red zones represent the highest favorability areas. It is clear that models with parameters related to the reservoir at elevation below 400 m b.s.l. play a significant role in the evaluation. Permeable zones above 400 m b.s.l. are not included in the most favourable areas due to not matching with the rest of the parameters as high temperatures and density related to the reservoir. It can also be noticed the areas around the wells have not been integrated in the evaluation. Figure 5.11 shows five favorable areas for drilling new production or exploration wells.

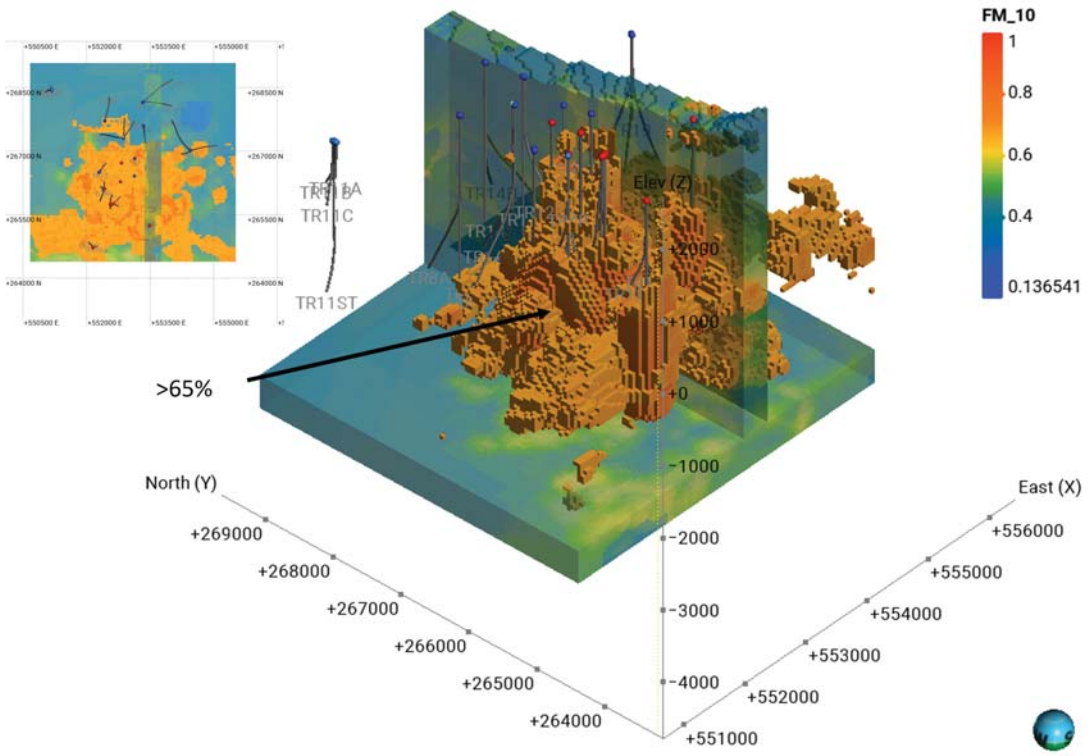


*Figure 5.9. 3D Favorability Index Model, orange blocks show the Index of 0.65 (65%) and above.*

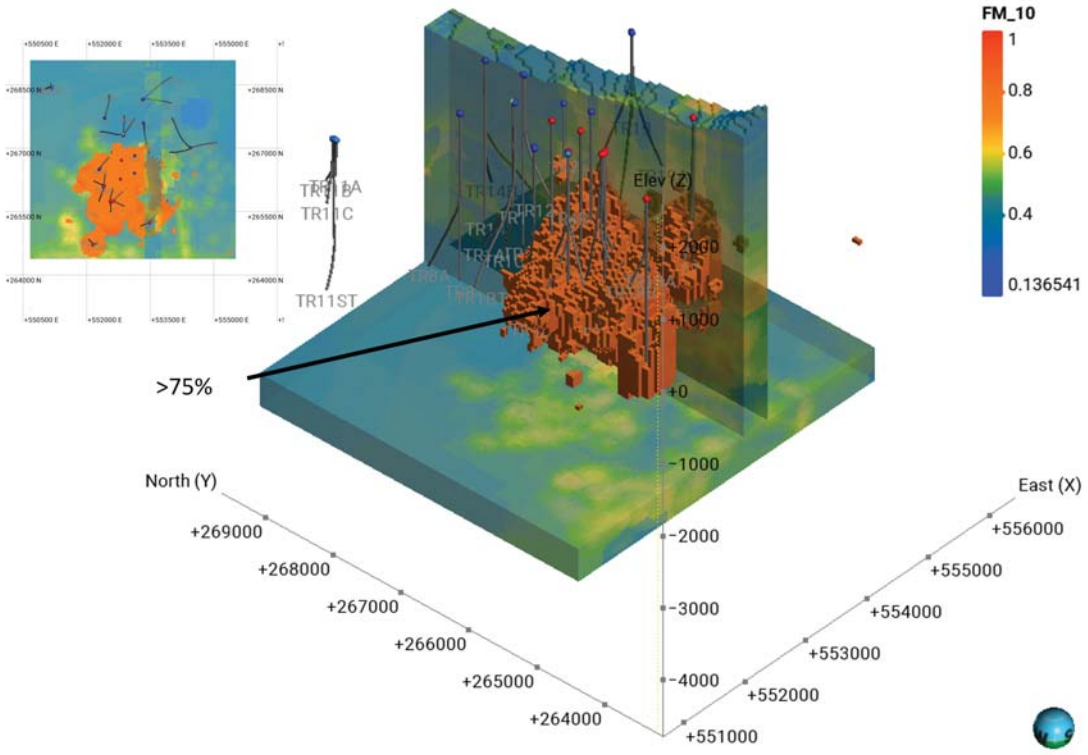


*Figure 5.10. 3D Favorability Index Model, orange blocks show the Index of 0.75 (75%) and above.*

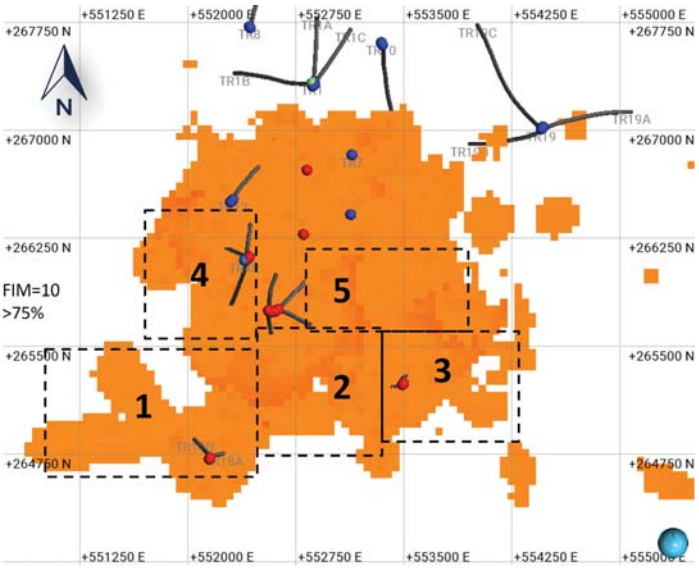


*Figure 5.11. Map of the FIM 10 with an Index >0.75 (75%). The dashed black squares show the most favorables target areas for drilling new wells.*

Figure 5.12 shows the histogram of the dataset volume (%) as function of Index values of the FIM 10. The histogram indicates the blocks with an Index value greater than 0.75 that represent about 8.5% of the data volume, and blocks with an Index value of 0.50 that represent about 68% of the total data. This confirms that the PFA method identifies only limited areas related to a specific categorization of parameters and weights, which emphasize the identification of drilling targets in the geothermal field.

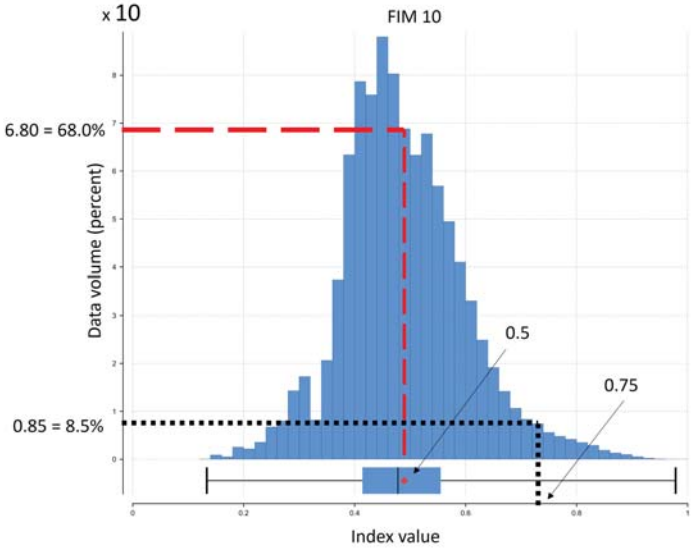


*Figure 5.12. Histogram of the Index favorability value of the FIM 10. The dashed red line indicates the Index value greater than 0.5 and the dotted black line the Index value greater than 0.75 with a data volume percentage of 68 and 8.5%, respectively. The index favorability value is shown in X-axes from 0 to 1, where 1 is related to the 100% of favorability.*

## 5.4 Conclusions

This study presents a PFA for the actual production area, where the production wells are located in BGF (the injection area is not considered in this study). Twelve 3D models were used to build six Favorability Index Models (FIMs). Geochemical data from wells were not included due to their unavailability. The faults, caldera borders, traces of boreholes, feedzones and hypocenters located in the north of BGF were not included to avoid an increase in the uncertainty in the data and distorting the result in our favorability model.

This study demonstrates that the availability and limited distribution of the datasets affects the FlM. The most favorable areas tend to occupy the block areas with a higher density and frequency of datasets. These block areas are consistently associated with clustered feedzones, structures, and hypocenters. The influence of geophysical data is critical in this study, as they present essential characteristics at great depth about the geothermal reservoir, while information from wells and surficial data are more limited at depth, for which the temperature, hydrothermal alteration facies, lithology models, as well as the distance functions, are limited at the maximum depth of the deepest borehole to avoid extrapolation and high uncertainties in the FIM.

FIM 10 is the most favorable FIM because it contains all the best-graded parameters. The selection of FIM 10 is based on standard deviation, variance and constrained results in the geothermal reservoir of BGF. The simple models reveal higher standard deviation, variance, and area extension in the FIM model than those more complex as FIM 10, which were regarded as the best FIM. Overall, the Favorability Index Model suggests five areas for further exploration, which matches with the present conceptual model of BGF. This suggests that the model is reliable and reasonably assessed.

# 6 Discussion

In the current study, different models that indicate and propose several main features of the Berlín Geothermal Field in El Salvador are produced. The main features presented and described here are based on the 3D density inversion model, gravity horizontal gradient analysis, and the Vp, Vs and Vp/Vs ratio. The density inversion model discussed in Chapter 3 shows the relevance of including additional known parameters in the geophysical inversion to reduce the ambiguity of the results and get more reliable and geologically correct inversion models. The first constrained model using a homogeneous density layer linked to the caprock reflects fewer heterogeneities due to the restrictions of density inside the iso-surface than the one without constraints. The second constrained model reflects a good response to the bulk density of granite and altered andesite lava rocks. This is observed with the comparison of density between the inversion model and the measured density from the cutting samples from boreholes TR-19B and TR-19C. From the three types of density models (one unconstrained and two constrained) it is possible to observe a surficial low-high density contrast associated with the presence of caldera borders (Blanca Rosa caldera, Berlín Caldera, and an inferred third caldera), which indicates a strong source in the inversion model. The gravity horizontal gradient confirms the presence of those calderas' boundaries at a similar location. In general, the low-density anomalies between the faults are interpreted as a weak zone which can be interpreted as a graben or horst within the geothermal system.

The geothermal reservoir is divided into two zones; the first one is a liquid-dominated reservoir located between 800 and 1700 m b.s.l. in the southern part of the geothermal field with density values around 2.4-2.5 $g/cm^3$. The other one is a steam-dominated reservoir (steam-saturated rock and hydrothermally altered zones) between 2000 and 4000 m b.s.l. associated with low Vp/Vs between 1.4 and 1.55, which is in the range of other geothermal reservoir models (Hersir et al., 2022). The upflow zone is mainly identified by the high-temperature isotherms, however, in this study, the density model suggests a high-density anomaly (2.5-2.6 $g/cm^3$) related to the deep hot fluids that travel from a transition zone (liquid-steam) to the reservoir, which is also related to low Vp/Vs anomalies.

The influence of the injection of fluids in the geothermal system is evidenced in low-temperature measurements in the injection wells despite a granite intrusive has been identified in the area, which is related to high temperatures. This insight could be related to the cooling process of an old heat source. The 3D density model evidences the top of the granite at around 1000 m b.s.l., however, the Vp seismic velocity model doesn't show a strong relation. The granite is identified in both models at around 2500 m b.s.l., which is proposed to be the bottom of the granite rock with a density of around 2.67 $g/cm^3$ and the P-wave velocity of 5200 $m/s$.

# 7 Conclusions

This thesis confirms and defines some features of the conceptual model and favorability model, which can be used in future analysis to identify new target areas for drilling new production wells. The additions of more information and modifications can be made and more detailed using a smaller VOXI mesh than the one used in this study.

The 3D density inversion model and the gravity horizontal gradient maps allowed a better understanding of the permeability related to faults, fractures, and caldera borders that could affect the fluid patterns in BGF. From this result, three fractures are inferred and confirmed based on the possible contact with feedzones in boreholes TR-19B and TR-19C. Therefore, a detailed analysis is recommended to do a detailed analysis of the horizontal gradients from new gravity points collected in the area to confirm the structures, as well as more geological studies in the identified areas.

The density inversion model and the Vp/Vs ratio provide a better and more complete understanding of how fluid flows from greater depth toward the reservoir. The detection of significant increments or decreases of low Vp/Vs anomaly in the identified area through new results in the next years can help to evaluate changes in the system, i.e., a probable depletion of liquid water in the reservoir. Continuous monitoring of the three-dimensional Vp, Vs, and Vp/Vs ratio is an effective method of reservoir characterization and depletion monitoring in the geothermal field.

For the PFA method, the most reliable Favorability Index Model (FIM 10) was selected based on the best-graded parameters of the Index Models and statistical parameters (variance and standard deviation). The FIM 10 suggests five areas for further exploration, which matches with the conceptual model of BGF. This suggests that the model is reliable and reasonably assessed. Therefore, the approach used in this study is recommended to become part of the standard procedure for Play Fairway Analysis in the BFG in the future when more data are available.

Further improvements in the conceptual model and Favorability Index Model involve including the chemical processes occurring in the vicinity of boreholes, as well as the use of new geophysical datasets (gravity and passive seismic measurements) and geological measurements to update both geothermal models.

# References


Amoroso, O., Napolitano, F., Hersir, G. P., Agustsdottir, T., Convertito, V., De Matteis, R., Gunnarsdóttir, S. H., Hjörleifsdóttir, V., & Capuano, P. (2022). 3D seismic imaging of the Nesjavellir Geothermal Field, SW-Iceland. *Frontiers in EarthScience*, *10*, 994280.

Aparicio, O. (2023). *Deep temperatures estimated by using a Bayesian rock-physic model and mineral geothermometers in the Berlin Geothermal Field, El Salvador* [Master's thesis, Tohoku University].

Axelsson, G. (2013). Conceptual models of geothermal systems-introduction. *Short course V on conceptual modelling of geothermal systems in El Salvador*.

Beauchamps, G., Ledésert, B., Hébert, R., Navelot, V., & Favier, A. (2019). The characterisation of an exhumed high-temperature paleo-geothermal system on Terre-de-Haut Island (the Les Saintes Archipelago, Guadeloupe) in terms of clay minerals and petrophysics. *Geothermal Energy*, *7*, 1–18.

Bromley, C. (2018). The role of advanced geophysical monitoring in improved resource expansion and make-up drilling strategy. *Proceedings 43rd Workshop on Geothermal Reservoir Engineering*.

Campos, A. (2019). *3D MT resistivity model in BGF (In Spanish).* Internal Report, El Salvador.

Canjura, R. (2016). *Analysis of gravity data in the northern of BGF (In Spanish).* Internal Report, El Salvador.

CGG. (2021). *Berlin-3D Micro-Earthquake Tomography  Gravity joint Inversion.* Internal Report, El Salvador.

DeMets, C. (2001). A new estimate for present-day Cocos-Caribbean plate motion: Implications for slip along the Central American volcanic arc. *Geophysical Research Letters*, *28*.

Didas, M. M., Armadillo, E., Hersir, G. P., Cumming, W., & Rizzello, D. (2022). Regional thermal anomalies derived from magnetic spectral analysis and 3d gravity inversion: Implications for potential geothermal sites in Tanzania. *Geothermics*, *103*, 102431.

GESAL. (2003). *Summary and Integration of the Geoscientific Data*.

Grandis, H., & Dahrin, D. (2014). Constrained two-dimensional inversion of gravity data. *Journal of Mathematical & Fundamental Sciences*.

Hernández, M. (2021). Berlín high temperature geothermal system, El Salvador: Evaluation of geoscientific inputs in the conceptual model – A new weighted model and quantification of favorable drilling targets of the area. *Geothermal Training Programme*.

Hernández, M., Hersir, G., & Axelsson, G. (2023). A new weighted model and quantification of the most favorable drilling targets of Berlín Geothermal Field using leapfrog geothermal. *World Geothermal Congress 2023*.

Hersir, G. P., Guðnason, E. Á., & Flóvenz, Ó. G. (2022). 7.04 - Geophysical exploration techniques. In T. M. Letcher (Ed.), *Comprehensive renewable energy (second edition)* (Second Edition, pp. 26–79). Elsevier. https://doi.org/https://doi.org/10.1016/B978-0-12-819727-1.00128-X

Huttrer, G. W. (2021). Geothermal power generation in the World 2015-2020 Update Report. *Proceedings World Geothermal Congress 2020+1*.

Inc, G. (2023). *The current release of oasis montaj 2023.2* (Version 2023.1). https://my.seequent.com/products/oasis-montaj/latest

Kaufhold, S., Plötze, M., Klinkenberg, M., & Dohrmann, R. (2013). Density and porosity of bentonites. *Journal of porous materials*, *20*, 191–208.

LAGEO. (2019). *Conceptual Model of Berlín Geothermal Field, 2019 (In Spanish).* Internal Report, El Salvador.

LAGEO. (2020). *Annual Operation Report of Berlín Geothermal Power Plant, 2020 (In Spanish).* Internal Report, El Salvador.

LAGEO. (2023). *Actual Status of Berlin Geothermal Field, feb 2023 (In Spanish).* Internal Report, El Salvador.

Lees, J. M. (2007). Seismic tomography of magmatic systems [Large Silicic Magma Systems]. *Journal of Volcanology and Geothermal Research*, *167*(1), 37–56. https://doi.org/https://doi.org/10.1016/j.jvolgeores.2007.06.008

Livingston, E. H. (2004). The mean and standard deviation: What does it all mean? *Journal of Surgical Research*, *119*(2), 117–123. https://doi.org/https://doi.org/10.1016/j.jss.2004.02.008

Omollo, P., & Nishijima, J. (2023). Analysis and interpretation of the gravity data to delineate subsurface structural geometry of the Olkaria Geothermal Reservoir, Kenya. *Geothermics*, *110*, 102663.

Pauling, H., Taverna, N., Trainor-Guitton, W., Witter, E., Kolker, A., Warren, I., Robins, J., & Rhodes, G. (2023). *Geothermal Play Fairway Analysis best practices* (tech. rep.). National Renewable Energy Laboratory (NREL), Golden, CO (United States).

Pavez, C., Tapia, F., Comte, D., Gutiérrez, F., Lira, E., Charrier, R., & Benavente, O. (2016). Characterization of the hydrothermal system of the Tinguiririca

volcanic complex, central chile, using structural geology and passive seismic tomography. *Journal of Volcanology and Geothermal Research*, *310*, 107–117. https://doi.org/https://doi.org/10.1016/j.jvolgeores.2015.11.018

Ponggohong, Suryantini, & A.B., P. (2020). 3D geological and isothermal model of geothermal field based on the integration of geoscience and well data. *IOP Conference Series: Earth and Environmental Science*, *417*(1), 012001.

Poux, B., & O'Brien, J. (2020). A conceptual approach to 3-D "play fairway" analysis for geothermal exploration and development. *Proceedings 42nd New Zealand Geothermal Workshop*, *24*, 26.

Rosid, M., & Sibarani, C. (2021). Reservoir identification at dieng geothermal field using 3d inversion modeling of gravity data. *Journal of Physics: Conference Series*, *1816*(1), 012083.

Saltus, R. W., & Blakely, R. J. (2011). Unique geologic insights from "non-unique" gravity and magnetic interpretation. *GSA Today*, *21*(12), 4–11.

Sarkowi, M., & Wibowo, R. C. (2021). Geothermal reservoir identification in Way Ratai Area based on gravity data analysis. *Journal of Physics: Conference Series*, *2110*(1), 012004.

Seequent. (2023). *Oasis user's guide*. The Bentley Subsurface Company. Christchurch, New Zealand.

SICA. (2021). *Current state of geothermal energy in the region of SICA member countries, 2021, (in spanish)* (tech. rep.). Sistema de Integración Centroamericana (SICA).

Snyder, G., Poreda, R., Fehn, U., & Hunt, A. (2004). Los campos geotérmicos de centroamérica: Influencia del proceso de subducción sobre su composición volátil. *Revista Geológica de América Central*, *30*.

Soulaimani, S., Chakiri, S., Manar, A., Soulaimani, A., Miftah, A., & Bouiflane, M. (2020). Potential-field geophysical data inversion for 3d modelling and reserve estimation (example of The Hajjar mine, Guemassa Massif, Morocco): Magnetic and gravity data case. *Comptes Rendus. Géoscience*, *352*(2), 139–155.

Torio-Henriquez, E. (2007). Petrography and Mineral Alteration in Berlin Geothermal Field. *Thirty-second workshop on Geothermal Rerservoir Engineering*.

UT. (2023). *Anuario estadístico 2023* (tech. rep.). Unidad de transacciones.

Wilson, S. (1960). Physical and chemical investigations of Ketetahi hot springs. *The geology of Tongariro Subdivision. NZ Geol. Survey Bull*, *40*, 124–144.